



# Space-based remote sensing of atmospheric aerosols: The multi-angle spectro-polarimetric frontier



A.A. Kokhanovsky <sup>a,\*</sup>, A.B. Davis <sup>b</sup>, B. Cairns <sup>c</sup>, O. Dubovik <sup>d</sup>, O.P. Hasekamp <sup>e</sup>, I. Sano <sup>f</sup>, S. Mukai <sup>g</sup>, V.V. Rozanov <sup>h</sup>, P. Litvinov <sup>d</sup>, T. Lapyonok <sup>d</sup>, I.S. Kolomiets <sup>i</sup>, Y.A. Oberemok <sup>i</sup>, S. Savenkov <sup>i</sup>, W. Martin <sup>c</sup>, A. Wasilewski <sup>c</sup>, A. Di Noia <sup>e</sup>, F.A. Stap <sup>e,l</sup>, J. Rietjens <sup>e</sup>, F. Xu <sup>b</sup>, V. Natraj <sup>b</sup>, M. Duan <sup>j,k</sup>, T. Cheng <sup>k</sup>, R. Munro <sup>a</sup>

<sup>a</sup> EUMETSAT, Eumetsat Allee 1, D-64367 Darmstadt, Germany

<sup>b</sup> Jet Propulsion Laboratory, California Institute of Technology, 4800 Oak Grove Drive, Pasadena, CA 91109, USA

<sup>c</sup> NASA Goddard Institute for Space Studies, 2880 Broadway, New York, NY, USA

<sup>d</sup> Laboratoire d'Optique Atmosphérique, CNRS/Université de Lille 1, Lille, France

<sup>e</sup> SRON, Netherlands Institute for Space Research, Sorbonnelaan 2, 3584 CA Utrecht, The Netherlands

<sup>f</sup> Faculty of Science and Technology, Kinki University, Kowakae 3-4-1, Higashi-Osaka, Osaka 677-8502, Japan

<sup>g</sup> The Kyoto College of Graduate Studies for Informatics, 7 Monzen Tanaka, Sakyo, Kyoto 606-8225, Japan

<sup>h</sup> Institute of Remote Sensing, University of Bremen, O. Hahn Allee 1, Bremen, Germany

<sup>i</sup> Kiev Taras Shevchenko University, Radiophysics Department, Vladimirska 64/13, Kyiv 01601, Ukraine

<sup>j</sup> Institute of Atmospheric Physics, Chinese Academy of Sciences, Beijing, China

<sup>k</sup> Institute of Remote Sensing and Digital Earth (RADE), Chinese Academy of Sciences, Beijing, China

<sup>l</sup> Institute for Marine and Atmospheric Research, Utrecht University, PO Box 80005, 3508 TA Utrecht, The Netherlands

## ARTICLE INFO

### Article history:

Received 1 July 2014

Accepted 30 January 2015

Available online 28 February 2015

### Keywords:

Aerosol  
Remote sensing  
Polarimetry  
Optical instrumentation  
Radiative transfer  
Climate change

## ABSTRACT

The review of optical instrumentation, forward modeling, and inverse problem solution for the polarimetric aerosol remote sensing from space is presented. The special emphasis is given to the description of current airborne and satellite imaging polarimeters and also to modern satellite aerosol retrieval algorithms based on the measurements of the Stokes vector of reflected solar light as detected on a satellite. Various underlying surface reflectance models are discussed and evaluated.

© 2015 Elsevier B.V. All rights reserved.

## Contents

1. Introduction . . . . .	86
2. Instrumentation . . . . .	86
2.1. Analysis using polarizers . . . . .	87
2.1.1. Spatial separation of polarization components . . . . .	87
2.1.2. S-GLI . . . . .	87
2.1.3. Sequential measurement of polarization components . . . . .	88
2.1.4. Spatial splitting of focal plane images and subsequent polarimetric analysis . . . . .	88
2.2. Analysis using polarizers and retarders . . . . .	89
2.2.1. Polarimetric modulation of the spectrum . . . . .	89
2.2.2. Polarimetric modulation of time domain signal . . . . .	89
3. Forward modeling of remote sensing signals . . . . .	90
3.1. The computational challenge of predictive sensor signal modeling . . . . .	90
3.2. Single scattering, absorption and extinction of light by atmospheric aerosol particles . . . . .	92

\* Corresponding author.

E-mail address: [Alexander.kokhanovsky@eumetsat.int](mailto:Alexander.kokhanovsky@eumetsat.int) (A.A. Kokhanovsky).

3.3.	Optical properties of aerosol populations with various particle size distributions . . . . .	92
3.4.	Radiative transfer (RT) in the Earth's atmosphere . . . . .	94
3.5.	Observable reflected light field characteristics . . . . .	96
3.6.	Computational techniques for solving the vector radiative transfer equation . . . . .	97
3.6.1.	Formulations, transformations and numerical methods . . . . .	97
3.6.2.	Illustration with a current challenge in continuously-varying stratified atmospheres . . . . .	97
3.6.3.	Intercomparison of three forward models . . . . .	97
4.	Solution of the inverse problem . . . . .	98
4.1.	Number of measurements versus number of parameters to be retrieved . . . . .	100
4.2.	JPL's operational MISR and experimental AirMSPI algorithms . . . . .	100
4.3.	The LOA/OP POLDER algorithm . . . . .	100
4.4.	The LOA/GRASP POLDER algorithm . . . . .	101
4.5.	The SRON/POLDER algorithm . . . . .	102
4.6.	The retrieval algorithm for the Directional Polarimetric Camera (DPC) . . . . .	102
4.7.	The GISS/RSP algorithm . . . . .	103
5.	Passive determination of the aerosol profile from oxygen A-band spectroscopy . . . . .	103
6.	Summary, conclusions and outlook . . . . .	106
	List of abbreviations and acronyms . . . . .	107
	Acknowledgments . . . . .	107
Appendix A.	Reflectivity of underlying surfaces . . . . .	107
A.1.	Definitions . . . . .	107
A.2.	Illustration . . . . .	108
A.3.	A convenient parametric surface BRDM model . . . . .	109
A.4.	Discussion . . . . .	111
References	. . . . .	112

## 1. Introduction

Atmospheric aerosols are composed of solid and liquid particles suspended in air (Seinfeld and Pandis, 2006; Kokhanovsky, 2008). They have profound influences on climate, clouds, precipitation, atmospheric chemistry, atmospheric visibility, and human health, motivating an urgent need to understand their global and local properties (Boucher et al., 2013). In particular, parameters such as the aerosol layer height; particle size, shape, and internal structure; chemical composition; and concentration must be studied in both space and time, taking into account that aerosol concentrations and properties are dynamic due to chemical reactions and coagulation, dispersal by wind, removal by clouds and precipitation, and deposition upon the underlying surfaces. Most particles are spherical in shape but nonspherical particles (e.g., irregularly shaped dust grains) are also often present in large numbers. Liquid films or ice, depending on temperature and humidity, can cover solid particles. Some liquid particles are internally inhomogeneous or also covered by thin films or even have other particles (like soot) attached to their surfaces. The classical example is a dissolved salt crystal with higher concentration of salt at the nucleus with outer layer composed of almost pure water.

Aerosols have been extensively studied in situ using ground-based, airborne and ship-borne instrumentation. However, only remote sensing methods can ensure global or even regional coverage. Remote observations of aerosols have been conducted from all of the above platforms, plus satellites. Because the diameters of most particles suspended in the atmosphere are comparable to the wavelength of visible light, optical instruments (radiometers, spectrometers, polarimeters, and imagers) are the most suitable for retrieving their properties. In this paper we review modern methods of atmospheric aerosol studies using spaceborne multi-angular spectropolarimeters. By comparison with traditional instrumentation (e.g., radiometers), the amount of raw data provided by such measurements is very high, easily reaching 100 to 400 measurements (that is, components of the Stokes vector for several observation directions and wavelengths) for a given satellite pixel. This contrasts sharply with the 10 or so measurements per pixel (e.g., different spectral channels) provided by conventional single-view radiometers. This abundance of new data is bound to increase

the accuracy of retrievals of aerosol properties but requires the development of quite complex instruments. Moreover, the software for modeling of optical signals as detected by a satellite, together with corresponding retrieval procedures, need to be at par with the advanced instrumentation. Validation of the retrieved satellite products is of great importance to ensure accurate inferences of aerosol impacts and correction for any biases through refinement of either the instrumentation or retrieval algorithms.

In this paper, we review the major steps related to the development of comprehensive polarimetric instrumentation as well as physics-based processing software for the monitoring of atmospheric aerosol properties, which include aerosol optical thickness, height, concentration, size/shape of particles, and chemical composition (aerosol type). The next section is devoted to the review of modern polarimetric instrumentation. Section 3 is aimed at the description of the forward physics-based models for remote sensing signals based on the theory of vector radiative transfer in vertically inhomogeneous atmospheres. The possible horizontal inhomogeneity of the atmosphere or surface, hence 3D and adjacency effects such as aerosol illumination by light from neighboring clouds or snow fields, is ignored (but briefly discussed in the concluding section). This is an important simplification, potentially leading to biases in the retrieved aerosol properties (Nikolaeva et al., 2005; Kokhanovsky et al., 2010a). The optical models for scattering by individual aerosols are also discussed in this section while parametric representations of underlying reflective surfaces are described in an Appendix section. Section 3 and Appendix A contain respectively a few new computations and measurements, to better illustrate the topics. Section 4 is devoted to the methodology used to retrieve aerosol properties from remote sensing observations, given the forward model. In Section 5, we discuss an emerging passive technology for uncovering the vertical profile of the aerosol, at least coarsely, which uses an interesting spectral feature of the oxygen molecule, the so-called "A-band." Finally, we offer our conclusions and outlook on satellite remote sensing of aerosols in the closing Section 6.

## 2. Instrumentation

In the following section we describe the various polarimetric remote sensing instruments that have, will, or are designed to fly on satellites.

We include satellite instruments for observing the other planets, as well as the Earth, because the earliest example of accurate polarimetric remote sensing of a planetary atmosphere from a satellite was provided by the Pioneer spacecraft observations of Jupiter. The descriptions of instruments are separated into those instruments that use only polarizers and those that use both retarders and polarizers to analyze the incident radiation into its Stokes vector components  $I^T = (I, Q, U, V)$ . The Stokes vector is made up of  $I$ , which is a measure of the intensity of the light;  $Q$  and  $U$ , which define the magnitude and orientation of the linearly polarized fraction of the light; and  $V$ , which is a measure of the magnitude and helicity of the circular polarization (van de Hulst, 1980). We note that the degree of circular polarization of light reflected by clouds and aerosols is typically very small ( $\sim 10^{-4}$  was measured for Jupiter; Kemp et al., 1971a,b) and is not generally measured by Earth observing sensors. Its small magnitude is however diagnostic of the type of planetary atmosphere being observed (cf. Hansen, 1971a,b).

### 2.1. Analysis using polarizers

The Stokes parameters  $I$ ,  $Q$  and  $U$  that define the state of linear polarization of light can be measured using a detector that is sensitive only to the intensity by first transforming the incident beam of light using a polarizer to analyze the polarization state. The intensity that is observed by such a detector is then given by the expression,

$$I_{\text{obs}}(\theta) = \frac{1}{2}(I + Q \cos 2\theta + U \sin 2\theta), \quad (2.1)$$

where  $\theta$  is the angle of rotation of the polarizer with respect to a predefined plane. By making such intensity observations with at least three suitably chosen polarizer orientations,  $I$ ,  $Q$  and  $U$ , can be determined. The following remote sensing instruments make use of such a technique in somewhat different ways.

#### 2.1.1. Spatial separation of polarization components

The use of a Wollaston prism that splits light into angularly separated orthogonal polarization components is one of the oldest methods for the accurate measurement of polarization. It was first introduced for this purpose by Lyot (1929) at the Observatory of Meudon and demonstrated unequivocally that the sunlight reflected by the planets was polarized. Satellite instruments that used the same polarization analysis technique were the Imaging Photopolarimeters on Pioneer 10 and 11 (Pellicori et al., 1973) that observed Jupiter and Saturn; the Orbiter Cloud Photopolarimeter (OCP) on Pioneer Venus (Russell et al., 1977); and the Photopolarimeter Radiometer (PPR) on the Galileo satellite that orbited Jupiter (Russell et al., 1992). In all of these instruments a relay telescope defined a fixed field of view, with the light then passing through filters in a rotating wheel before passing through a Wollaston prism that served as a polarizing beam splitter. Of particular note for this paper is the fact that the linear polarization data obtained by the OCP experiment confirmed that the visible clouds at low and mid-latitudes on Venus were composed predominantly of  $1 \mu\text{m}$  radius  $\text{H}_2\text{SO}_4$  droplets, an identification made previously using Earth-based observations (Hansen and Hovenier, 1974). In addition, it was found that within and extending above the main visible cloud was an extensive haze with a refractive index of  $1.45 \pm 0.04$  at  $550 \text{ nm}$ , an effective radius of  $0.23 \pm 0.04 \mu\text{m}$ , and an effective variance of  $0.18 \pm 0.1$  (Knollenberg et al., 1980). Therefore, the detailed retrieval of aerosols above clouds on Venus have been provided by the polarimetric measurements in 1980 in contrast with much more recent developments for remote sensing of the Earth (Knobelspiesse et al., 2014).

One reason that instruments similar to the planetary polarimeters noted above have not been used for Earth observations is that the spatial scales over which clouds and aerosols vary is much smaller ( $\sim 1$  to  $\sim 10 \text{ km}$ ) for the Earth, which limits the ability of instruments with a fixed field of view to observe a particular scene from multiple angles.

This problem was eliminated in the airborne Research Scanning Polarimeter (RSP), which is a prototype for the Glory Aerosol Polarimetry Sensor (APS, <http://glory.gsfc.nasa.gov/overview-aps.html>) that failed to reach orbit on March 4th, 2011. The RSP instrument uses a polarization compensated scan mirror assembly to scan the fields of view of six bore-sighted, refractive telescopes through  $\pm 60^\circ$  from the normal with respect to the instrument baseplate. The refractive telescopes are paired, with each pair making measurements in three spectral bands. One telescope in each pair makes simultaneous measurements of the linear polarization components of the intensity with polarizer orientations of  $0^\circ$  and  $90^\circ$  ( $I$  and  $Q$ ), while the other telescope simultaneously measures the intensity with polarizer orientations of  $45^\circ$  and  $135^\circ$  ( $I$  and  $U$ ). This approach ensures that the polarization signal is not contaminated by scene intensity variations during the course of the polarization measurements, which could create false polarization. These measurements in each instantaneous field of view in a scan provide the simultaneous determination of the intensity, and the degree and azimuth of linear polarization in all nine spectral bands. When the RSP is oriented to scan in the plane of direction of flight of an aircraft, multiple views of each sub-aircraft scene can be aggregated.

The instrument has nine spectral channels that are divided into two groups based on the type of detector used: visible/near infrared (VNIR) bands at  $0.410$ ,  $0.470$ ,  $0.550$ ,  $0.670$ ,  $0.865$  and  $0.960 \mu\text{m}$  and shortwave infrared (SWIR) bands at  $1.590$ ,  $1.880$  and  $2.250 \mu\text{m}$ . These spectral bands sample the spectrum of reflected solar radiation over most of the radiatively significant range, with measurements under typical clear sky conditions ranging from significant Rayleigh scattering ( $0.410 \mu\text{m}$ ) to single scattering by aerosol ( $2.250 \mu\text{m}$ ) within a single measurement set. Since two telescopes are required to measure  $I$ ,  $Q$  and  $U$  and each pair of telescopes only provides measurements in three spectral bands, RSP has a total of six telescopes: three pairs, with each pair measuring  $I$ ,  $Q$  and  $U$  in three spectral bands.

The desired polarization-insensitive scanning function of the RSP is achieved by the use of a two-mirror system with the mirrors oriented such that any polarization introduced at the first reflection is compensated for by the second reflection. The scan system allows for a dark reference and polarization references to be viewed on every scan enabling continuous tracking of calibration stability and accuracy. Bore-sighted refractive telescopes define the  $14 \text{ mrad}$  field of view of the RSP. Dichroic beam splitters are used for spectral selection, interference filters define the spectral bandpasses and Wollaston prisms spatially separate the orthogonal polarizations onto the pairs of detectors. The detectors for the VNIR wavelengths are pairs of UV-enhanced silicon photodiodes. The detectors for the SWIR wavelengths are pairs of HgCdTe photodiodes with a  $2.5 \mu\text{m}$  cutoff cooled to  $163 \text{ K}$ .

A liquid nitrogen Dewar is used to cool the SWIR detectors during both ground and airborne operation. To optimize the performance of the SWIR channels the temperature of the detectors is servo controlled at  $163 \text{ K}$  during operation. Digital data from 152 scene sectors (i.e., instantaneous fields of view, or "IFOVs") over  $121^\circ$  of scan, dark samples from 10 sectors and instrument status data are formatted by the RSP electronics and each scan is transmitted to a personal computer for storage. The average data rate of  $110 \text{ kbps}$  provides readout of the 36 signal channels together with instrument status data with a scan period of  $0.8409 \text{ secs}$ . In order to get contiguous (scan line-to-line) or oversampled coverage on an aircraft the pixel size (field of view x aircraft height) needs to be larger than the distance the aircraft moves between successive nadir views (scan period x aircraft velocity), which means that the ratio of aircraft velocity to height needs to be less than  $0.017 \text{ sec}^{-1}$  and this is achievable on a wide range of aircraft from small Cessnas to the NASA ER-2.

#### 2.1.2. S-GLI

Japanese space agency (JAXA) plans to launch global change observation mission satellite (GCOM-Climate) series. The first GCOM satellite, called GCOM-C1, will be launched in early winter of 2017 as a 5-year mission. The subsequent launches of GCOM-C2 and -C3 are spaced at

4-year intervals. Thus, the total observation period is at least 13 years from GCOM-C1 to -C3. The GCOM series is a component of the long-term Global Earth Observation System of Systems (GEOSS). The second generation global imager (S-GLI) will be included in the GCOM-C payloads. The S-GLI is an imaging sensor with observational characteristics similar to MODIS on Terra and Aqua for understanding of Earth's environment (Imaoka et al., 2010).

The S-GLI incorporates 18 spectral channels to measure Earth's reflectance from near-ultraviolet to near-infrared wavelengths and thermal emission in the infrared region. Although multi-spectral information provides useful aerosol constraints, accurate retrievals require multi-angular observations of both intensity and polarization characteristics of reflected solar light. Therefore, the S-GLI has two outstanding features with respect to aerosol observations. The first is polarization measurements at 673.5 and 868.5 nm. The Stokes parameters ( $I$ ,  $Q$ ,  $U$ ) are obtained from measurements at three different linear polarizer angles, which are the same as in the Polarization and Directionality of Earth Reflectance (POLDER) instrument system, i.e.,  $0^\circ$ ,  $60^\circ$ , and  $120^\circ$  (Deschamps et al., 1994). The IFOV (instantaneous field of view) of the polarization channels is  $1 \text{ km} \times 1 \text{ km}$  (Imaoka et al., 2010). This is much smaller than POLDER's  $6 \text{ km} \times 7 \text{ km}$  footprints (Deschamps et al., 1994). In addition, the IFOV of S-GLI is  $250 \text{ m} \times 250 \text{ m}$  in the non-polarimetric channels. Combination of this fine resolution information with polarization enables correction for broken clouds. Moreover, polarization observations are taken at along-track view angles of  $+45^\circ$  or  $-45^\circ$  in order to observe the middle scattering direction (from  $80^\circ$  to  $120^\circ$ ). The measurement performed at 380 nm wavelength available at S-GLI is the second novel feature for aerosol retrievals because most underlying surfaces (except snow and ice) are dark in the UV. The near-UV channel can be used to estimate aerosol absorption effects because many aerosol types (including dust and smoke) have increased absorption in the UV region of the electromagnetic spectrum.

### 2.1.3. Sequential measurement of polarization components

The POLDER instrument uses sequential measurements with polarizers in different orientations to measure the linear polarization of light reflected by the Earth. This instrument has flown on ADEOS-1, ADEOS-2 and most recently on PARASOL. Since the PARASOL mission was the longest in which a POLDER instrument was flown, and was part of the A-Train (L'Ecuyer and Jiang, 2010), the POLDER configuration used for that mission is described here. POLDER (Deschamps et al., 1994) is a digital camera with a  $274 \times 242$ -pixel silicon CCD detector array, wide-field telecentric optics and a rotating filter wheel enabling measurements in 9 spectral channels from blue to near-infrared (0.445, 0.492, 0.564, 0.670, 0.763, 0.861, 0.907 and  $1.020 \mu\text{m}$ ) where there are two filters with 10 and 40 nm widths in the oxygen A-band at  $0.763 \mu\text{m}$ . The spectral bands have widths of 20 nm except at  $0.861 \mu\text{m}$ , where the bandwidth is 40 nm in order to provide a high signal to noise ratio. In the spectral bands at  $0.490 \mu\text{m}$ ,  $0.670 \mu\text{m}$  and  $0.865 \mu\text{m}$  there are polarizers in directions of  $0^\circ$ ,  $60^\circ$  and  $120^\circ$  that are used to provide estimates of the Stokes parameters  $I$ ,  $Q$  and  $U$ . These sequential polarization measurements are motion compensated by wedge prisms in order to reduce "false" polarization that is caused by intensity variations between successive polarizer positions. As it acquires a sequence of images every 20 s, the instrument can view ground targets from different angles between  $\pm 51^\circ$  along track, with a cross-track FOV of  $\pm 43^\circ$ .

The POLDER instrument has demonstrated that its combination of multi-spectral, polarization and multi-angle observations has considerable capability for retrieving aerosol properties (Dubovik et al., 2011; Hasekamp et al., 2011; Waquet et al., 2013). The Multi-spectral, Multi-directional Multi-polarization Instrument (3MI) is a planned successor to POLDER (Biron et al., 2013; Marbach et al., 2013). 3MI will be similar to POLDER in its use of wide-field, telecentric optics and a filter wheel for spectral and polarimetric analysis. However, it will have expanded spatial coverage ( $100.44^\circ$  along and cross-track), higher spatial resolution of 4 km at nadir, and an expanded spectral range ( $0.41$ – $2.13 \mu\text{m}$ )

with more spectral bands having polarization measurements. While 3MI has not been built yet and the exact spectral band specifications may change it is expected to have a similar number and spectral range as RSP/APS for the bands that measure polarization. In addition, it will include the unpolarized observations in the oxygen "A" and water vapor bands that were used on POLDER.

A new airborne Directional Polarimetric Camera (DPC) with high spatial resolution (4 m at 4000 m a.g.l.) has been developed (Cheng et al., 2011; Xie et al., 2013) to retrieve the aerosol optical properties. The DPC is an experimental airborne instrument focused on monitoring aerosol pollution over cities. The DPC instrument is a wide field of view radiometer designed to measure the polarization and directionality of the solar radiation reflected by the Earth–atmosphere system in the visible and near infrared spectrum. It is a POLDER-type polarized camera with a significantly better spatial resolution (nadir pixel size:  $4 \text{ m} \times 4 \text{ m}$  at 4000 m cruising level) for monitoring aerosol emission sources in cities. The DPC instrument is a CCD camera that covers the spectral range of 400 to 900 nm with the three polarized spectral bands (490 nm, 665 nm, and 865 nm). Each polarized band is equipped with a set of three linear polarizers with polarization azimuths separated by an angle of  $60^\circ$ . This configuration allows the angle of polarization and the linear polarized radiance to be determined.

### 2.1.4. Spatial splitting of focal plane images and subsequent polarimetric analysis

The Philips prism has been widely used in television cameras to split the focal plane images into three parts that are then analyzed to provide red, green and blue images for broadcast. If care is taken in the design of the coatings for such a prism it can also be used to provide three identical images that can then be analyzed using polarizers in three orientations (e.g.,  $0^\circ$ ,  $45^\circ$  and  $90^\circ$ ). This allows the Stokes parameters  $I$ ,  $Q$  and  $U$  to be determined simultaneously, with the potential to eliminate "false" polarization and achieve high polarimetric accuracy with no moving parts. Such an approach has been taken in the HyperAngular Rainbow Polarimeter (HARP) that is being built for launch on a CubeSat in early 2015. Similar measurements have been obtained from an airborne prototype called the Rainbow Polarimetric Imager (RPI).

The Passive Aerosol & Clouds Suite Polarimeter (PACS) is new hyper-angular imaging polarimeter for aerosol and cloud measurements designed to meet the requirements of the proposed Aerosol-Cloud-Environment (ACE) decadal survey mission. The full PACS system consists of three wide field of view ( $110^\circ$  cross track) telescopes covering the UV, VNIR, and SWIR spectral ranges with angular coverage between  $+55^\circ$  forward and  $-55^\circ$  backwards. The angular density can be selected to cover up to 100 different viewing angles at selected wavelengths. PACS\_VNIR is a prototype airborne instrument designed to demonstrate PACS capability by deploying just one of the three wavelength modules of the full PACS. With wavelengths at 470, 550, 675, 760 and 875 nm, PACS\_VNIR flew for the first time during the PODEX experiment in January/February 2013 aboard the NASA ER-2 aircraft. PACS\_SWIR (1.64, 1.88, 2.1, and  $2.25 \mu\text{m}$ ) is currently under construction and should be operational soon. PACS\_UV has been fully designed, but is not yet under construction. During the PODEX flights PACS\_VNIR collected data for aerosol and clouds over variable surface types including, water, vegetation, urban areas, and snow. The data is currently being calibrated, geolocated and prepared for the inversion of geophysical parameters including water cloud size distribution and aerosol microphysical parameters (<http://userpages.umbc.edu/~martins/laco/projects.html>). These instruments combine a wide-field of view lens with a Phillips prism to split the focal plane image into three identical images, linear polarizers at  $0^\circ$ ,  $45^\circ$  and  $90^\circ$  in front of each focal plane and wavelength separation by interference filters on the focal plane array. The spectral bands that are available in the HARP/RPI sensors are 410, 550 and 660 or 750 nm. The multi-angle looks are acquired in the same way as POLDER, by taking multiple overlapping images with a particular pixel on the ground being viewed from multiple angles.

## 2.2. Analysis using polarizers and retarders

An alternative to using polarizers in multiple positions or polarizing beam splitters to measure the Stokes parameters  $I$ ,  $Q$  and  $U$  is to encode the polarization state into temporal, or spectral variations in the intensity using retarders. This approach has the advantage that it can eliminate, or substantially reduce “false” polarization. In Eq. (2.2) we show how the intensity of a detector behaves when it observes a scene through a polarizer with a circular retarder (Chipman, 1994) in front of it:

$$I_{obs}(t, \lambda) = \frac{1}{2}(I + Q \cos(\delta(t, \lambda)) + U \sin(\delta(t, \lambda))). \quad (2.2)$$

Here  $\delta(t, \lambda)$  is the, possibly time varying, retardance and  $\lambda$  is the wavelength of light. If the retardance is large then the intensity will have significant variations with wavelength that will have the magnitudes of  $Q$  and  $U$  encoded in them. If the retardance is moderate, but time varying, then the intensity will vary in time in a manner that can be analyzed to determine the magnitudes of  $Q$  and  $U$ . In the following we describe systems that use these two different types of encoding of the polarization signal.

### 2.2.1. Polarimetric modulation of the spectrum

The original approach to spectral modulation to encode the Stokes vector into an intensity measurement was presented by Oka and Kato (1999) and implemented in an airborne instrument called the HyperSpectral Polarimeter for Aerosol Retrievals (HySPAR) by Jones et al. (2004). In this method a system of polarization analysis optics is inserted between the scene being viewed and an imaging spectrometer. These polarization analysis systems have the advantage, for implementation in a remote sensing system, that they have no moving parts. The way that they work is by imposing a variation on the incident spectrum that is rapid (hyperspectral) compared with the spectral variations of atmospheric aerosol and molecular scattering. This rapid variation depends on the Stokes vector and in the HySPAR instrument allowed the circular polarization as well as the intensity and state of linear polarization to be determined, at the expense of having to analyze three different sinusoidal variations in the spectrum. Snik et al. (2009) proposed a simpler approach that uses a quarter wave retarder, a multiple-order retarder and a polarizer. In this approach only the intensity and state of linear polarization are determined.

In this method there is only a single modulating function to analyze and the optics can be made robust and insensitive to thermal variations. This polarization analysis technique has been incorporated into an instrument called the Spectropolarimeter for Planetary Exploration (SPEX, van Harten et al., 2011). This instrument is a hyperspectral imager with multi-viewing capability enabled by using multiple static viewports with views in different directions. Each viewport is equipped with polarization encoding optics that consists of a Fresnel rhomb that is used as an achromatic quarter wave retarder, an athermal combination of MgF<sub>2</sub> and sapphire that is used for the multiple-order retarder and a crystal (Wollaston) polarizer that provides the polarization analysis in the form of two complementary spectrally modulated light beams. This design is virtually free from instrumental polarization. Since the method uses spectral analysis in the determination of the polarization state, the spectral range that is covered is that of the spectrometer.

In a prototype version of SPEX, nine realizations of these polarization encoding units provide a 112° angular viewing range. All 18 light beams are coupled into a single imaging spectrograph that provides cross-track imagery in a pushbroom mode with spectral analysis in the along track direction of the focal plane. This prototype offers a 7° swath, a spectral range from 400 to 800 nm, and an average spectral resolution of 2 nm for radiance and 20 nm for polarization. Recent calibration measurements (Rietjens et al., 2015; van Harten, 2014) with this prototype show an

absolute polarimetric accuracy better than  $0.002 + 0.01 \times P$ , with  $P$  being the degree of linear polarization (DOLP):  $P = \sqrt{Q^2 + U^2}/I$ .

A SPEX system with a spectral range of 0.4–1.6 μm is planned for an Earth observing mission. This spectral range will be covered using a visible and a shortwave infrared version of SPEX, with an average spectral resolution of the polarization state of 20 nm (or 60 nm, depending on the implementation) in the visible and 80 nm in the shortwave infrared. The spectral resolution of the radiance will be typically a factor of 5 or more better, in order to adequately sample the spectral modulation pattern. A new design includes a modular version of SPEX with one opto-mechanical unit and detector per viewport and a 30° swath. The goal for the polarimetric accuracy is  $0.001 + 0.005 \times P$ .

### 2.2.2. Polarimetric modulation of time domain signal

In astronomical applications it is feasible to use a photo-elastic modulator (PEM) to generate high speed variations in the retardance as a function of time,  $\delta(t)$ , in Eq. (2.2) that are then demodulated at the resonant frequency (typically between 10 and 100 kHz) and harmonics of the PEM in order to determine  $Q$  and  $U$  using the different phase and harmonic content of their modulation (Povel et al., 1990; Keller, 2001). For Earth remote sensing applications this is an extremely high speed at which to operate a focal plane given that the frame rate of a pushbroom imager with a resolution of hundreds of meters in low Earth orbit is expected to be on the order of tens of milliseconds. An ingenious approach to imaging polarimetry for Earth viewing satellite applications has therefore been proposed in which a pair of PEMs are used as the source of retardance modulation, between a pair of crossed quarter wave plates, with the analysis of the signal being performed at the beat frequency  $\omega_b$  (Diner et al., 2007). In this method analyzers oriented at 0° ( $I_0$ ) and 45° ( $I_{45}$ ) are used to provide estimates of  $I$ ,  $Q$  and  $U$  as indicated in the following equations:

$$\begin{aligned} I_{obs}(t, \lambda) &= \frac{1}{2}(I + QJ_0(2\delta_0 \cos(\omega_b t - \eta))), \\ I_{obs}(t, \lambda) &= \frac{1}{2}(I + UJ_0(2\delta_0 \cos(\omega_b t - \eta))), \end{aligned} \quad (2.3)$$

where  $\delta_0$  is the average of the peak retardance of the two PEMs,  $\eta$  is a phase term, and  $J_0$  is the 0th order Bessel function. “False” polarization using this measurement approach is expected to be a weak effect since only temporal variations in the scene that are similar to the terms modulating  $Q$  and  $U$  will alias into those elements. A more complete scene model than shown in Eq. (2.3) allows for linear variation of  $I$ ,  $Q$ , and  $U$  during the beat period (Diner et al., 2007, 2011).

This polarimetric concept has been implemented as an imaging polarimeter, the Airborne Multiangle SpectroPolarimetric Imager (AirMSPI), in which a pushbroom camera provides cross-track coverage with the different spectral bands and polarization state measurements extending in the along-track direction. The AirMSPI spectral bands are centered at 355, 380, 445, 470P, 555, 660P, 865P, and 935 nm where bands for which the state of linear polarization is measured are noted by a “P”. AirMSPI’s camera has an effective focal length of 29 mm and a cross-track field of view of  $\pm 15^\circ$  with light being brought to a focus using a three-mirror  $f/5.6$  anastigmatic, telecentric system (Diner et al., 2013). The mirrors in the system have low diattenuation and retardance and high reflectance, minimizing instrumental polarization that might be created by the camera before the polarization analysis. For operation on the NASA ER-2 AirMSPI is mounted on a gimbal in order to provide multiple viewing directions for a particular scene. Selected characteristics of AirMSPI together with those for other polarimeters are summarized in Table 2.1. A photo of the instrument is given in Fig. 2.1 and example image measurements are shown in Fig. 2.2.

The MSPI team is currently developing a second-generation instrument, AirMSPI-2, with spectral bands located at 365, 385, 445P, 540, 645P, 751, 763, 865P, 945, 1620P, 1885, and 2185P nm, where “P” means

**Table 2.1**

The spectral channels of the polarimetric instrumentation. The channels, where the parameters ( $I$ ,  $Q$ ,  $U$ ) are measured are given in bold. The S-GLI push-broom instrument, not shown in the table (but described in Section 2.1.2), performs the ( $I$ ,  $Q$ ,  $U$ ) measurements only at two wavelengths (670 and 865 nm) at a fixed observation direction, either  $45^\circ$  (forward scan) or  $-45^\circ$  (backward scan), depending on the scattering angle, which by definition must be smaller than  $120^\circ$ . Additionally, the measurements of the intensity of reflected light at these wavelengths (and also at other channels) at the nadir direction are performed by S-GLI.

Instrument	RSP	AirMSPI	POLDER-3	3MI
Reference	Cairns et al. (1999)	Diner et al. (2013)	Deschamps et al. (1994)	Biron et al. (2013)
Channels	<b>410, 470, 550, 670, 865, 960,</b> <b>1590, 1880, 2250</b> nm	355, 380, 445, <b>470</b> , 555, <b>660, 865</b> , 935 nm	445, <b>492</b> , 564, <b>670</b> , 763, <b>861</b> , 907, 1020 nm	<b>410, 443, 490, 555, 670</b> , 763, 765, <b>865</b> , 910, 1370, <b>1650, 2130</b> nm
Observation angles	140	Up to 30	Up to 16	Up to 14
Number of observations (see Eq. (4.1))	3780	420	224	392

that the first 3 components of the Stokes vector are measured. AirMSPI-2 is a prototype for future UV-to-SWIR spaceflight versions of MSPI.

### 3. Forward modeling of remote sensing signals

#### 3.1. The computational challenge of predictive sensor signal modeling

At the core of a physics-based retrieval algorithm to infer aerosol properties is a forward model that predicts the signals measured by sensors, be they ground-based, shipborne, airborne, or in space. This model will depend on individual particle optics, a microphysical description of the aerosol population, as well as macroscale parameters that describe the atmosphere as a whole and the underlying surface.

Most importantly, it must capture the radiation transport physics that moves sunlight from its source to various sinks in the atmosphere/surface system, and to light-measuring devices wherever they may be. The purpose of a forward model for remote sensing signals is to map a set of  $m$  aerosol (and possibly surface) properties formally represented by a “state” vector  $\mathbf{x}$  to values of an  $M$ -dimensional vector  $\mathbf{y}$  that contains all the observations to be used in the retrieval. In mathematical shorthand, we have

$$\mathbf{y} = \mathbf{F}(\mathbf{x}) + \boldsymbol{\varepsilon}. \quad (3.1)$$

where  $\boldsymbol{\varepsilon}$  is instrument noise and, if it is known, the random (as opposed to systematic) part of forward model error.

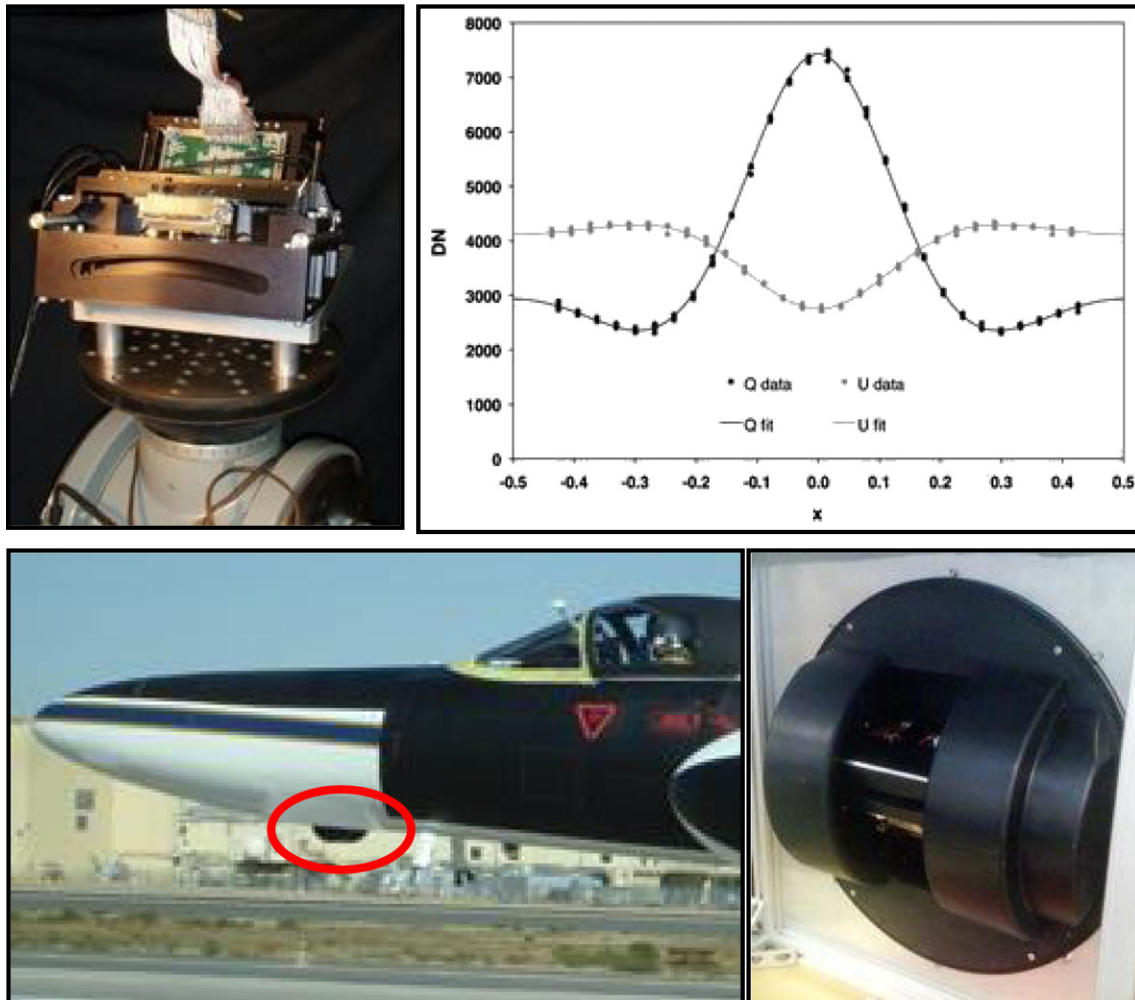


**Fig. 2.1.** Multi-angle Spectro-Polarimetric Imager (MSPI). Clockwise from the upper left-hand corner: (i) MSPI prototype in a configuration for operation from ground (GroundMSPI) where the scene is scanned vertically using a horizontal axis of rotation; the curved geometry of the inlet baffle is required because linear detector arrays in image space map to slightly curved arcs in object space. (ii) Output beat-frequency signals from the dual PEMs are fitted using Eq. (2.3), yielding  $I$  and  $Q$  from line arrays with  $0^\circ$  polarizers (“ $Q$  data”), and  $I$  and  $U$  from line arrays with  $45^\circ$  polarizers (“ $U$  data”). (iii) Current airborne version of MSPI (AirMSPI) mounted on a high-precision gimbal for push-broom imaging. (iv) AirMSPI mounted in the nose of NASA’s ER-2 aircraft.

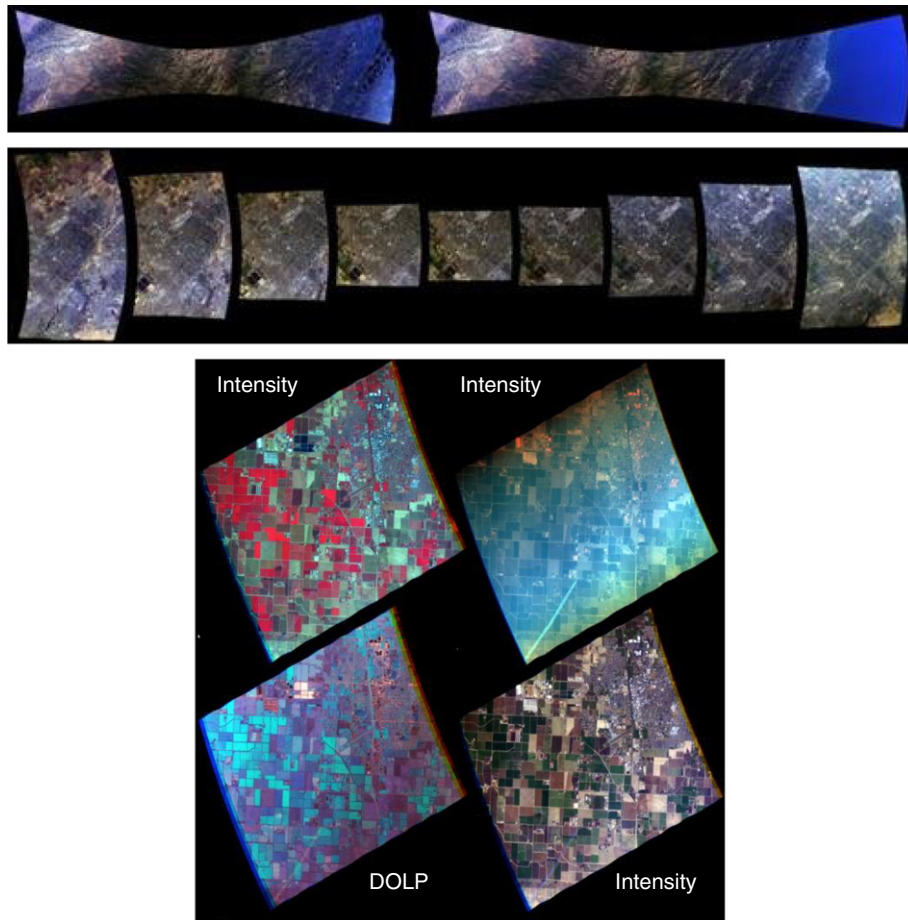


**Fig. 2.2.** Samples of AirMSPI data. NASA's ER-2 aircraft cruises at an altitude of 20 km where, at nadir, AirMSPI's pixels are 7 m in size and its swath exceeds 10 km. The gimbal that holds AirMSPI (see Fig. 2.1) can be programmed to sweep continuously back and forth along track fast enough to collect wide angle views; a succession of such data provides imagery at several angles for a given ground pixel (example in upper panel: Santa Barbara, CA, 1 August 2013, intensity in true color); in this mode, uniform ground samples are registered on a 25 m grid in ground data processing. AirMSPI can also operate in a "step-and-stare" mode that emulates a MISR-like sensor in space (example in middle panel: Bakersfield, CA, 22 January 2013, intensity in true color); collection of up to 31 discrete angles has been demonstrated by limiting the along-track length of the target area. The bottom panel shows color composites of step-and-stare AirMSPI data (nadir view) captured on 22 January 2013, 19:59 UTC, above Hanford, CA. In the lower panel, we notice the serendipitous occurrence of a contrail from an aircraft that is under-flying NASA's ER-2 (altitude 20 km) carrying AirMSPI. The contrail is most apparent in the UV-blue composite in the upper right. In the same panel, densely vegetated fields are bright red in the "false-color" composite in the upper left and, accordingly, they become bright blue in degree of linear polarization. The highly polarized rectangular sectors in the DOLP image correspond to a water treatment plant; these same sectors are very dark in the corresponding false-color intensity image (upper left) as well as in its true-color counterpart (lower right).

In this section, we examine the physical nature of this forward model while the next section is devoted to its inversion, which is to derive  $\mathbf{x}$  from  $\mathbf{y}$ , generally with some ancillary information and/or applicable constraints to help the convergence of the algorithm that searches  $\mathbf{x}$ -space for a good fit of the observations with  $\mathbf{y}$ .

Computational models in general, and forward remote sensing models in particular, must be evaluated along the three entangled dimensions of accuracy/precision, efficiency, and fidelity. Accuracy and precision are quantified by *Verification* procedures such as benchmarking or model inter-comparison exercises, as illustrated further on. Following Roache (1998), the key question is: *Are we solving the equations right?* Conceptually, efficiency is just a matter of computer time required to get the answer. Accuracy/precision and efficiency are obviously both desirable attributes for the forward model in an atmospheric remote sensing algorithm since the inversion procedure will likely call for iterative evaluations of  $\mathbf{F}(\mathbf{x})$ . However, they are generally conflicting goals. A balance or compromise must therefore be sought. Moreover, this necessary tradeoff only makes sense at a given level of forward model fidelity, which describes how well it represents the real world. Fidelity is not as straightforward to quantify as accuracy or efficiency. The total number of parameters in the model, which must be  $\geq m$ , the dimension of  $\mathbf{x}$ , or its "degrees of freedom," comes to mind. At any rate, this opens the key

question of *Validation*—the other "V" in "V&V." Roache (1998) now asks: *Are we solving the right equations?*

A computational model's validation normally calls for direct comparison of its prediction with real-world observations, always bearing in mind its intended purposes. Without this essentially programmatic input, there is no objective criterion for certifying a model as "good enough." In the present context of atmospheric optics and aerosol remote sensing, this is tantamount to asking about whether the retrieved aerosol properties agree well enough with some "truth" about them collected either in situ or by some other (presumably well-established) remote sensing technique. NASA's ground-based Aerosol Robotic Network or "AERONET" (Holben et al, 1998) is a popular source of validation data. In situ aerosol characterization is highly desirable as well, but the sampling (at a surface location or along an aircraft flight track) is necessarily very sparse while scattered and reflected radiances integrate over large areas and volumes.

Model fidelity should thus be held constant (in principle, at a level determined by the demands of the application) in any meaningful accuracy-versus-efficiency tradeoff study. A sensible requirement for model accuracy and precision is that it solves the forward signal prediction problem in Eq. (3.1) to within the sensor's noise level over the expected range of input parameters,  $\mathbf{x}$ . A sensible requirement for

efficiency is to enable the inverse problem solution—formally (if the inverse problem solution exists for a given set of measurements),  $\mathbf{x} = \mathbf{F}^{-1}(\mathbf{y})$ —to execute fast enough for the application. That criterion will be different for processing a whole mission worth of data and for a case study (e.g., focused on some field campaign). A sensible requirement for fidelity is that all the key parametric sensitivities of the signal, i.e., effects that are not overwhelmed by instrument noise, are represented in the set of input parameters, some or all of which are contained in  $\mathbf{x}$ .

There are two distinct stages in the prediction of  $\mathbf{y}$  based on  $\mathbf{F}(\mathbf{x})$  for a given  $\mathbf{x}$  and a specified observational sampling. At both stages, the forward signal modeler must necessarily make assumptions that we will lay out as clearly as possible since these assumptions are liabilities (contributions to “forward model error”) in the retrieval. The first stage is to convert physico-chemical attributes of the aerosol particulates into optical properties. In turn, this translation task has particle-level and microphysical aspects. At the end of this procedure, we know how light interacts (by scattering or absorption) with an aerosol population characterized by a handful of parameters that will become targets for determination by remote sensing. In the second stage, this local information is ingested into a radiation transport (RT) model accounting for all orders of scattering and reflection. This extends the predictive capability to the macroscopic scales where it is needed; the thickness of the whole atmosphere as well as any vertical variations in optical properties and, if necessary, scales of horizontal variability must be considered.

### 3.2. Single scattering, absorption and extinction of light by atmospheric aerosol particles

A particle's chemical make-up translates to a complex index of refraction, denoted by  $n$ , which is expected to vary with wavelength. However, we must ask: Is the particle of interest chemically homogeneous? If so, we can proceed. If not, one should first account for the so-called “internal” mixture of materials in a single aerosol particle (e.g., Lesins et al., 2002) or use general solutions of Maxwell theory for inhomogeneous scatterers (Babenco et al., 2003). A natural approach to internal mixing is “homogenization,” i.e., the derivation of an effective value for  $n$ . This is never as simple as a volume- or mass-weighted mean of the components of the mixture, and will invariably depend of the structural details of the mixture. However, the homogenization approach to the internal mixing problem may not always be feasible at the required level of accuracy. Assuming it is, we now have a value for  $n$ , and we must next define the particle's outer shape.

Here, the default assumption is a sphere of radius  $r$ . Often this is a gross misrepresentation of particle shape: smoke particle clusters near sources, dust grains, pollen, and sea salt crystals are just a few examples. That said, a spheroidal or spherical shape might be a reasonable assumption, especially after mineral or organic aerosols have aged and/or hydrated. If the spherical particle assumption is acceptable, we can use classic Lorenz–Mie scattering theory (e.g., Mishchenko and Travis, 2008) where Maxwell's equations are solved inside and outside of the spherical region where  $n = n_r - n_i \times i$  differs from 1.

The outcome of this electromagnetic (EM) wave scattering computation is a specific prediction for the extinction cross-section matrix  $\mathbf{K}(r, \lambda, n_\lambda)$  in

$$\delta\mathbf{I} = -N\mathbf{K}(r, \lambda, n_\lambda)\mathbf{I}\delta\ell, \quad (3.2)$$

where  $\delta\mathbf{I}$  is a change in the Stokes vector  $\mathbf{I} = [I, Q, U, V]^T$  (where superscript T means transpose) as it crosses a small distance  $\delta\ell$  in the optical medium and  $N$  is the density of a monodisperse population of particles of radius  $r$ . For spherical particles made of a material that is not optically active, we have  $\mathbf{K}(r, \lambda, n_\lambda) = C_e(r, \lambda, n_\lambda)\mathbf{1}$ , where  $\mathbf{1}$  is the unitary diagonal matrix and  $C_e(r, \lambda, n_\lambda)$  is the extinction cross-section, typically expressed in  $\mu\text{m}^2$ . The latter quantity is conventionally expressed as  $C_e(r, \lambda, n_\lambda) = \pi r^2 Q_e(x, n_\lambda)$ , where  $Q_e(x, n_\lambda)$  is a non-dimensional

“efficiency factor” for extinction of light dependent only on  $n_\lambda$  and the so-called “size parameter”  $x_\lambda = 2\pi r / \lambda$ .

In this review, we focus on the solar spectrum where the wavelength ranges from  $\approx 300$  nm in the UV to  $\approx 3000$  nm in the SWIR. Particle size  $r$  has a larger range, from a few nm to  $100 \mu\text{m}$ . This means that  $x$  can vary over 5 orders of magnitude, which creates a computational challenge. By contrast, the range for  $n_r$  is modest ( $\approx 1.3$  to  $\approx 1.7$ ) but  $n_i$  can range from  $0^+$  to a finite  $O(1)$  value in the most absorbing materials.

Another outcome of a detailed Lorenz–Mie scattering computation is the a priori complete  $4 \times 4$  matrix of differential cross-sections  $\mathbf{Z}(\theta_s, r, \lambda, n_\lambda)$  in

$$\delta\mathbf{I}(\Omega_s) = N\mathbf{Z}(\theta_s, r, \lambda, n_\lambda)\mathbf{I}(\Omega_0)\delta\ell\delta\Omega_s, \quad (3.3)$$

where  $\delta\mathbf{I}(\Omega_s)$  is the Stokes vector of light beam scattered into a small element of solid angle  $\delta\Omega_s$  around direction  $\Omega_s$  from a light beam  $\mathbf{I}(\Omega_0)$  coming in from direction  $\Omega_0$ , and  $\theta_s = \cos^{-1}\Omega_s \cdot \Omega_0$  is the scattering angle. Recall that  $\delta\Omega_s = \delta\cos\theta_s\delta\phi_s$  where  $\phi_s$  is the azimuthal angle around  $\Omega_0$ .

Matrix  $\mathbf{Z}(\theta_s, r, \lambda, n_\lambda)$  clearly has units of a differential cross-section [ $\mu\text{m}^2/\text{sr}$ ]. The usual way of writing  $\mathbf{Z}(\theta_s, r, \lambda, n_\lambda)$  is as  $C_s(r, \lambda, n_\lambda)\mathbf{P}(\theta_s; x_\lambda, n_\lambda)/4\pi$  where  $C_s(r, \lambda, n_\lambda)$  is the total scattering cross-section in  $\mu\text{m}^2$ , and  $\mathbf{P}(\theta_s; x_\lambda, n_\lambda)$  is the so-called “phase matrix” in dimensionless form (with the  $1/4\pi$  normalization yielding the  $\text{sr}^{-1}$  units). In turn,  $C_s(r, \lambda, n_\lambda)$  is conventionally factored as  $\pi r^2 Q_s(x_\lambda, n_\lambda)$ , i.e., the geometric area of the scattering particle projected perpendicular to the incoming beam, times a dimensionless “efficiency” factor  $Q_s(x_\lambda, n_\lambda)$ .

By definition, we have

$$C_s(r, \lambda, n_\lambda) = 2\pi \int_0^\pi Z_{11}(\theta_s, r, \lambda, n_\lambda) \sin\theta_s d\theta_s, \quad (3.4)$$

and the phase matrix  $\mathbf{P}(\theta_s; x_\lambda, n_\lambda) = 4\pi\mathbf{Z}(\theta_s, r, \lambda, n_\lambda) / C_s(r, \lambda, n_\lambda)$  is normalized in such a way that

$$\int_0^\pi P_{11}(\theta_s; x_\lambda, n_\lambda) \sin\theta_s d\theta_s = 2. \quad (3.5)$$

When  $n_{i1} \equiv 0$ , it follows:  $C_s(r, \lambda, n_\lambda) = C_e(r, \lambda, n_\lambda)$ . If  $n_{i1} > 0$ , and therefore  $C_s(r, \lambda, n_\lambda) = C_e(r, \lambda, n_\lambda)$ , then the cross-section for absorption  $C_a(r, \lambda, n_\lambda) = \pi r^2 Q_a(x_\lambda, n_\lambda)$ , with its efficiency factor  $Q_a(x_\lambda, n_\lambda)$ , is defined as  $C_e(r, \lambda, n_\lambda) - C_s(r, \lambda, n_\lambda) \geq 0$ . This immediately yields the identity  $Q_e(x_\lambda, n_\lambda) = Q_s(x_\lambda, n_\lambda) + Q_a(x_\lambda, n_\lambda)$ .

Well-known asymptotic regimes are obtained in the small- and large spherical particle limits (Kokhanovsky, 2008). When  $x_\lambda \ll 1$ , we have Rayleigh scattering, leading to  $Q_s \propto 1/\lambda^4$ . When  $x_\lambda \gg 1$ , we find geometric optics, leading to  $Q_e \approx 2$  ( $C_e \propto r^2$ ). In the case of large weakly absorbing particles, it follows:  $Q_a \propto x_\lambda$  ( $C_a \propto r^3$ ). Accuracy control of Lorenz–Mie computations over the full range of  $x_\lambda$  and  $n_\lambda$  is a mature field but its fidelity to nature can be a legitimate concern.

If the particle is grossly non-spherical, the forward modeler will have to upgrade from a Lorenz–Mie code to one with non-spherical shape capability. In this realm, the main classes of solution are geometric optics (with or without interference effects) or Maxwell equation solvers (time-domain/finite-difference, T-matrix, Discrete Dipole Approximation, etc.); see Mishchenko et al. (1999). In this case, and apart from  $(r, \lambda, n)$ ,  $\mathbf{Z}$  will depend on both the incoming  $\Omega_i$  and outgoing  $\Omega_s$  directions, not just the scattering angle  $\cos^{-1}\Omega_i \cdot \Omega_s$ . There are also methods for accounting for the optical effects of small-scale roughness on the particle's surface (e.g., Kahnert et al., 2012).

### 3.3. Optical properties of aerosol populations with various particle size distributions

We are usually interested in a whole population of aerosol particles present in some volume of air. How many particles? What kind of

population? How big or small a volume? If non-spherical, are the particles randomly oriented?

Let  $N$  be the number density of aerosol particles, now of any radius  $r$ , per  $\text{cm}^{-3}$  in a “dilute” optical media, that is, where typical inter-particle distances ( $\approx N^{-1/3}$ ) are both  $\gg \lambda$  and  $\gg r$  (a representative value for the population such as its median or mode). That way, the particles are overwhelmingly often in each other’s far-fields in the sense of EM wave scattering and, assuming random positions, we can then average over real-valued intensities (hence cross-sections) rather than over complex-valued amplitudes (to account for phases and interference effects). Fortunately, even the most polluted atmospheres (where  $N \approx 10^{3+} \text{ cm}^{-3}$ ) are well within this regime. We also want volumes  $L^3$  such that  $NL^3 \gg 1$ ; that way, we can talk about statistically well-defined “populations,” even in the cleanest natural environments (where  $N \approx 10^{2-} \text{ cm}^{-3}$ ). Thus  $L$  in excess of a few cm seems adequate. At the same time, we want these elementary volumes to be small enough that even a single scattering or absorption event is a rare occurrence, hence  $NC_e(r, \lambda, n_\lambda) \times L \ll 1$  for the predominant values of  $r$ . We will see further on that is tantamount to asking that the elementary volume be optically thin. Even in the densest fogs, dust storms and smoke clouds, cm scales are still essentially transparent. As an extreme example, take  $N \approx 10^{3+} \text{ cm}^{-3}$  (dense particulates),  $C_e \approx 2\pi r^2$  ( $r \gg \lambda$ ),  $r \approx 10 \mu\text{m}$  (very large cloud-like particles), then one would need to take  $L \approx 1 \text{ m}$  for the product  $NC_eL$  to reach unity.

In remote sensing, aerosol particle size populations  $N(r)$ , usually expressed in  $\text{cm}^{-3} \mu\text{m}^{-1}$ , are invariably represented parametrically; log-normal distributions are by far the most popular, often with two modes, one coarse, one fine. This particle size distribution (PSD) is expressed as

$$N(r)dr = \left( N / \ln \sigma_g \sqrt{2\pi} \right) \exp \left( - \left[ \ln \left( r / r_g \right) / \ln \sigma_g \right]^2 / 2 \right) dr / r, \quad (3.6)$$

in the monomodal case. In the multimodal case, a weighted sum of two or more of such PSDs is used. Thus there are three microphysical parameters per PSD mode:  $N = \int N(r)dr$  (particle density, irrespective of size), the characteristic radius  $r_g$  (geometric mean of  $r$ ), and the log-standard deviation  $\sigma_g$  (a measure of PSD width). Statistical moments,  $\langle r^q \rangle = \int r^q N(r) dr / N$ , of the PSD are used extensively. For the lognormal model in Eq. (3.6), they are given by

$$\langle r^q \rangle (r_g, \sigma_g) = r_g^q \exp \left[ \left( q \ln \sigma_g \right)^2 / 2 \right], \quad (3.7)$$

hence the effective radius  $r_e = \langle r^3 \rangle / \langle r^2 \rangle = r_g \exp[(5/2)(\ln \sigma_g)^2]$ , and an alternative measure of PSD width known as effective variance  $v_e = \langle r^4 \rangle \langle r^2 \rangle / \langle r^3 \rangle^2 - 1 = \exp[(\ln \sigma_g)^2] - 1$ . In summary, we have five aerosol parameters per mode,  $\{N, r_g, \sigma_g, n_{\lambda r}, n_{\lambda i}\}$ , and all are legitimate remote sensing targets. For a given PSD, these properties are sufficient to generate the local values of the extinction, scattering and absorption coefficients, generally expressed in  $\text{km}^{-1}$ :

$$\sigma_{x\lambda} = N(C_x) (\lambda, n_\lambda; r_g, \sigma_g) = \int_0^\infty C_x(r, \lambda, n_\lambda) N(r; r_g, \sigma_g) dr \quad (3.8)$$

with  $x = e, s, a$ , where  $\langle \dots \rangle$  means, as for moments, an average over the PSD. By definition, the relative change in radiance  $\mathbf{I}_\lambda$  across a distance  $\delta \ell$  is given by  $\sigma_{e\lambda} \delta \ell$  in the absence of sources, cf. Eq. (3.2).

The differential scattering cross-section matrices and associated phase matrices are also averaged over the PSD. Viewed as optical counterparts of antenna radiation patterns in  $\theta_s$ , single-particle differential cross-sections, hence phase matrices, have highly variable interference-driven angular structure as soon as the non-dimensional size parameter  $x_\lambda$  exceeds a few tenths. Averaging over the PSD blurs this structure with one notable exception: the forward scattering peak at  $\theta_s = 0^\circ$  that is present for all values of  $x_\lambda$ . The backscattering (“glory”) peak at  $\theta_s = 180^\circ$  also persists, at least for spherical particles. Fig. 3.1 shows a selection of aerosol phase functions  $P_\lambda(\theta_s)$  as well as the Rayleigh phase

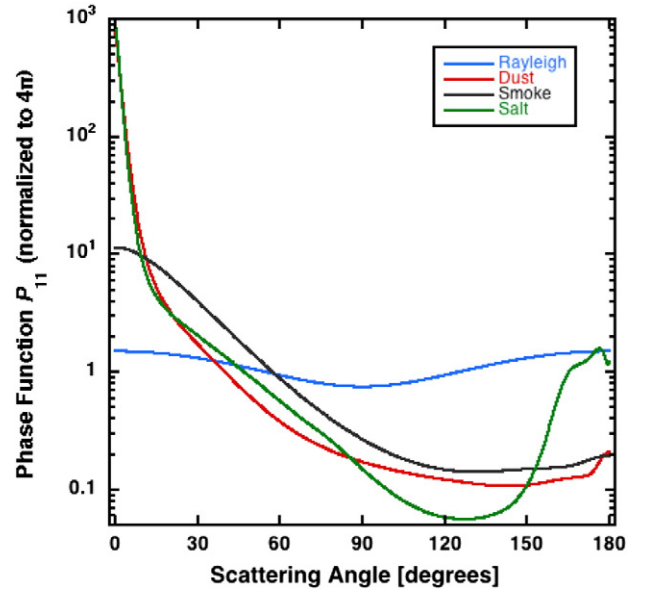


**Fig. 3.1.** Selected aerosol phase functions. Microphysical definitions of the particles are in Table 3.1. Spherical (smoke and salt) particles’ optical properties were generated using the Mie theory. Those of the non-spherical (dust) particles were obtained using the database generated by Dubovik et al. (2006). Wavelength is 446 nm.

function. We note that the phase function for the relatively coarse salt particles varies over almost 4 and 1/2 orders of magnitude. Table 3.1 displays the aerosol optical constants and the parameters of the particle size distribution used in calculations shown in Fig. 3.1.

Now, past the first scattering of natural sunlight coming from above or reflected by the surface below, the incoming light for the next scattering event can be in any state of polarization as described by the Stokes vector  $\mathbf{I}_\lambda = [I_\lambda, Q_\lambda, U_\lambda, V_\lambda]^T$ . Upon scattering, the outgoing light will generally be in an altered state of polarization determined by the  $4 \times 4$  phase matrix  $\mathbf{P}_\lambda(\theta_s)$ , including the phase function  $P_{\lambda 11}(\theta_s)$ . For spherical particles, the following symmetries apply:  $P_{\lambda 11}(\theta_s) = P_{\lambda 22}(\theta_s)$ ;  $P_{\lambda 44}(\theta_s) = P_{\lambda 33}(\theta_s)$ ;  $P_{\lambda 21}(\theta_s) = P_{\lambda 12}(\theta_s)$ ;  $P_{\lambda 43}(\theta_s) = -P_{\lambda 34}(\theta_s)$ ; and all other elements vanish identically. If the particles are non-spherical but randomly oriented, the set of phase matrix elements becomes  $\{P_{\lambda 11}, P_{\lambda 22}, P_{\lambda 33}, P_{\lambda 44}, P_{\lambda 12}, P_{\lambda 34}\}(\theta_s)$ , hence two more phase matrix elements to consider along the diagonal. The general structure of a phase matrix for randomly oriented nonspherical particles is therefore

$$\mathbf{P}_\lambda(\theta_s) = \begin{pmatrix} P_{\lambda 11}(\theta_s) & P_{\lambda 12}(\theta_s) & 0 & 0 \\ P_{\lambda 12}(\theta_s) & P_{\lambda 22}(\theta_s) & 0 & 0 \\ 0 & 0 & P_{\lambda 33}(\theta_s) & P_{\lambda 34}(\theta_s) \\ 0 & 0 & -P_{\lambda 34}(\theta_s) & P_{\lambda 44}(\theta_s) \end{pmatrix}. \quad (3.9)$$

**Table 3.1**

Microphysical properties of selected aerosol models. See Figs. 3.1–3.2 for scattering properties at the wavelength of 446 nm, and Fig. 3.4 for multiple scattering simulations. The calculations for the dust model have been done using Dubovik’s database (Dubovik et al., 2006). In this case, there was an equal mix of oblate and prolate spheroids with aspect ratios ranging between 4/3 and 3, and their inverses, with the most probable values being at the extremes. In real world situations sea salt and smoke aerosols may contain nonspherical particles as well (sea salt crystals and fractal aggregates of smoke particles).

Parameter	Shape	Aspect ratio	$r_g$ ( $\mu\text{m}$ )	$\sigma_g$	$r_e$ ( $\mu\text{m}$ )	$v_e$	$n_r$	$n_i$
“Smoke”	Sphere	Unity	0.060	0.549	0.148	0.433	1.518	0.02368
“Salt”	Sphere	Unity	1.000	0.549	2.460	0.433	1.550	0
“Dust”	Spheroid	Variable	3.285	0.539	8.550	0.466	1.502	0.00510

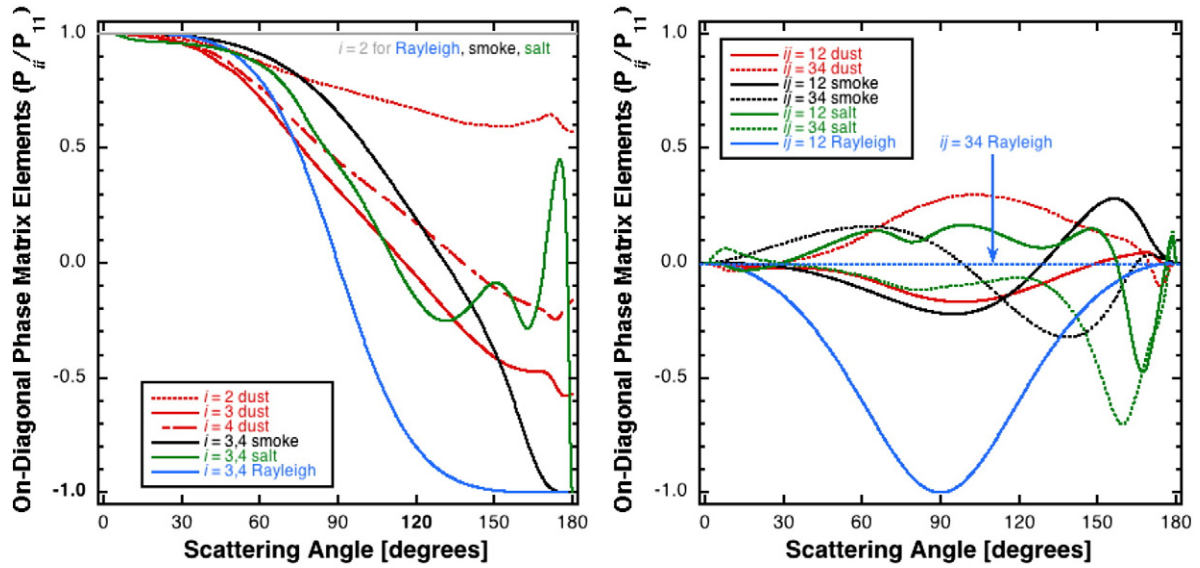


Fig. 3.2. Phase matrices of selected aerosol particles. As for Fig. 3.1, but for the diagonal (left) and off-diagonal (right) elements of the phase matrices. In both cases, the phase matrix elements are normalized by the first phase matrix element from Fig. 3.1.

Fig. 3.2 shows the non-vanishing  $P_{\lambda ij}(\theta_s)$  values, normalized by the phase function  $P_{\lambda 11}(\theta_s)$ , for the aerosols in Table 3.1, using  $P_{\lambda 11}(\theta_s)$  from Fig. 3.1. From the standpoint of polarimetry, the first off-diagonal element  $P_{\lambda 12}(\theta_s)$  is the only one that matters in the limit of single scattering for sunlight, which is unpolarized ( $Q_\lambda = U_\lambda = V_\lambda = 0$ ). Therefore, it is clear from Fig. 3.2 that Rayleigh scattering is by far more polarizing than scattering by any of the aerosols.

For the moment, the incoming and outgoing Stokes vectors have been evaluated in the scattering plane defined by  $\mathbf{\Omega}_{inc}$  and  $\mathbf{\Omega}_{out}$ . This is the most natural convention in laboratory studies and in computational models for EM wave scattering prediction. In remote sensing observations, however, the Stokes vector is generally evaluated in a convenient fixed frame, such as the North–South vertical plane or the principal plane (defined by the local vertical and the incident solar beam). In that case, a rotation is applied to move the incoming Stokes vector  $\mathbf{I}_{\lambda i}$  into the scattering plane, where Eq. (3.9) is applied, and then the scattered Stokes vector is rotated back into the reference plane, yielding  $\mathbf{I}_{\lambda s}$ . Conventionally, this matrix manipulation is denoted

$$\mathbf{I}_{\lambda s} = \mathbf{M}(\mathbf{\Omega}_{inc} \rightarrow \mathbf{\Omega}_{out}) \mathbf{I}_{\lambda i} = \mathbf{L}(\pi - \gamma_s) \mathbf{P}_\lambda(\theta_s) \mathbf{L}(-\gamma_i) \mathbf{I}_{\lambda i} \quad (3.10)$$

where the  $\gamma$ 's are the angles between the vertical planes containing the incoming and outgoing beams and the scattering plane. They are given

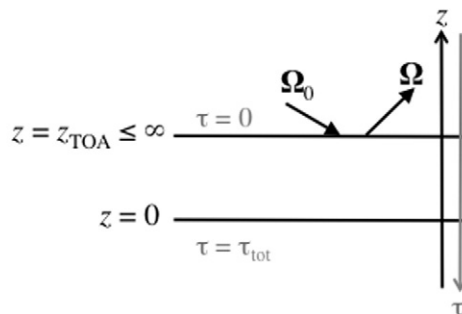
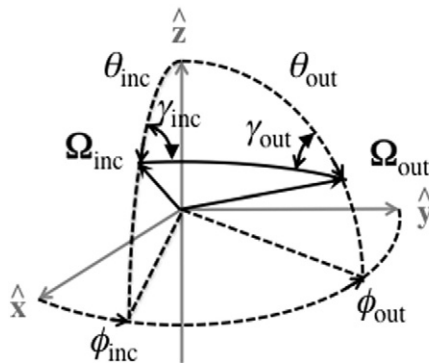


Fig. 3.3. Angular and spatial schematics. (Left) The scattering plane in regard to vertical planes is defined by incoming ( $\mathbf{\Omega}_{inc}$ ) and outgoing/scattered ( $\mathbf{\Omega}_{out}$ ) light beams. In the main text, they are represented in polar coordinates respectively as  $(\mu', \phi')$ , where  $\mu' = \cos\theta_{inc}$  and  $\phi' = \phi_{inc}$ , and similarly as  $(\mu, \phi)$ . The scattering angle  $\theta_s$  is formed between  $\mathbf{\Omega}_{inc}$  and  $\mathbf{\Omega}_{out}$ ; its cosine is given by  $\mu\mu' + (1 - \mu^2)^{1/2}(1 - \mu'^2)^{1/2}\cos(\phi' - \phi)$ . (Right) A schematic for RT in plane-parallel scattering media:  $z$  is the vertical coordinate (altitude) while  $\tau$  is optical depth going into the medium from the top, where solar radiation impinges on it (at the TOA) from direction  $\mathbf{\Omega}_0$ . Finally,  $\mathbf{\Omega}$  is the direction of the space-based sensor in which we wish to predict the outgoing Stokes vector.

by  $\cos\gamma_{inc} = (\mathbf{\Omega}_{inc} \times \hat{z}) \cdot (\mathbf{\Omega}_{inc} \times \mathbf{\Omega}_{out}) / (|\mathbf{\Omega}_{inc} \times \hat{z}| |\mathbf{\Omega}_{inc} \times \mathbf{\Omega}_{out}|)$ , where  $\hat{z}$  is the unit vector in the  $z > 0$  direction, and similarly for  $\pi - \gamma_{out}$  by swapping  $\mathbf{\Omega}_{inc}$  and  $\mathbf{\Omega}_{out}$ . The scattering angle  $\theta_s$  is given schematically and algebraically as a function of  $(\mathbf{\Omega}_{inc}, \mathbf{\Omega}_{out})$  in Fig. 3.3. The rotation matrix is defined as

$$\mathbf{L}(\alpha) = \begin{pmatrix} 1 & 0 & 0 & 0 \\ 0 & \cos 2\alpha & -\sin 2\alpha & 0 \\ 0 & \sin 2\alpha & \cos 2\alpha & 0 \\ 0 & 0 & 0 & 1 \end{pmatrix}. \quad (3.11)$$

The left schematic in Fig. 3.3 shows the various planes and angles used in the above.

### 3.4. Radiative transfer (RT) in the Earth's atmosphere

We now describe the “RT” stage, where the forward model gains the capability of accounting for all orders of scattering and, from there, the ability to predict the top-of-atmosphere (TOA) Stokes vectors measured by space-borne sensors. There are new scales to consider in a reasonably high-fidelity atmospheric RT model in terms of atmospheric structure. First, we plan to neglect horizontal variations of aerosol optical properties ( $\langle C_x \rangle$ 's) and aerosol loading and invoke the standard uniform

plane-parallel geometry. That is to say that the scales of horizontal aerosol variability will be assumed larger, and preferably much larger than scales of horizontal radiation transport. What are these scales?

Horizontal radiation transport has been studied extensively for stratiform clouds, largely with the same goal in mind of stating how uniform a cloud should be in this simplified representation. For clouds, the horizontal transport scale is defined as the root-mean-square (RMS) size of the cloud's point-spread function in reflection (Davis et al., 1997) or in transmission (Davis and Marshak, 2002), all orders of scattering included. In aerosol atmospheres, horizontal transport has not been investigated as well from that analytical standpoint. What has been extensively studied is the impact on a satellite remote sensing signal from a change in surface reflectivity at a finite distance from the ground target (Otterman and Fraser, 1979; Mekler and Kaufman, 1980; Otterman et al., 1980; Tanré et al., 1981; Kaufman, 1982; Diner and Martonchik, 1984a,b; Royer et al., 1988; Takashima and Masuda, 1992; Reinersman and Carder, 1995; Lyapustin, 2001; Lyapustin and Kaufman, 2001; Lyapustin and Knyazikhin, 2002; Richter and Schläpfer, 2002; Lyapustin et al., 2010; Semenov et al., 2011; Sterckx et al., 2011; Burazerovic et al., 2013; Jäkel et al., 2013). This is known as the “pixel adjacency effect,” and like all other 3D RT effects it is ignored in a 1D RT-based forward model. Another approach to horizontal variability scales is to consider the largely physiological notion of “visibility:” the horizontal range at which an observer can distinguish a dark object against the ambient light.

This can be translated to a standoff distance  $\ell_V = 3.92 / \sigma_e$  (for a physiologically relevant broad-band definition of extinction  $\sigma_e$ ), the important fact being that it varies inversely with  $\sigma_e$ . For aviation safety considerations,  $\ell_V$  in excess of 23 km is considered very clear while  $\ell_V$  less than 5 km is considered quite hazy. To ground this in RT theory, we recall that  $\delta I_\lambda / I_\lambda = -\sigma_{e\lambda} \delta \ell$  (in the absence of sources and in-scattering); from there, we easily obtain Beer's law of exponential light extinction with distance  $\ell$  from a source:

$$I_\lambda(\ell) = I_\lambda(0) \exp(-\sigma_{e\lambda} \ell), \quad (3.12)$$

which generalizes immediately to the case of a full Stokes vector. Therefore,  $1/\sigma_{e\lambda}$  is the characteristic or e-folding distance for (incoherent) light propagation over macroscopic scales in a uniform medium, a.k.a. photon mean-free-path. Technically, we should require that  $\sigma_{e\lambda}$  and other optical properties be horizontally uniform over scales  $\sim 1/\sigma_{e\lambda}$ . In other words, we should be safe over distances where the relative changes in  $\sigma_{e\lambda}$  are small. This certainly excludes “aerosol plume” scenarios, where  $\sigma_{e\lambda}$  makes large jumps. What the thresholds are for horizontal variability scales and for amplitudes in aerosol atmospheres remain open questions. Moreover, these questions need to be addressed from the standpoint of forward model accuracy and fidelity requirements to meet science goals.

Turning to the vertical dimension of the atmosphere, let  $H_p$  be the geometrical thickness of the aerosol layer (assumed uniform):  $N(z) \equiv \text{constant} > 0$  for the range  $0 \leq z \leq H_p$  and 0 for  $z > H_p$ . Alternatively,  $H_p$  can be the characteristic scale height if  $N(z)$  is assumed to decay exponentially in a half-space:  $N(z) = N(0) \exp(-z / H_p)$ . In both interpretations,  $H_p \approx 2$  km is a typical value and, either way, the non-dimensional aerosol optical thickness (AOT) of the atmosphere is

$$\tau_\lambda^{(p)} = \int_0^\infty \sigma_{e\lambda}^{(p)}(z) dz = \langle C_e \rangle (\lambda, n_\lambda; r_g, \sigma_g) \int_0^\infty N(z) dz = \sigma_{e\lambda}^{(p)}(0) H_p, \quad (3.13)$$

if  $\langle C_e \rangle (\lambda, n_\lambda; r_g, \sigma_g)$  is assumed constant since that leads to  $\sigma_{e\lambda}^{(p)}(z) = \sigma_{e\lambda}^{(p)}(0) \exp(-z / H_p)$ . Here  $\sigma_{e\lambda}^{(p)}(0) = \langle C_e \rangle (\lambda, n_\lambda; r_g, \sigma_g) N(0)$  is the ground-level value of aerosol extinction (superscript “p” for particulate), as used implicitly in the above estimate of horizontal visibility  $\ell_V$ . AOTs, for both fine and coarse modes, are better extensive measures of aerosol burden than the associated  $N(0)$  or  $\sigma_{e\lambda}^{(p)}(0)$  in a stratified atmosphere, at

**Table 3.2**

Scale-aware summary of aerosol properties. First come those aerosol parameters contained in the 10-dimensional vector  $\mathbf{x}$  of unknowns (5 per mode) in the remote sensing inverse problem; they are followed by two other quantities that may also matter. Note that AOT at a reference wavelength, generally 550 nm, determines all the others through the microphysics.

Parameter	Symbol	Units	Range	Modes	Scale
Index of refraction (real part)	$n_r$	–	1.33–1.65	Fine & coarse	Micro
Index of refraction (imaginary part)	$n_i$	–	0–0.05		
Characteristic radius (geometric mean)	$r_g$	$\mu\text{m}$	0.03–5		
Log-standard deviation	$\sigma_g$	–	0.2–1.5		
Aerosol optical thickness	$\tau^{(a)}$	–	0–5		Macro
Layer's physical thickness/scale height	$H_p$	km	1–5		
Layer's base altitude	$z_{\text{base}}$	km	0.5–4.5		

least for remote sensing and radiation budget (climate) considerations. One reason for that is the considerable interest in situations where the aerosol may be lofted into a layer between  $z_{\text{base}} > 0$  and  $z_{\text{top}} = z_{\text{base}} + H_p$ , so  $\tau_\lambda^{(p)} > 0$  even though  $N(0) = 0$  and  $\sigma_{e\lambda}^{(p)}(0) = 0$ . Table 3.2 shows a scale-by-scale summary for all the aerosol properties contained in the vector  $\mathbf{x}$  of unknowns in the remote sensing inverse problem, and a few others that matter.

At shorter wavelengths, Rayleigh scattering becomes an increasingly strong contributor to the Stokes vector since Rayleigh optical depth  $\tau_\lambda^{(R)}$  will eventually exceed  $\tau_\lambda^{(p)}$ . Recall that  $\tau_\lambda^{(R)} \propto 1 / \lambda^4$  while the Angstrom exponent  $\alpha$  in  $\tau_\lambda^{(p)} \propto \lambda^{-\alpha}$  hovers around unity for most aerosols. Moreover, molecules and particulates are stratified differently; specifically, we can use, to high accuracy,  $\sigma_{e\lambda}^{(R)}(z) = \sigma_{e\lambda}^{(R)}(0) \exp(-z / H_m)$ , where  $\sigma_{e\lambda}^{(R)}(0) = \tau_\lambda^{(R)} / H_m$  and the atmospheric pressure scale height  $H_m \approx 8$  km is significantly larger than  $H_p$ . Consequently, we will need to define optical properties (extinction, scattering and absorption coefficients, along with phase matrices) in continuously varying aerosol-Rayleigh mixtures. For instance, introducing the aerosol single scattering albedo (SSA),  $\omega_{0\lambda}^{(p)} = \sigma_{s\lambda}^{(p)} / \sigma_{e\lambda}^{(p)}$ , we have

$$\omega_{0\lambda}(z) = \sigma_{s\lambda}(z) / \sigma_{e\lambda}(z) = \left[ \omega_{0\lambda}^{(p)} \sigma_{e\lambda}^{(p)}(z) + \omega_{0\lambda}^{(R)} \sigma_{e\lambda}^{(R)}(z) \right] / \left[ \sigma_{e\lambda}^{(p)}(z) + \sigma_{e\lambda}^{(R)}(z) \right] \quad (3.14)$$

for the mixture, where the Rayleigh counterpart  $\omega_{0\lambda}^{(R)}$  can generally be taken as unity (no molecular absorption) in multispectral aerosol remote sensing applications. The denominator  $\sigma_{e\lambda}(z)$  in Eq. (3.14) is the total extinction coefficient for the mixture. In the same vein, we have

$$\mathbf{P}_\lambda(\theta_s) = [1 - f_R(z)] \mathbf{P}_\lambda^{(p)}(\theta_s) + f_R(z) \mathbf{P}_\lambda^{(R)}(\theta_s), \quad (3.15)$$

where  $f_R(z)$ , the height-dependent Rayleigh scattering fraction, is

$$f_R(z) = \sigma_{e\lambda}^{(R)}(z) / \left[ \omega_{0\lambda}^{(p)} \sigma_{e\lambda}^{(p)}(z) + \sigma_{e\lambda}^{(R)}(z) \right], \quad (3.16)$$

under the explicit assumption that  $\omega_{0\lambda}^{(R)} = 1$ . “External” mixtures of aerosols of different types present in the scattering volume are treated in the same fashion. Examples are a mixture of fine (or “accumulation”) mode aerosols and a coarse mode, or a local “background” aerosol and a very different kind of aerosol transported from a distant source.

The Rayleigh phase matrix  $\mathbf{P}_\lambda^{(R)}(\theta_s)$  introduced in the above is given by these non-vanishing elements:

$$\begin{aligned} P_{11\lambda}^{(R)}(\mu_s) &= P_{22\lambda}^{(R)}(\mu_s) = (3/4) \Delta_\lambda (1 + \mu_s^2), \\ P_{12\lambda}^{(R)}(\mu_s) &= P_{21\lambda}^{(R)}(\mu_s) = -(3/4) \Delta_\lambda (1 - \mu_s^2), \\ P_{33\lambda}^{(R)}(\mu_s) &= (3/2) \Delta_\lambda \mu_s, \\ P_{44\lambda}^{(R)}(\mu_s) &= \Delta_\lambda \Delta'_\lambda P_{33\lambda}^{(R)}(\mu_s), \quad \text{and} \\ P_{34\lambda}^{(R)}(\mu_s) &= P_{43\lambda}^{(R)}(\mu_s) = 0, \end{aligned} \quad (3.17)$$

where  $\mu_s = \cos\theta_s$ ,  $\Delta_\lambda = (1 - \delta_\lambda) / (1 + \delta_\lambda / 2)$  and  $\Delta_\lambda^\lambda = 1 - \delta_\lambda / (1 - \delta_\lambda)$ , with  $\delta_\lambda$  denoting the Rayleigh depolarization factor. If there is sufficient contrast between the aerosol and Rayleigh optical properties, aerosol particles could be coarsely profiled (by inferring  $z_{\text{base}}$  and  $H_p$ ) using purely passive remote sensing methods (Kalashnikova et al., 2011).

The final ingredient of the forward model is the vector RT equation (vRTE), and associated boundary conditions (BCs), and a practical solution thereof. The general vRTE describes the detailed balance between sources and sinks of radiation in 5-dimensional “transport” space. Transport space contains all  $(\mathbf{r}, \mathbf{\Omega})$  pairs of 3D position vectors  $\mathbf{r} = (x, y, z)^T$  and, introducing polar coordinates, unitary propagation direction vectors  $\mathbf{\Omega}(\theta, \phi)$ . In the absence of horizontal variability of the optical properties and/or sources, we restrict ourselves to the three independent variables  $(z, \theta, \phi)$  of so-called “1D” vRT. Radiation sinks for a light beam  $\mathbf{\Omega}$  going through level  $z$  are the removal of radiant energy by:

- (1) extinction, described by  $\sigma_{\text{ex}}(z)\mathbf{I}_\lambda(z, \mu, \phi)$ ; and
- (2) advection out of the elementary volume, described by  $\mathbf{\Omega} \cdot \nabla \mathbf{I}_\lambda \equiv \mu \partial \mathbf{I}_\lambda / \partial z$ ,

where  $\mu = \cos\theta$  is the vertical component of  $\mathbf{\Omega}_z$ . In the solar spectrum, the only source of diffuse radiance for a given light beam is in-scattering of radiant energy propagating in other directions; this process is described at height  $z$  by the double angular integral

$$\sigma_{\text{s}\lambda}(z) \int_0^{2\pi} \int_{-1}^{+1} \mathbf{M}_\lambda(z, \mu', \phi' \rightarrow \mu, \phi) \mathbf{I}_\lambda(z, \mu', \phi') d\mu' d\phi' / 4\pi \quad (3.18a)$$

over all incoming directions. In summary, we have the following integro-differential vRTE to solve,

$$\begin{aligned} & [\mu \partial / \partial z + \sigma_{\text{ex}}(z)] \mathbf{I}_\lambda(z, \mu, \phi) \\ & = \sigma_{\text{s}\lambda}(z) \iint \mathbf{M}_\lambda(z, \mu', \phi' \rightarrow \mu, \phi) \mathbf{I}_\lambda(z, \mu', \phi') d\mu' d\phi' / 4\pi, \end{aligned} \quad (3.18b)$$

for  $\mathbf{I}_\lambda(z, \mu, \phi)$  on the domain  $(0, z_{\text{TOA}}) \times [-1, +1] \times (0, 2\pi)$  where  $z_{\text{TOA}}$  is between  $z_{\text{top}} (\geq H_p)$  and  $\infty$ .

Before discussing numerical solutions of the 1D vRTE in (3.18), we have to question its derivation sketched in the above. Although we have high confidence in the validity of vRT theory—at least its full 3D version—in atmospheric optics, the above rationale is a purely phenomenological argument based on radiant energy conservation, as applied to a “light beam.” Should this vRTE not follow from Maxwell’s equations for EM waves? It does, and has been proven rigorously (Mishchenko, 2002, 2014). The new derivation is grounded in statistical optics and makes clear the above-stated requirements on the light scattering medium, and some new ones such as “ergodicity.” Particles must be positioned randomly in space in each other’s far field. In other words, the light scattering medium must be dilute and, in principle, (statistically) uniform.

It is customary to use optical depth from the TOA,

$$\tau_\lambda(z) = \int_z^{z_{\text{TOA}}} \sigma_{\text{ex}}(z') dz', \quad (3.19)$$

in lieu of the vertical coordinate  $z$  in the 1D vRTE in Eq. (3.14). This change of variable leads to

$$\begin{aligned} & [-\mu \partial / \partial \tau_\lambda + 1] \mathbf{I}_\lambda(\tau_\lambda, \mu, \phi) \\ & = \varpi_{0\lambda}(\tau_\lambda) \iint \mathbf{M}_\lambda(\tau_\lambda, \mu', \phi' \rightarrow \mu, \phi) \mathbf{I}_\lambda(\tau_\lambda, \mu', \phi') d\mu' d\phi' / 4\pi, \end{aligned} \quad (3.20)$$

where  $\mu > 0$  still means up-welling and  $\mu < 0$  down-welling radiances. However, while  $z$  can in principle go to  $\infty$ , the range of  $\tau_\lambda$  is always finite, namely, the interval  $(0, \tau_{\lambda 0})$ , where  $\tau_{\lambda 0} = \tau_\lambda(0) = \tau_\lambda^{(p)} + \tau_\lambda^{(R)}$ . The function  $\tau_\lambda(z)$  in Eq. (3.19) decreases monotonically, so it can be inverted at least numerically to give altitude  $z$  as a function of  $\tau_\lambda$ , the

independent variable in Eq. (3.20). That map in turn enables the construction of the optical properties as prescribed functions of  $\tau_\lambda$ , namely,  $\varpi_{0\lambda}(\tau_\lambda)$  and  $\mathbf{M}_\lambda(\tau_\lambda, \dots)$ .

The computational problem at hand is not completely defined without the applicable BCs. See schematic in Fig. 3.3. In the present formulation there are no volume sources, but the incoming Stokes vector field must satisfy specific constraints at both upper and lower boundaries:

(1)

$$\mathbf{I}_\lambda(0, \mu, \varphi) = [F_{0\lambda}, 0, 0, 0]^T \delta(\mu + \mu_0) \delta(\phi) \quad (3.21a)$$

for  $-1 \leq \mu < 0$  ( $\pi/2 < \theta \leq \pi$ ) at the TOA ( $z = z_{\text{TOA}}$ ,  $\tau_\lambda = 0$ ), where  $\mu_0$  is (the absolute value of) the cosine of the solar zenith angle (SZA), taking  $\mathbf{\Omega}_0 = \mathbf{\Omega}(-\mu_0, 0)$ , and letting  $F_{0\lambda}$  be the spectral solar irradiance for the precise Earth–Sun distance at the time of observation; and

(2)

$$\mathbf{I}_\lambda(\tau_{\lambda 0}, \mu, \phi) = \int_0^{2\pi} \int_{-1}^0 \rho_\lambda(\mu', \phi' \rightarrow \mu, \phi) \mathbf{I}_\lambda(\tau_{\lambda 0}, \mu', \phi') |\mu'| d\mu' d\phi' \quad (3.21b)$$

for  $0 < \mu \leq +1$  ( $0 \leq \theta < \pi/2$ ) at the lower boundary ( $z = 0$ ,  $\tau_\lambda = \tau_{\lambda 0}$ ), where  $\rho_\lambda(\mu', \phi' \rightarrow \mu, \phi)$  is a given matrix that we call the bidirectional reflectance distribution matrix (BRDM), by extension from the scalar case where only  $I_\lambda$  is of interest and we specify only a bidirectional reflectance distribution function (BRDF).

Aerosol remote sensing is almost invariably conducted under conditions where the atmosphere is optically thin enough to see the surface through the haze (small AOT), which means that said surface has to be quite carefully represented in the forward model. Several parametric models for the surface reflectance have been used successfully for this requirement, and they are described in detail in the technical Appendix A section at the end of this review.

This completes the description of the computational vRT problem to be solved. We will describe numerical solution techniques after introducing quantities derived from the Stokes vector that are commonly used in remote sensing.

### 3.5. Observable reflected light field characteristics

The standard format for comparison of forward model predictions at TOA with well-calibrated space-based observations is the normalized Stokes vector (NSV)

$$\mathbf{S} = \pi \mathbf{I}(0, \mathbf{\Omega}_i) / \mu_0 F_0, \quad (3.22)$$

with the elements  $[R, q, u, v]^T$  for a finite number of directions  $\{\mathbf{\Omega}_i, i = 1, \dots, N_\Omega \geq 1\}$  with  $0 < \mu_i \leq 1$ . Note that the first component of the NSV,  $\pi I(0, \mathbf{\Omega}_i) / \mu_0 F_0$ , is known as the “bidirectional reflectance factor” or BRF. The physical interpretation of the BRF is as follows.

Assume there is no atmosphere, so that the whole RT problem is contained in Eqs. (3.21a) and (3.21b), and that the BRDM is for a depolarizing Lambertian (i.e., isotropically reflecting) surface for which the  $\rho_{\lambda 11}$  (BRDF per se) is  $\alpha_\lambda / \pi$ , where  $\alpha_\lambda \in [0, 1]$  is the spherical albedo of the surface, and all the other elements are 0. Then the down-welling intensity in Eq. (3.21b) is given by Eq. (3.21a). The angular integral over the down-welling  $2\pi$  sr in the lower BC then yields  $\mu_0 F_{0\lambda}$ . If we now treat  $\alpha_\lambda$  as an unknown it can be obtained from the data (up-welling  $I_\lambda$ , uniform across directions) as  $\pi I_\lambda / \mu_0 F_{0\lambda}$ . The observed or predicted BRF value is therefore the effective Lambertian albedo that would yield  $I_\lambda(0, \mathbf{\Omega})$ , for a given  $\mathbf{\Omega}$ , in the absence of a scattering

atmosphere; the other components of the NSV are conveniently non-dimensionalized in the same manner.

A combination of great interest is the degree of linear polarization, considered here across wavelengths. As an alternative to the 2nd and 3rd elements of the Stokes vector,  $\text{DOLP}_\lambda = (Q_\lambda^2 + U_\lambda^2)^{1/2} / I_\lambda$  is complemented with the angle of linear polarization (AOLP),

$$\text{AOLP}_\lambda = \tan^{-1}(U_\lambda/Q_\lambda)/2, \quad (3.23)$$

where  $\tan^{-1}(\cdot)$  accounts for the signs of  $U_\lambda$  and  $Q_\lambda$ , thus taking values from 0 to  $2\pi$ . Neither  $\text{DOLP}_\lambda$  nor  $\text{AOLP}_\lambda$  care about the whether NSV or, as implied here, the original Stokes components are used. Finally, one can define polarized radiance

$$I_{\lambda p} = (Q_\lambda^2 + U_\lambda^2 + V_\lambda^2)^{1/2}, \quad (3.24)$$

which is necessarily  $\leq I_\lambda$ . Sometimes,  $V_\lambda$  is dropped from Eq. (3.24) in view of its small magnitude in atmospheric optics, in which case,  $I_{\lambda p} = \text{DOLP}_\lambda \times I_\lambda$ , which is called *linearly polarized radiance* or polarization difference because  $I_{\lambda p} \equiv Q$  at  $U_\lambda = V_\lambda = 0$ , and the value of  $Q$  is just the difference of the intensities of scattered light polarized perpendicular and parallel to a given plane (say, scattering plane).

### 3.6. Computational techniques for solving the vector radiative transfer equation

#### 3.6.1. Formulations, transformations and numerical methods

Computational techniques for solving numerically the 1D vRT problem are out of scope for the present review, so we only point here to the relevant literature. It suffices to state that they are remarkably diverse in their approaches, ranging from straightforward Monte Carlo schemes (e.g., Marchuk et al., 1980) to sophisticated implementations of deterministic methods (Kokhanovsky et al., 2010b). The latter invariably start with a (truncated) Fourier series decomposition in the azimuthal angle. Translational invariance of the RT problem in the  $(x, y)$ -plane (1D vs. 3D RT) means that each mode is decoupled from the others. These independent Fourier mode coefficients each obey a simpler 1D vRTE that is discretized in the polar angle using discrete ordinates (e.g., Stamnes et al., 1988; Spurr, 2006; Rozanov et al., 2014) or spherical harmonics (e.g., Lyapustin et al., 2010; Korokin et al., 2013).

The forward scattering peak in the phase function of many interesting aerosol types (cf. Fig. 3.1) is a particular challenge for truncated and discretized direction spaces; this calls for special phase function decomposition and rescaling techniques (e.g., Potter, 1970; Wiscombe, 1977; Nakajima and Tanaka, 1988). The resulting system is either reduced to the coupled ordinary differential equations with prescribed BCs, which can be solved using eigenvalue methods, or to a discretized integral equation. In the latter case, one can solve the problem by source iteration (a.k.a. successive orders-of-scattering) (e.g., Hasekamp and Landgraf, 2002; Kotchenova et al., 2006; Kotchenova and Vermote, 2007; Zhai et al., 2009), or using Markov chain formalism (e.g., Xu et al., 2011a, 2011b, 2012). Alternatively, adding/doubling (e.g., Hansen, 1971a,b; Hansen and Travis, 1974; Wiscombe, 1976; De Haan et al., 1987; Evans and Stephens, 1991; Liu and Weng, 2006) or matrix-operator (e.g., Nakajima and Tanaka, 1986; Liu and Ruprecht, 1996; Sanghavi et al., 2013, 2014) methods can be implemented, following the general principles of invariant embedding in discrete spaces (Preisendorfer, 1965; Grant and Hunt, 1969a,b; van de Hulst, 1980). It is notable that these strategies are at their most diverse when applied to optically uniform layers; the need to address stratification tends to spawn hybrid computational models, with (layer) adding being the last step. With unlimited computational resources (in both core memory and computer time) and proper implementation, all of these approaches to realistic

numerical 1D vRT problems can be brought into arbitrarily close agreement. However, in practical situations, deviations of up to  $\sim 1\%$  can be expected. In view of radiometric error ( $\approx 3\%$ ) and unavoidable fidelity error (e.g., 3D RT effects not included in 1D RT models), that may be sufficient.

#### 3.6.2. Illustration with a current challenge in continuously-varying stratified atmospheres

Fig. 3.4 illustrates forward modeling for a multi-angle spectropolarimeter concept using the “dust” model from Table 3.1 and a Monte Carlo code. There is a constant background of conservative Rayleigh scattering following an exponential extinction profile with a characteristic scale height  $H_m = 8$  km. Two wavelengths are considered: 446 nm (blue) and 354 nm (near UV) that lead respectively to Rayleigh optical depths of 0.231 and 0.593 (at normal atmospheric pressure), and a Rayleigh depolarization factor  $\delta_\lambda = 0.029$  is used. The strongly absorbing dust layer (cf. Table 3.1, leading to the single scattering albedo equal to 0.838) is either lofted to 3–5 km altitude ( $z_{\text{base}} = 3$  km,  $H_p = 2$  km), presumably in the course of long-range transport, or confined to the planetary boundary layer (0–2 km); in both cases, it has a uniform aerosol extinction profile corresponding to AOT = 0.5. The sun is at  $60^\circ$  from zenith, and the underlying surface is black. The non-vanishing elements of the NSV at TOA in the principal plane are plotted, namely,  $I$  and  $Q$  for  $(\tau, \theta, \varphi) = (0, \theta, 0)$  and  $(0, -\theta, \pi)$ , where  $\theta$  is the viewing zenith angle (VZA) is set to  $0.0^\circ, \pm 26.1^\circ, \pm 45.6^\circ, \pm 60.0^\circ$ , and  $\pm 70.5^\circ$  (based on the nominal MISR view angles) with  $>0$  meaning  $\varphi = 0$  and  $<0$  for  $\varphi = \pi$ .

It is clear in Fig. 3.4 that the difference in signal between the two profiles is significantly larger than a conservative estimate of instrumental error (3%), which is certainly an upper bound for forward model error. Consequently, a wrong assumption about aerosol layer height would lead in this case to unacceptable forward model error. Kalashnikova et al. (2011) analyzed in detail sensitivities of multi-angle spectropolarimetric measurements to aerosol layer height at wavelengths, where Rayleigh scattering contributes significantly to the observed Stokes vector. In particular, in Fig. 3.4, we can see that for discriminating the boundary layer and lofted aerosol scenarios on the basis of DOLP, the blue wavelength is just as effective as its UV counterpart.

#### 3.6.3. Intercomparison of three forward models

Fig. 3.5 shows an intercomparison of three 1D vRT models listed in Table 3.3. As in Fig. 3.4,  $I$  and  $Q$  in the principal plane are used, now for VZA sampled every  $3^\circ$  (59 points). Two test cases are considered: the atmosphere contains the sea salt aerosol only (no molecular scattering) from Table 3.1, and the surface is either black or Lambertian with an albedo of 0.2; in short, we take  $a = 0$  or  $0.2, k = 1, b = 0$ , and  $\zeta = 0$  in the parametric model described in the Appendix A. The top two panels show on the same scale  $\pi I(0, \theta, 0) / \mu_0 F_0$  and  $\pi Q(0, \theta, 0) / \mu_0 F_0$  for these two surface scenarios obtained from the reference Monte Carlo (MC) scheme run at very high precision ( $10^8$  histories) and with no discretization beyond the tabulation of the phase matrix used as input ( $0.25^\circ$  intervals in the scattering angle). For instance, a rejection method was used to decide what new direction the random path would take instead of a secondary tabulation for the inverse cumulative phase function integral. The remaining 4 panels show “model-MC” plots for two models: MarCh, a Markov Chain model (Xu et al., 2011a,b) in green, and SCIATRAN (Rozanov et al., 2014), which is based on discrete ordinates, in red. MC error is also plotted with dashed lines.

Intensity differences in the middle panels show that the agreement is quite good. All differences are less than 1%. Relative 1% is actually a reasonable accuracy goal to request of models and modelers, and the horizontal axes in the middle plots have  $\pm 1\%$  as upper and lower bounds on their vertical axes. Indeed, forward model error should be small compared to the measurement uncertainty of a typical instrument recording radiometry. Often 3% is advanced as a number for radiometric calibration error. However, calibration error is not a random number taking independent values for every different angle and spectral

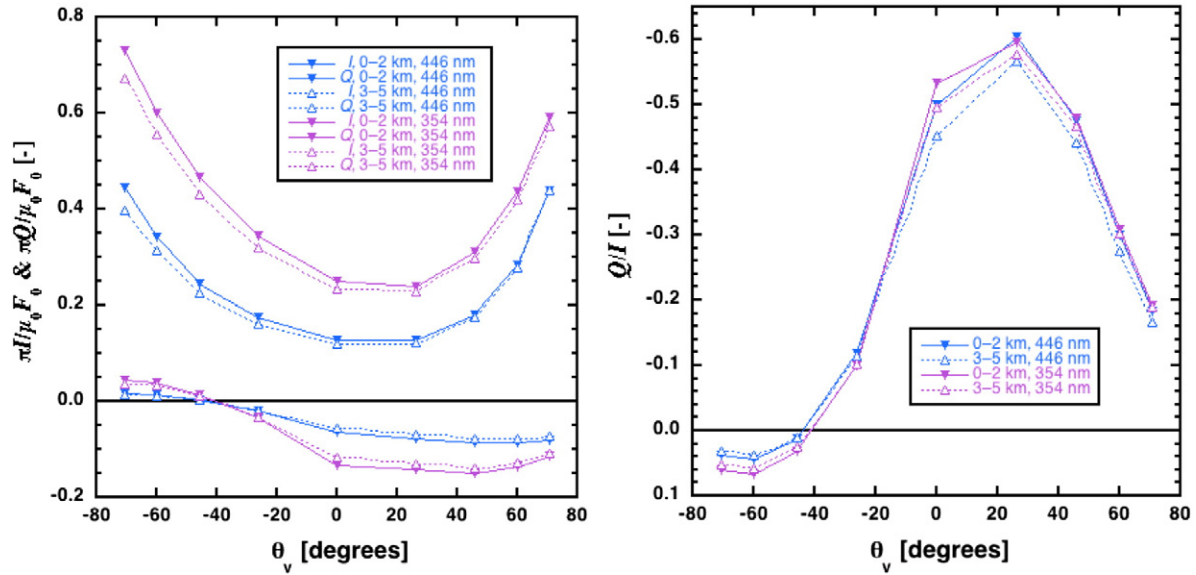


**Fig. 3.4.** Synthetic multi-angle radio-polarimetric observations from space of a vertically variable atmosphere above a black surface. There is a constant background of conservative Rayleigh scattering following an exponential extinction profile with a characteristic scale height  $H_m = 8$  km. Two wavelengths are considered: 446 nm (blue) and 354 nm (near UV) that lead respectively to Rayleigh optical depths of 0.231 and 0.593 (at normal atmospheric pressure), and Rayleigh depolarization factor  $\delta_{\lambda} = 0.029$ . The strongly absorbing dust layer (cf. Table 3.1, leading to the single scattering albedo  $\delta_{\lambda} = 0.838$ ) is either lofted to 3–5 km altitude ( $z_{\text{base}} = 3$  km,  $H_p = 2$  km), or confined to the planetary boundary layer (0–2 km); in both cases, it has a uniform aerosol extinction corresponding to AOT = 0.5. The sun is at  $60^\circ$  from zenith, and the underlying surface is black. (Left) Radiances for a dust aerosol layer at two levels as a function of viewing angle in the principal plane, where a positive viewing angle means azimuth of  $0^\circ$  and a negative one means  $180^\circ$ . (Right) Same as left panel but for  $Q/I$ , the absolute value of which is DOLP since  $U = 0$  in the principal plane. The peak in  $Q/I$  occurs at  $\theta_s = 120^\circ - \theta_v \approx 90^\circ$ , as expected from the single scattering estimation of  $P_{12}/P_{11}$  for Rayleigh scattering in Fig. 3.2. We can see that for discriminating the boundary layer and lofted aerosol scenarios on the basis of DOLP, the blue wavelength is just as effective as its UV counterpart (Kalashnikova et al., 2011).

channel and polarization state. Rather it drifts slowly during a period and is occasionally reset to a large extent by performing on-orbit calibration procedures. The truly random part of the radiometric uncertainty is probably closer to 1.5 to 2%. On the other hand, 1D vRT models have a fundamental fidelity limitation with respect to the 3D vRT unfolding in nature. It is doubtful that nature is ever compliant with the horizontal uniformity assumption at better than relative 1% in the observations. Anyway, to achieve this 1% accuracy, MarCh was run with 70 Gaussian quadrature points for the each of the 4 quadrants and each of the 35 azimuthal Fourier terms. On the other hand, no “delta-truncation” of the forward peak was implemented. SCIATRAN’s numerical control parameters were similar. We even note that the two deterministic models track each other in their fluctuations across the 59 direction samples, especially for the black surface.

Differences in the (signed) DOLP, the ratio  $Q/I$ , are displayed in the lower panels of Fig. 3.5. They also show a high degree of correlation between the angular fluctuations of MarCh and SCIATRAN differences with the MC reference data. MarCh–SCIATRAN differences remain smaller than or on the order of the MC errors. For DOLP, the desirable and achievable upper bound on instrumental uncertainty is often cited as 0.005 (0.5% absolute). All three models shown here are already doing much better since  $\pm 0.005$  is about a half of the full range of the error plots.

Finally, it is clear that, for remote sensing applications at least, 1D vRTE solution methods that manipulate only the required Stokes vectors at TOA are at an advantage in terms of computer memory vis-à-vis their counterparts that compute the Stokes vector field throughout the light scattering medium. MC is one such vRTE solution but there are computationally efficient deterministic vRTE solutions as well. That advantage in speed can be re-invested, e.g., in enhanced fidelity. By the same token, it is highly desirable to have forward models that have been “linearized,” i.e., that efficiently and accurately compute the Jacobian matrix  $\partial \mathbf{F} / \partial \mathbf{x}$  along with  $\mathbf{F}(\mathbf{x})$  without resorting to finite differences, which are risky and costly. These linearized models can be used

in sensitivity studies (e.g., Hasekamp and Landgraf, 2007) that could be extended to instrument design support. Most importantly, accurate estimates of  $\partial \mathbf{F} / \partial \mathbf{x}$  can be used in optimization approaches for solving the inverse problem (e.g., Rodgers, 2000).

Most 1D codes do calculations that would allow the internal fields to be constructed, e.g., Discrete Ordinates (e.g., Stamnes et al., 1988) and (with a little more effort) Doubling/Adding (e.g., Hansen and Travis, 1974). The construction of internal fields has negligible overhead and they can then be used in calculating Jacobians. For Discrete Ordinates as many calculations as view angles are required for the adjoints, but the eigenvector problem only has to be solved once. For Doubling/Adding a single run gives the internal fields and their adjoints including adjoints for any internal observation level (e.g., aircraft or AERONET).

This concludes our high-level description of how a physics-based forward model  $\mathbf{F}(\mathbf{x})$  is computed, with an emphasis on the *potentially wrong* assumptions made along the way and on the computational challenge of getting the predicted sensor signal accurate with respect to a high-precision Monte Carlo result. We next discuss how the inverse problem is addressed in practical remote sensing situations, with the understanding that forward model error, either in fidelity of representation of the atmospheric state or in numerical computation, is a liability that has been assessed.

#### 4. Solution of the inverse problem

In this section we review the algorithms developed to retrieve aerosol properties from multi-angle photo-polarimetric measurements that are published in peer-reviewed literature. We restrict ourselves to algorithms that are developed for aerosol retrieval in clear sky scenes. Efforts to retrieve aerosol properties above, below or between clouds are also known (references and discussion in concluding section). Furthermore, we restrict ourselves to the version of the different

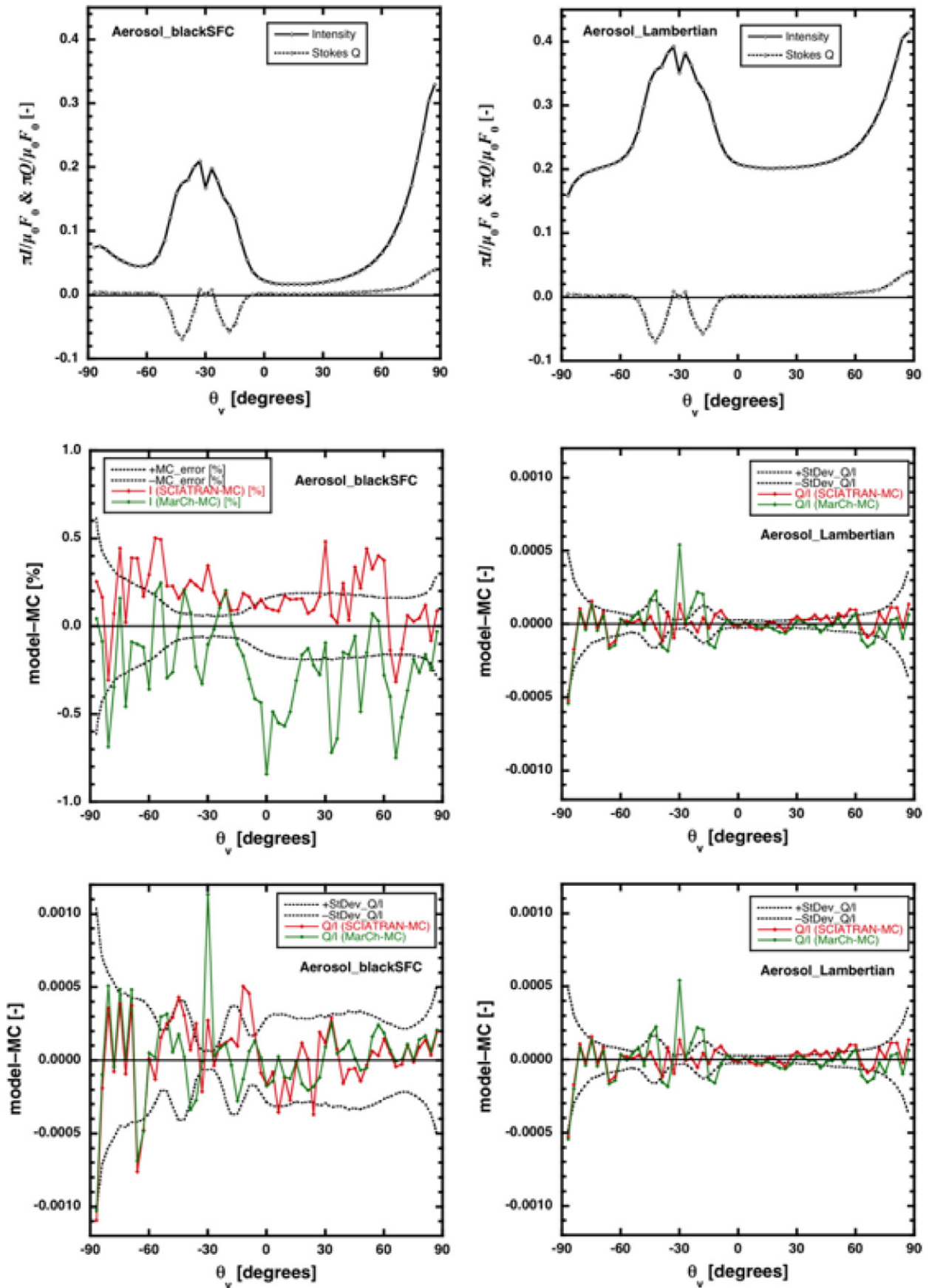


**Fig. 3.5.** Comparison of four multiple scattering forward 1D vRT models. The atmosphere is made of a pure non-absorbing salt particles from Table 3.1, with an AOT of 0.5. On the left-hand side, the surface is black and, on the right-hand side, it is Lambertian (hence depolarizing) with an albedo of 0.2. The sun is at 30° from zenith. The top row shows  $I$  and  $Q$  as functions of viewing angle in the principal plane (where  $U$  vanishes), using the same sign convention for viewing zenith angle as used in Fig. 3.3. The middle row shows differences between the deterministic models and the Monte Carlo estimate for intensity  $I$ , along with Monte Carlo error bars (one standard deviation). The bottom row shows the same as the middle one, but for  $Q/I$ .

algorithms as described in the respective publications—unpublished newer developments are not considered here. The main characteristics of the algorithms are given in Table 4.1.

#### 4.1. Number of measurements versus number of parameters to be retrieved

Given an instrument with  $N$  wavelengths (all of which are assumed to have some level of aerosol/surface utility), of which  $N_p$  have polarization capability, there are

$$M = N_{\Omega} \times (N + 2N_p), \quad (4.1)$$

observations when, as is customary, only  $I$ ,  $Q$  and  $U$  are measured ( $V$  being very small).  $N_{\Omega}$  is the number of angular measurements. To keep the retrieval problem mathematically well-posed,  $M$  has to be larger—and preferably much larger—than the number of retrieval parameters  $m$ . To get an idea of  $M$ 's magnitude, imagine that we want to characterize a bimodal aerosol model (assuming spherical shapes); that's 10 parameters:  $r_e$ ,  $v_e$ , complex  $n$  (assumed to be spectrally neutral), and an AOT for each mode. There is aerosol layer height, for which we need two more parameters, say,  $z_{\text{base}}$  and  $H_p$ ; that's 12 aerosol parameters in all if both the spectral dependence of the complex refractive index and possible deviation of the shape of particles from a perfect homogeneous sphere are neglected. But we still need to characterize the surface. If we opt for an mRPV model (see Appendix A) for the depolarizing part of the surface BRDM, we can assume that the two shape parameters ( $k$ ,  $b$ ) are spectrally invariant, but we need  $N$  copies of the overall scale parameter  $a$ . For the polarizing part of the BRDM, we need at least a scale parameter  $\xi$  and a parameter for the variance of the micro-facet slope probability density function (PDF). That's  $N + 4$  surface-related quantities,

$$m = 16 + N \quad (4.2)$$

parameters to determine in all. This is an impossible task if  $N_{\Omega} = 1$  and  $N_p = 0$  (e.g., MODerate resolution Imaging Spectroradiometer (MODIS) (King et al., 1992)), irrespective of  $N$ , so many additional constraints are required to infer aerosol and/or surface properties.

#### 4.2. JPL's operational MISR and experimental AirMSPi algorithms

Although theoretically possible with the Multiangle Imaging Spectroradiometer (MISR) (Martonchik et al., 2009), where  $N_{\Omega} = 9$ ,  $N = 4$  and  $N_p = 0$ , leading to  $M = 36$ , an optimized aerosol/surface retrieval is not attempted in MISR operational processing due to computational speed constraints (R.A. Kahn, pers. comm.). Indeed, not all of the  $M$  observations are expected to contribute independent pieces of information. The solution adopted in the operational MISR aerosol retrieval algorithm starts with the restriction of aerosol parameter space to 74 particle mixtures (a climatology populated with mono-, bi- and tri-modal PSDs), including two non-spherical dust-type particles, and two different heights for one of these (Kahn et al., 2010). All of these particles are used to generate a Look-Up Table (LUT); only the AOT is left to vary (discretely in the LUT, followed by an interpolation) (Martonchik et al., 1998a,b). Over land, regions of  $16 \times 16$  pixels ( $17.6 \times 17.6 \text{ km}^2$ ) are processed at the same time in a “multi-pixel” framework that assumes the same horizontally uniform aerosol within the region. Radiances for all pixels within the region are therefore based on the same path radiance (i.e., intensity for a black surface) but have an additional random element. A singular-value decomposition of the  $9 \times 9$  covariance matrix for the multi-spectral angular pattern of intensity leads to a much smaller number of significant surface eigenvectors, typically between 3 and 6 (Martonchik et al., 2002, 2009). These eigenvectors are summed and removed from the mean multi-spectral radiance pattern and the resulting estimates of path radiances are fitted using the look-up table (LUT) approach to find the best-fitting mixtures. About 70–75% of

MISR AOT retrievals fall within 0.05 or 20% of the AOT from the paired validation data from AERONET, with some sensitivity to particle type, i.e., categorical classifications into spherical nonabsorbing, spherical absorbing, and nonspherical (Kahn et al., 2010).

One drawback of the LUT-based approach is that retrieval biases may be incurred if the ambient aerosol is not captured in the LUT (Diner et al., 2011). For this reason, JPL is exploring an aerosol retrieval algorithm based on the Levenberg–Marquardt inversion scheme with the option of adding one or more smoothness constraints akin to Dubovnik et al. (2011) in the spectral or spatial (pixel) domains. It is sufficiently general that polarization data (e.g., from AirMSPi) has been readily incorporated. Starting with an initial guess  $\mathbf{x}_0$  for the state vector, the optimized solution is approached through following iterations in the simplest case (no additional smoothness constraints):

$$\left( \mathbf{J}_k^T \mathbf{W} \mathbf{J}_k + \Lambda_k \text{diag} \left( \mathbf{J}_k^T \mathbf{W} \mathbf{J}_k \right) \right) \Delta \mathbf{x}_k = \mathbf{J}_k^T \mathbf{W} (\mathbf{y} - \mathbf{F}(\mathbf{x})), \quad (4.3)$$

where  $\mathbf{J}_k$  is the Jacobian matrix evaluated from the iterative solution  $\mathbf{x}_k$  and the weighting matrix  $\mathbf{W}$  is diagonal with  $W_{ii} = 1/\text{Var}(\varepsilon_i)$  where  $\text{Var}(\varepsilon_i)$  is the variance of the instrument error on the  $i^{\text{th}}$   $I$  or  $Q$  measurements. The damping factor  $\Lambda_k$  is chosen and adjusted in a multiplicative way until a solution  $\mathbf{x}_{k+1} = \mathbf{x}_k + \Delta \mathbf{x}_k$  produces a significantly better fit to the measured data  $\mathbf{y}$ ; in other words, the following chi-squared error function is reduced:

$$\chi^2(\mathbf{x}_{k+1}) = \frac{1}{2} (\mathbf{F}(\mathbf{x}_{k+1}) - \mathbf{y})^T \mathbf{W} (\mathbf{F}(\mathbf{x}_{k+1}) - \mathbf{y}), \quad (4.4)$$

where  $\mathbf{F}(\mathbf{x}_{k+1})$  contains the fits for the reflectance and polarization data by the solution  $\mathbf{x}_{k+1}$  during the iteration. In the current version, and the iteration stops when the weighted average fitting error  $2 \chi^2(\mathbf{x}_{k+1})/M$  drops below a specified threshold.

The forward model is the vector MarCh code developed at JPL (Xu et al., 2011a,b, 2012). Currently it assumes a bimodal lognormal distribution of aerosols and contains 3 types of surface, (1): depolarizing parametric surface described by the modified RPV (mRPV) model, with two spectrally invariant parameters ( $k, b$ ) and one overall multiplier ( $a_s$ ) per wavelength (cf. Appendix A) (2): polarizing parametric water surface described by the Cox–Munk model, with two parameters for the longitudinal and latitudinal surface wind speeds and (3): mix of (1) and a polarizing microfacet model as in (2) but with more options for the slope distribution (cf. Appendix A”).

#### 4.3. The LOA/OP POLDER algorithm

The POLDER instrument has  $N_{\Omega} \approx 9$  to 16 depending on where the pixel is on the focal-plane array,  $N = 7$  (not counting the “A-band” channels) and  $N_p = 3$ , leading to  $M \approx 117$  to 208 observations. With  $N_{\Omega} \approx 200$ ,  $N = 8$  and  $N_p = N$ , leading to  $M \approx 4800$  observations, the APS (aboard the Glory satellite that unfortunately failed to reach orbit in 2011) would have extended the spectral range into the SWIR, thus providing additional constraints on the surface boundary condition.

The “OP” retrieval algorithm used for operational processing of POLDER data developed at the Laboratoire d'Optique Atmosphérique (LOA) is based on a traditional LUT approach. The algorithm for retrieval over the ocean is described by Deuzé et al. (1999) and Herman et al. (2005). The ocean reflectance is modeled with the Cox and Munk (1954) equations assuming a wind speed of 5 m/s for capturing multiple interactions between the surface and the atmosphere. The actual wind speed provided by the European Center for Medium-term Weather Forecasting (ECMWF) weather forecast model is used in the glint mask and for computing the foam reflectance according to the model proposed by Koepke (1984); the underwater contribution is taken equal to 0.001 and 0.000 at 670 and 865 nm respectively. The algorithm

**Table 3.3**  
1D vRT models used in Fig. 3.5.

1D vRT model	Institution	Solution method	Reference
MC	JPL	Monte Carlo	Davis et al. (in preparation)
MarCh	JPL	Markov chain formalism, accelerated with adding	Xu et al. (2011a,b)
SCIATRAN	University of Bremen	Discrete ordinates	Rozañov et al. (2014)

uses the total and polarized radiances at 670 and 865 nm and assumes that the size distribution follows a combination of two lognormal aerosol size distributions, one in the fine or “accumulation” mode and one in the coarse mode ( $r_e$  typically larger than 1.0  $\mu\text{m}$ ). Non-absorbing particles are considered in both modes. The LUT contains 33 aerosol models for the fine mode and 9 models for the coarse mode. The algorithm selects the combination of a fine and coarse mode that provides the best fit to the measurements. The total radiance modeled from the LUT, is approximated by a weighted sum of the tabulated radiance for the fine and coarse mode, respectively (Wang and Gordon, 1994). In the coarse mode, spherical or non-spherical particles are considered.

Over land surfaces, the PARASOL aerosol retrieval is based on polarized measurements at 670 and 865 nm (Herman et al., 1997; Deuzé et al., 2001). Contrary to the total radiances, polarized light reflectance of surfaces is small and fairly neutral spectrally (Nadal and Bréon, 1999; Maignan et al., 2009). The models used in the land algorithm are considering aerosols within the accumulation mode only. In other words, the contribution of the coarse mode is neglected, and it is assumed that mainly fine aerosols contribute to the measured polarized radiance. The refractive index is taken equal to 1.47–0.01i, which corresponds to a mean value for aerosols resulting from biomass burning or pollution events (Dubovik et al., 2002). The surface contribution depends on the surface type (bare soils or vegetated areas), and is estimated from a relationship using empirical coefficients adjusted for the different classes of land surfaces according to the main IGBP (International Geosphere–Biosphere Program) biotypes and the Normalized Difference Vegetation Index (NDVI).

An algorithm similar to that of POLDER was developed by Sano (2004). In this algorithm the fine mode fraction and AOT are found using polarized reflectance measurements for a priori assumed parameters of the fine and coarse modes. It is planned to extend the algorithm using double-view S-GLI observations for the polarized channels.

Cheng et al. (2012, 2013) have developed a new aerosol retrieval algorithm using multi-angular total and polarized measurements based on the LUTs of simulated satellite signals pre-computed for some limited selected aerosol scenarios and underlying surfaces. The algorithm was applied to POLDER data.

4.4. The LOA/GRASP POLDER algorithm

The GRASP algorithm for POLDER-3/PARASOL aerosol retrievals is described by Dubovik et al. (2011, 2014). The algorithm uses measurements of Stokes parameters  $I$ ,  $Q$ , and  $U$  at 6 POLDER-3 wavelengths between 440 and 1019 nm (the  $\text{O}_2$  A-band channels are omitted). The basic algorithm concept is based on the AERONET algorithm to invert diffuse sky measurements (Dubovik et al., 2000). No a priori parameterized shape of the size distribution is assumed. Instead, a discretized size distribution for 16 size bins between 0.07 and 10  $\mu\text{m}$  is retrieved. The refractive index is assumed independent of aerosol size (i.e., no difference between fine and coarse aerosols), but it may depend on wavelength. Particles represent a mixture of spheres and spheroids (Dubovik et al., 2006), where the fraction of spheres is a fitted parameter. In addition to size distribution and refractive index, the central height of a Gaussian shaped height distribution is also retrieved.

The development of GRASP, as described by Dubovik et al. (2011), has mainly been focused on aerosol retrievals over land. GRASP has a large variety of approaches for surface reflection description based on the semi-empirical and physical models of BRDM for ocean and land surfaces. In the semi-empirical models, BRDM is presented as the sum of the semi-empirical BRDF models, such as the Rahmann–Pinty–Verstraete (RPV) and Ross–Li models, and the reflection matrix based on Fresnel reflection from surface models of Maignan et al. (2009) and Litvinov et al. (2011a,b). For these models, 4 parameters are retrieved (one scaling and two directional parameters of BRDF and one scaling parameter for Fresnel-based reflection matrix). In principle, all these parameters are allowed to change with wavelength but for the directional parameters and the scaling parameter for Fresnel-based reflection matrix the wavelength dependence is highly constrained. Physical BRDM model for land surfaces is described by Litvinov et al. (2012). This model works with 4 parameters related to physical properties of surfaces (albedo of a surface element, surface roughness, fraction of surface providing Fresnel reflection). One parameter out of four (surface albedo) is spectrally dependent while three others are common parameters for all elements of surface BRDM.

GRASP inversion method is statistically optimized minimization as described by Dubovik and King (2000) and Dubovik (2004). Here, the

**Table 4.1**  
Characteristics of selected aerosol retrieval algorithms for multi-angle photo-polarimetric measurements.  $N$  is the columnar aerosol concentration  $R_{pol}$  is the polarized reflectance (see Eq. (3.24)).

Institution	GISS	LOA (GRASP)	LOA (OP)	SRON
Reference	Waquet et al. (2009a), Knobelspiesse et al. (2011)	Dubovik et al. (2011)	Deuzé et al. (1999, 2001), Herman et al. (1997, 2005)	Hasekamp et al. (2011)
Instrument	RSP	POLDER	POLDER	POLDER
Spectral range	410–2300 nm	440–1020 nm	670–865 nm	490–670 nm
Measurement	$R_{pol}$	$R, Q/I, U/I$	$R, R_{pol}(\text{ocean}), R_{pol}(\text{land})$	$R, Q/I, U/I$
Surface	Land	Land	Land & ocean	Ocean
Aerosol parameters	$r_e, v_e, n_r, n_i, N$ for bi-modal size distribution	size distribution (16 bins), $n_r, n_i$ , fraction non-spherical	AOT & aerosol model	$r_e, v_e, n_r, n_i, N$ for bi-modal size distribution
Surface parameters	Fresnel scaling (angle dependent)	RPV parameters, BPDF scaling	No	Wind speed (2 directions), $[\text{Chl}_a]$ , foam fraction
Online RT (if so, numerical method)	Yes (adding/doubling)	Yes (successive orders of scattering)	No	Yes (Gauss–Seidel iteration)
Inversion technique	Optimal estimation	Regularization with smoothness constraints	Least squares	Tikhonov regularization with prior
Iteration technique	Levenberg–Marquardt	Gauss–Newton	n/a	Reduced step Gauss–Newton
Multi-pixel	No	Yes	No	No

cost function to be minimized contains a term minimizing the difference between forward model and measurement and a side constraint imposing smoothness of the size distribution and spectral dependence of the refractive index and of directional surface parameters.

The GRASP algorithm is capable of doing conventional “single-pixel” retrievals but also has the capability to make “multi-pixel” retrievals, i.e., inverting measurements for a group of ground pixels simultaneously. In a contrast to MISR’s operational aerosol retrieval, GRASP’s multi-pixel approach does not assume the same aerosol properties within inverted group of the pixels. The retrieved parameters may change but allowed variability is restricted by a priori smoothness constraints. In addition, the group of pixels inverted in multi-pixel retrieval of GRASP includes multi-temporal observations. This allows for constraining retrieval by applying both smoothness constraints on the spatial variation of aerosol properties and also on the temporal variation of surface parameters. The application of these multi-pixel smoothness constraints is implemented in the frame of rigorous statistical optimization. (We emphasize here that this multi-pixel methodology operates statistically in the aerosol retrieval through the so-called “regularization” term of the cost function where the RT is modeled in 1D; this is not to be confused with the physics-based multi-pixel approach used by Langmore et al. (2013) where 3D RT is used deterministically in the cost function to be minimized.) Detailed mathematical derivations are provided in Dubovik et al. (2011). Examples of retrievals are shown in Figs. 4.1 and 4.2.

#### 4.5. The SRON/POLDER algorithm

The SRON-POLDER algorithm, as described by Hasekamp et al. (2011), utilizes measurements of intensity  $I$  and relative Stokes fractions  $Q/I$  and  $U/I$  at 490 nm and 670 nm. Hasekamp et al. (2011) focus on aerosol retrievals over the ocean. Here, the BRDM of the ocean is modeled taking into account underwater scattering, where the ocean optical properties are parameterized as function of the chlorophyll concentration (Chowdhary et al., 2006), Fresnel reflection on the rough ocean surface (Cox and Munk, 1954), and the contribution of whitecaps.

To define the state vector for the retrieval problem it is assumed that the aerosol size distribution can be described by bimodal lognormal functions for small and coarse modes, respectively. The aerosol parameters included in the state vector are for each mode the effective radius  $r_e$ , the effective variance  $v_e$  (see, e.g., Hansen and Travis, 1974), the aerosol loading, and the real and imaginary parts of the refractive index. In addition to these aerosol parameters the following ocean properties are included in the state vector: chlorophyll a concentration [Chl], wind speed  $v_x$  and  $v_y$  parallel and perpendicular to the solar plane (defined by the incoming solar beam and the zenith direction), and the fraction of the PARASOL pixel footprint that is covered by whitecaps.

To retrieve the state vector from the PARASOL measurements, the inversion algorithm implemented by Hasekamp and Landgraf (2005) is based on Phillips–Tikhonov regularization (Phillips, 1962; Tikhonov, 1963). The Phillips–Tikhonov method finds the retrieved state vector  $\mathbf{x}$  by minimizing a cost function that is the sum of the least squares cost function and a constraint term containing the weighted difference between the state vector and an a priori state vector. That 2nd term in the cost function is weighted by a regularization parameter. An appropriate value for the regularization parameter is found using the so called “L-curve” technique (Hansen and O’Leary, 1993). Since the retrieval problem is nonlinear it is solved iteratively using a Gauss–Newton iteration scheme with a progressively reduced step size (i.e., the step size is decreased gradually during the course of the iteration). The validation of retrievals over ocean is demonstrated in Figs. 4.3 and 4.4.

An alternative version of the SRON aerosol retrieval scheme for ground-based aerosol retrievals is currently being explored, where a neural network (NN) algorithm is used to generate a first guess as a replacement for the LUT (Di Noia et al., 2015). The main advantage of this solution is that it makes it easier to improve the quality of the first guess. In fact, improving the quality of the LUT retrievals themselves

would require a considerable increase in the number of LUT entries, with negative effects on retrieval speed and memory requirements.

In very general terms, NN retrievals are performed by fitting the parameters of a nonlinear function that maps the measurement vector onto the state vector to be retrieved, using a large number of input–output coincidences stored in a training set. While the training of a NN can be a time consuming process, a trained NN can be used to deliver retrievals in fractions of seconds. NNs have already proven successful in solving a number of remote sensing tasks, such as temperature and humidity retrievals (Aires et al., 2002; Blackwell, 2005), ozone profile retrievals (Del Frate et al., 2002; Müller et al., 2003), precipitation and cloud measurements (Tapiador et al., 2004; Loyola, 2006), and have been investigated for aerosol retrievals from MODIS (Vucetic et al., 2008; Ristovski et al., 2012). In a similar way, a suitably trained NN for the retrieval of the aerosol properties from spectropolarimetric data can be expected to provide fast and accurate retrievals. The idea behind the use of these retrievals as first guess in an iterative algorithm is that they can be then further improved through an inversion based on full radiative transfer calculations.

The training set for the NN used in the SRON retrieval algorithm has been generated by performing circa half million radiative transfer simulations. A set of 8 aerosol parameters (effective radius, complex refractive index and optical thickness at 550 nm for the fine and the coarse mode of a log-normal size distribution) have been randomly varied within a physically meaningful range. Ground-based measurements of reflectance and degree of polarization at 3 wavelengths (490, 675 and 870 nm) and six VZAs and the azimuthal angle of 180° have been simulated using a polarimetric radiative transfer model. The simulated measurements and the corresponding combinations of aerosol parameters have been used as input and output variables for the neural model respectively. The SZA and the surface pressure have been used as additional input variables for the NN inversion scheme. In the case of retrievals using simulated data, the use of the aforementioned NN as a first guess in the SRON retrieval scheme has resulted in an increased number of successful retrievals (retrievals that achieved a goodness-of-fit parameter smaller than 2) of almost a factor 2 compared to the original algorithm using a LUT as first guess. Preliminary applications to real ground-based observations from the SPEX (Spectropolarimeter for Planetary EXploration) instrument also show an increase in the number of successful retrievals, and a considerable improvement in the estimate of the imaginary part of the aerosol refractive index (Di Noia, 2015; van Harten et al., 2014). Airborne and space-based versions of SPEX are under development.

#### 4.6. The retrieval algorithm for the Directional Polarimetric Camera (DPC)

The main scientific objective of DPC lies in environmental monitoring of urban environments making use of the high-resolution capability. An algorithm for retrieving simultaneously aerosol optical properties from multi-angular polarized data was developed (Cheng et al., 2011), which simultaneously provides the aerosol optical thickness and the Ångström exponent (AE).

The retrieval algorithm is based on a LUT, which is a function of aerosol optical thickness, aerosol optical model, surface polarized reflectance model, and viewing and illumination geometries. To solve most of the ambiguity in retrieving aerosol optical properties using the DPC measurements alone, ground-based measurements are used to constrain the inversion in terms of the key characteristics of a local aerosol model, including spectral complex refractive index, size distribution, and vertical distribution of aerosol optical parameters. The Nadal–Bréon model for the BPDF was used to simulate the multi-angular polarized radiance over vegetation surfaces, and was adjusted using DPC polarized measurements at low altitude (Xie et al., 2011).

In the retrieval program, the sun-sensor geometric parameters, including the solar zenith angle, the sensor-view zenith angle, and the relative azimuth angle, were first prescribed for each pixel of DPC measurements. Because the DPC can deserve a single spot with 6 viewing

zenith angles, observations at 6 scattering angles for each pixel in the retrieval algorithm. Thus, using spectral bands, each pixel are used will have 12 pieces of observations for the determination of AOT and AE. The retrieval algorithm employs the least mean squares fitting method in the form of a series of numerical iteration procedures to search for the computed polarized reflectance that best matches the polarized reflectance observed by the DPC.

4.7. The GISS/RSP algorithm

The GISS/RSP retrieval algorithm is described by Waquet et al. (2009a) and Knobelspiesse et al. (2011) for aerosol retrievals over land. RSP is an airborne prototype of the Aerosol Polarimetric Sensor (APS) on the Glory satellite that unfortunately failed at launch in 2011. The main idea behind the RSP retrieval algorithm is to use only measurements of the polarized reflectances  $R_p$ , as in these signals the influence of surface reflectance is small, spectrally flat, and relatively simple to model. The algorithm exploits the full spectral range of RSP between 410 and 2250 nm. As a first step the contribution of polarized surface, reflection is determined from the 2250 nm channel where the atmospheric contribution is assumed to be small. For the surface polarized reflectance, a scaling of the Fresnel polarized reflection function  $R_p^F$  for a refractive index  $n_s = 1.5-0 \times i$  is used:

$$R_p(\theta_0, \theta, \phi) = \zeta R_p^F(\gamma), \tag{4.5}$$

where  $\gamma(\theta_0, \theta, \phi)$  is the surface scattering angle (at the micro-facet scale, cf. Appendix A) and  $\zeta$  is the scaling coefficient. Since the different viewing directions of RSP are not perfectly co-located the scaling coefficients are determined for each viewing direction separately. The retrieved polarized surface reflectance at 2250 nm is used at the other wavelengths as input for the aerosol retrieval, because the surface polarized reflectance is assumed to be spectrally flat.

For the retrieval of aerosol properties a bi-modal aerosol model for spherical aerosols is assumed, of which the corresponding 10 aerosol parameters ( $r_e, v_e, n_r, n_i, N$  of both the fine and coarse

mode) are unknown parameters. Here, the real and imaginary parts of the refractive index are wavelength dependent but a correlation between different wavelengths is assumed. The aerosol parameters are retrieved from the RSP measured polarized reflectances using an Optimal Estimation approach combined with the Levenberg–Marquardt iterative method to account for the nonlinearity of the forward model. The a priori information on aerosol properties needed for Optimal Estimation is obtained from the climatology of Dubovik et al. (2002). The first guess aerosol properties to start the iterative procedure are obtained by performing a LUT-based retrieval for a number of standard aerosol models. At each iteration step, new scaling coefficients for the Fresnel surface model are determined taking into account the residual aerosol effect at 2250 nm. The developed technique is very powerful and currently is being updated for the application to other polarimetric observations (RSP, AirMSPi, 3MI) with main modifications with respect to the first guess determination (analytical radiative transfer approximations, NNs, atmospheric chemistry models, LUTs).

5. Passive determination of the aerosol profile from oxygen A-band spectroscopy

Yamamoto and Wark (1961) first proposed that O<sub>2</sub> A-band spectroscopy (759–770 nm) could be used to obtain cloud top height since, to a first approximation, the absorption spectrum is determined by the two-way transmission of the sunlight through the airmass above the cloud. It was eventually realized that, due to the significant photon path length cumulated inside the cloud, the cloud top pressure/height estimate would be biased low (Wu, 1985). However, for that very same reason, physical cloud thickness can be estimated from the A-band data as long as there is sufficient spectral resolution (O'Brien, and Mitchell, 1992; Heidinger and Stephens, 2000; Stephens and Heidinger, 2000) and/or angular sampling (Ferlay et al., 2010) to unravel the above-cloud and in-cloud paths. Both observational and theoretical research are ongoing, motivated by this novel way of passively profiling the cloudy atmosphere using scattering, similar to what the competing

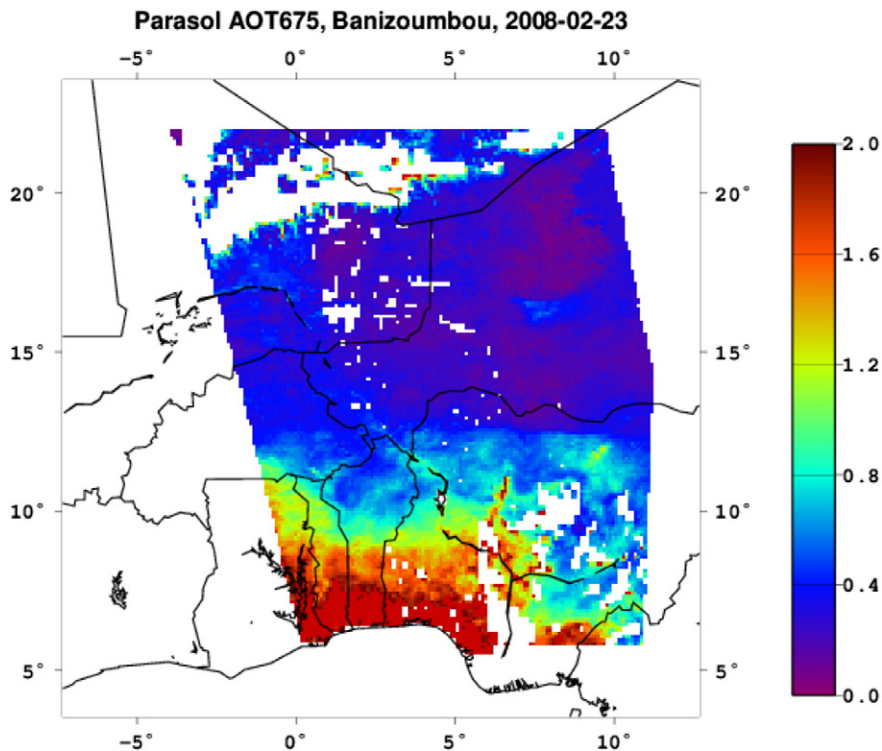


Fig. 4.1. The retrieval of AOT using POLDER-3 data with the GRASP algorithm.

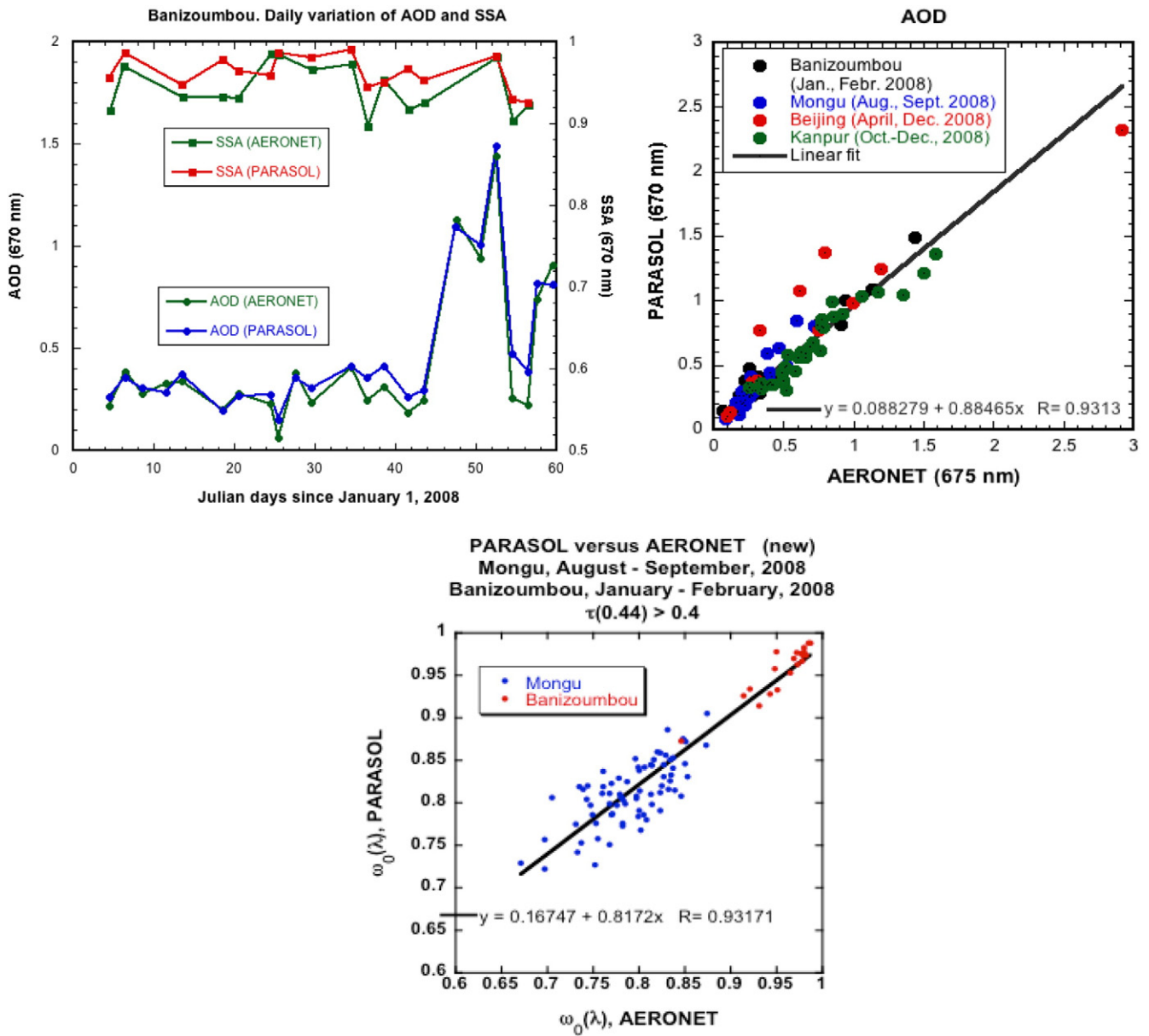


Fig. 4.2. Ground-based validation of retrieval of aerosol optical depth (AOD) and single scattering albedo (SSA) using POLDER-3 data with the GRASP algorithm.

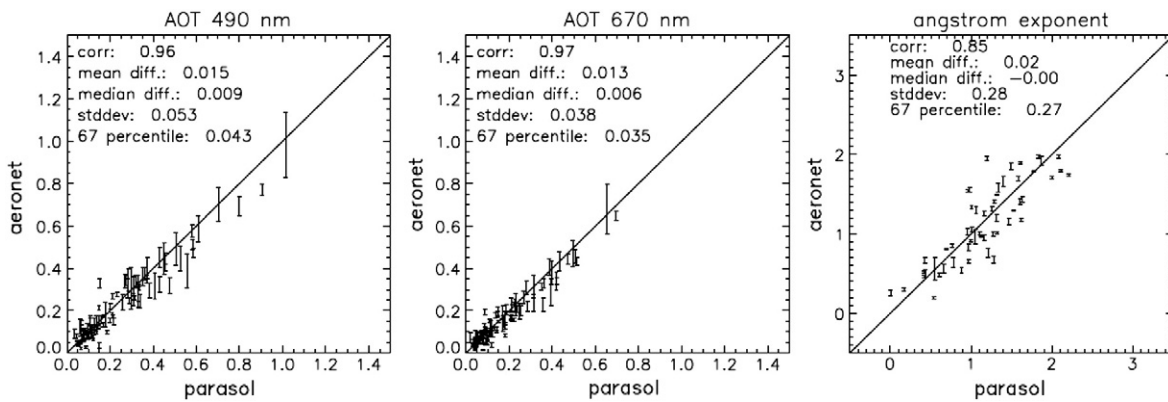
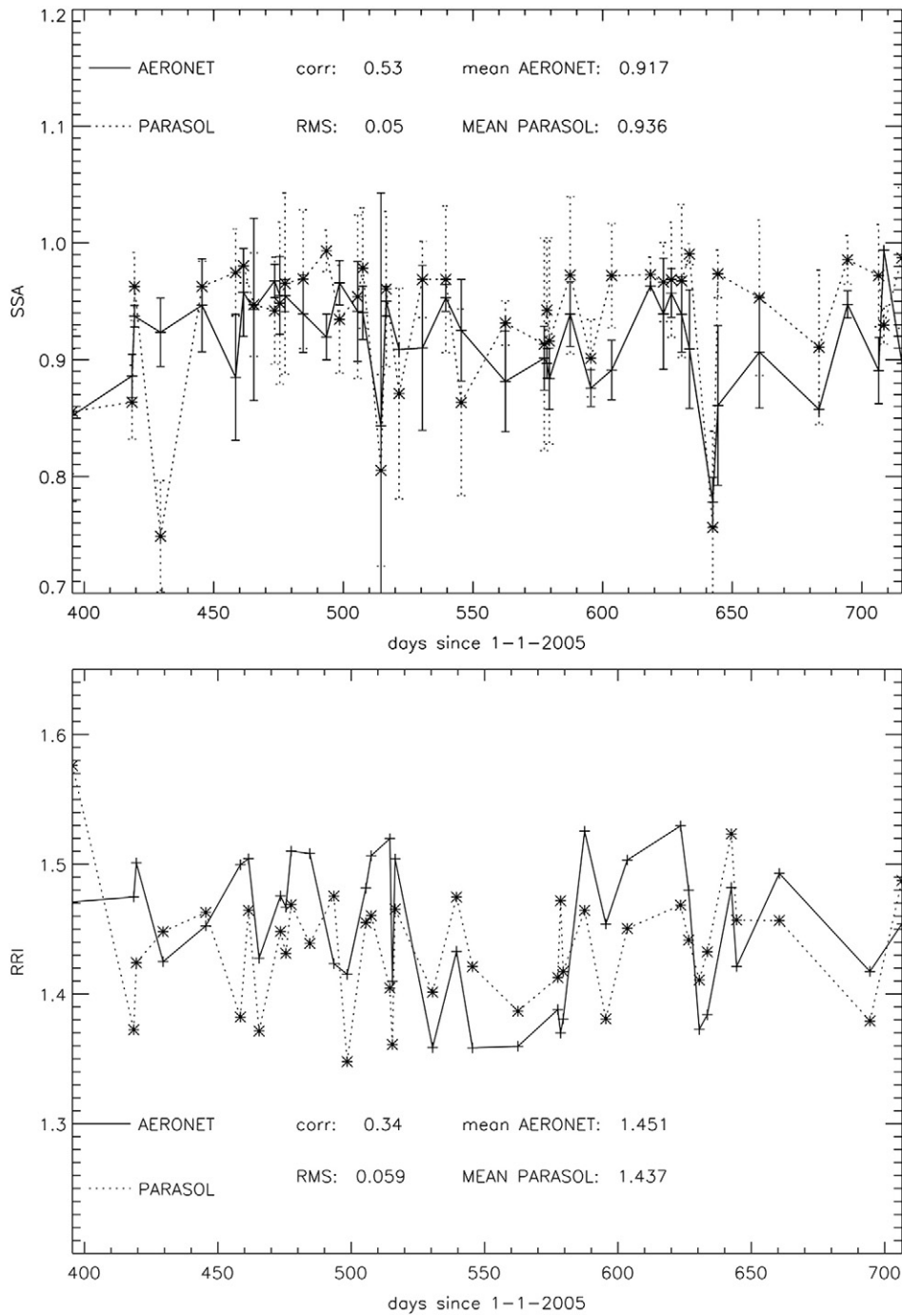


Fig. 4.3. PARASOL over ocean retrievals versus AERONET. (Left) AOT at 490 nm, (middle) AOT at 670 nm, and (right) Angstrom exponent. For PARASOL the median of the retrieval results within 40 km from the AERONET site are shown. For AERONET the median is shown over a 2-hour period. The error bars show the peak-to-peak variability of the AERONET values within 2 h. We consider comparisons for which at least three AERONET measurements are available in the 2-hour period, and three PARASOL retrievals with the 40 km radius. Adapted from Hasekamp et al. (2011).



**Fig. 4.4.** Time series of  $SSA_{670}$  (upper panel) and model real part of refractive index  $RRI_{670}$  (lower panel) retrieved from POLDER/PARASOL (volume-weighted radii of fine and coarse modes) near FORTH-Crete, compared to Level 1.5 AERONET retrievals that are coincident with the POLDER measurements to within  $\pm 0.5$  days (averaged).

active technologies (mm-wave radar and lidar) do, but with far simpler instrumentation offering the possibility of imaging cloud height, and maybe thickness as well. Can the same feat be done for aerosols?

In the absence of clouds, remote sensing of the  $O_2$  A-band offers a priori a convenient means to estimate surface pressure (Barton and Scott, 1986), especially over vast oceanic areas with too few weather stations, let alone radio-sondes, hence severely reduced accuracy in numerical weather prediction. It was soon realized that one of the major sources in uncertainty in surface pressure estimates obtained from such passive remote sensing techniques is aerosol scattering in the atmosphere (Mitchell, 1987; Mitchell and O'Brien, 1987). Aerosols induce error in the following ways: (1) by direct scattering of sunlight into the

observing beam, thus shortening the effective absorption path length; (2) by illumination of the satellite footprint with diffuse (single or multiple) scattered light, thereby lengthening the absorption path; and (3) by the scattering into the observing beam of light reflected from arbitrary points on the surface, thereby lengthening the absorption path. The effect of an aerosol layer on the apparent pressure depends on its thickness and altitude.

Timofeyev et al. (1995) pioneered the application of information content analysis to determine the potential of  $O_2$  A-band measurements to retrieve vertical profiles of aerosol optical properties. van Diedenhoven et al. (2005) studied the effects of aerosols on the retrieval of surface pressure using simulated SCIAMACHY measurements for

atmospheres with different aerosol loads. They found that, depending on the surface albedo, the surface pressure could be under- or over-estimated by neglecting scattering due to aerosols.

Recently, the effects of polarization have begun to be considered. Stam et al. (1999) illustrated the use of linear polarization measurements in the O<sub>2</sub> A-band to obtain aerosol vertical profile information. Knibbe et al. (2000) recognized that the linear polarization of sunlight reflected by cloudy areas on Earth is sensitive to the cloud top pressure as a result of molecular scattering above the clouds and showed that cloud top pressures could be derived using photo-polarimetry. Stam et al. (2000) demonstrated that, for an instrument with a given polarization sensitivity, the best way to decrease errors in the radiances (which in turn decrease errors in retrieved atmospheric parameters such as cloud top height) is to simultaneously measure the radiance and state of polarization of the observed light. Zeng et al. (2008) showed that polarization data could be used together with radiance data to constrain the vertical distribution of aerosol composition.

Clearly, aerosols are a significant factor in the determination of surface and cloud top pressure. Gabella et al. (1999) showed that aerosol profile variations could be retrieved using radiance measurements in the O<sub>2</sub> A-band. The fundamental physical reason for using the O<sub>2</sub> A-band is the large dynamic range of absorption as a function of wavelength. Where there is high absorption, the reflected signal that reaches the satellite comes from the upper part of the atmosphere, whereas at regions of lower absorption scattering from lower layers becomes increasingly more pronounced.

However, this technique is not very effective when there are multiple aerosol layers in the atmosphere. Jiang et al. (2003) and Boesche et al. (2008) showed that the degree of linear polarization inside the O<sub>2</sub> A-band offers an additional constraint on the vertical distribution of aerosol and cirrus clouds. In the line cores, the strong absorption shields the lower layers of the atmosphere from incident sunlight. Therefore most of the light has been scattered at high altitudes, whereas in the continuum no such shielding occurs. Thus, the change in polarization between the continuum and the line cores reflects the different polarizing properties of the aerosols in the lower and upper parts of the atmosphere. In other words, polarization provides information about the location as well as the type of aerosol. The latter is not possible with radiance-only measurements. Further, even the former is hard to attain without high spectral resolution.

With the launch of the JAXA Greenhouse Gases Observing Satellite (GOSAT) (Kuze et al., 2009), and the NASA Orbiting Carbon Observatory-2 (OCO-2) (Crisp et al., 2004), we now have high spectral resolution polarimetric O<sub>2</sub> A-band measurements from space. The time is therefore ripe to realize the potential of the O<sub>2</sub> A-band to perform aerosol profile retrievals. Further, combining O<sub>2</sub> A-band measurements with multi-wavelength, multi-angle polarimetric measurements such as that from POLDER (cf. Section 2.1.3) has tremendous potential to revolutionize aerosol remote sensing since the former constrains the aerosol vertical distribution while the latter is sensitive to the microphysical parameters.

## 6. Summary, conclusions and outlook

Aerosol remote sensing using spaceborne instrumentation remains a challenge. This is because particles suspended in atmosphere can have vastly different origins and histories that influence their chemical composition, shape, and size distributions that, ultimately, determine their observable optical properties.

NASA's CALIPSO mission (Winker et al., 2010) has demonstrated that a space-based LIDAR (Light Detection And Ranging) such as CALIOP (Cloud-Aerosol Lidar with Orthogonal Polarization) is a powerful active technique for probing the atmospheric aerosol, especially with the possibility to measure depolarization in the returned light pulse. However, CALIOP's backscattering lidar signal does not disambiguate

between aerosol extinction and the phase function (at 180°). ESA's EarthCARE mission will have that capability thanks to the adopted HSRL (high spectral resolution lidar) technology (Hélière et al., 2012). Notwithstanding, spaceborne lidar captures only a rapid sequence of vertical atmospheric profiles, a 2D transect or “curtain” along the sub-satellite ground track. Many applications call for more comprehensive spatial and temporal sampling offered only by passive imaging sensors and, better still, for improved aerosol characterization, combined active/passive instrumentation.

In the present survey, we have described the state-of-the-art in multi-spectral/multi-angle/multi-polarization sensor development as well as in the corresponding physics-based multi-dimensional forward signal modeling using “vector” radiative transfer. We also discussed the current approaches used to solve the associated inverse problem. Since the aerosol-laden atmosphere can be anywhere between from highly to moderately transparent, we have confronted the complication in aerosol remote sensing caused by the underlying surface, with special attention to its spectral, bidirectional and polarization reflection characteristics. Finally, we have reported on on-going research into the exploitation of passive oxygen A-band spectroscopy to infer at least a coarse vertical profile of the aerosol.

However, by adopting upfront the “1D” framework for polarized radiative transfer, we have completely ignored “pixel adjacency” effects, i.e., the influence of the horizontal variability of the underlying surface properties as well as of atmospheric properties, particularly, clouds and in opaque aerosol plumes that can occur near potent sources of particles (fires, industrial facilities, and so on). Either ways, “3D” radiative transfer models are required to quantify these effects. Possible biases due to spatial fluctuations of surface albedo have been extensively investigated (see brief discussion and many references in Section 3.4). Similarly, aerosol remote sensing in the vicinity of clouds remains an important and challenging problem. This can be when the clouds are spatially resolved, the “cloud adjacency” problem (Zhang et al., 2005; Wen et al., 2007; Marshak et al., 2008; Várnai and Marshak, 2009, 2011; Chand et al., 2012), or when the clouds and aerosols are mixed inside a wide footprint pixel, the “cloud contamination” problem (Kaufman et al., 2005; Zhang et al., 2005; Hasekamp, 2010; Knobelspiesse et al., 2011; Davis et al., 2013). These 3D surface or atmospheric violations of the assumed 1D forward signal modeling will thus remain a subject of vigorous research that will lead in time to operational models with improved fidelity. In the meantime, satellite data processing will go through rigorous cloud (or dense aerosol plume) screening procedures to ensure the quality of 1D-based retrievals and, whenever possible, a quantified uncertainty due to forward model error will be added to the overall retrieval error budget.

Finally, there is a growing interest in targeting tropospheric aerosols above extended cloud decks with purely passive remote sensing. This can be done by exploiting polarization (Waquet et al., 2009b; Hasekamp, 2010) or the strong absorption present in aerosols, e.g., smoke and dust, that are most likely to be lofted above the clouds and transported over long distances (Torres et al., 2012; Jethva et al., 2013). Another problem is to detect and characterize aerosols below an elevated cirrus cloud layer, in which case multi-angle observations are key (Pierce et al., 2010). These situations can be addressed within the framework of 1D radiative transfer, polarized if necessary, with added sophistication in the stratified structure of the atmosphere.

An important conclusion is that to increase the information content one needs to use multi-angular polarimetric measurements in several carefully selected wavebands. Spectral intensity-only measurements at a single view angle may provide reliable measurements if correct a priori information is used such as the surface spectral albedo, aerosol type, and phase function (Kokhanovsky and de Leeuw, 2009; Kokhanovsky et al., 2010b). However, generally, multi-angular (and also polarimetric) measurements are needed to better constrain the inverse problem solution (King et al., 1999; Lebsock et al., 2007). New spaceborne optical devices such as multiangle imaging

spectropolarimeters (see, e.g., Marbach et al., 2013) will provide a wealth of information, which can be used for the further advance of our knowledge on global atmospheric aerosol properties (Kinne et al., 2013).

### List of abbreviations and acronyms

1D	one-dimensional
3D	three-dimensional
3MI	Multi-viewing Multi-channel Multi-polarization Imager (EUMETSAT mission)
ACE	Aerosol–Cloud–Environment (Tier 2 NASA Decadal Survey mission)
ADEOS	ADvanced Earth Observing Satellite (JAXA satellite series)
AERONET	AERosol RObotic NETwork
AE	Ångstrom exponent
AOLP	angle of linear polarization
AOT	aerosol optical thickness
AirMSPI	Airborne MSPI
APS	Aerosol Polarimetry Sensor
BC	boundary condition
BRDF	bidirectional reflectance distribution <i>function</i>
BRDM	bidirectional reflectance distribution <i>matrix</i>
BRF	bidirectional reflectance factor
CALIOp	Cloud–Aerosol Lidar with Orthogonal Polarization (main CALIPSO instrument)
CALIPSO	Cloud–Aerosol Lidar and Infrared Pathfinder Satellite Observations (satellite)
DOLP	degree of linear polarization
DPC	Directional Polarimetric Camera
ECMWF	European Center for Medium-term Weather Forecasting
EM	electro-magnetic (e.g., waves)
EUMETSAT	European Meteorological Satellite Organization
FOV	field of view
GRASP	Generalized Retrieval of Aerosol & Surface Properties
HARP	HyperAngular Rainbow Polarimeter
HySPAR	HyperSpectral Polarimeter for Aerosol Retrievals
GCOM	Global Change Observation Mission (JAXA satellite series)
IFOV	instantaneous FOV
IGBP	International Geosphere–Biosphere Program
ISSI	International Space Science Institute (Bern, Switzerland)
JAXA	Japanese space agency
JPL	Jet Propulsion Laboratory (NASA Center)
LOA	Laboratoire d’Optique Atmosphérique (CNRS research unit at Université Lille 1)
LUT	Look-Up Table
MarCh	a (largely linearized) Markov Chain 1D vRT model
MC	Monte Carlo (numerical integration method)
MISR	Multiangle Imaging Spectroradiometer
MODIS	MODerate resolution Imaging Spectroradiometer
mRPV	modified RPV (parametric BRDF model)
MSPI	Multiangle SpectroPolarimetric Imager
NASA	National Aeronautics and Space Agency
NDVI	Normalized Difference Vegetation Index
NN	neural network
NSV	normalized Stokes vector
PARASOL	Polarization and Anisotropy of Reflectances for Atmospheric Science coupled with Observations from a Lidar
PACS	Passive Aerosol & Clouds Suite Polarimeter
PEM	photo-elastic modulator
PODEX	Polarization Definition EXperiment
POLDER	Polarization and Directionality of Earth Reflectance
PSD	particle size distribution
RPI	Rainbow Polarimetric Imager
RPV	Rahmann–Pinty–Verstraete (parametric BRDF model)
RSP	Research Scanning Polarimeter

RT	radiative transfer
SCIAMACHY	Scanning Imaging Absorption Spectrometer for Atmospheric CHartography
SCIATRAN	1D RT code (designed originally to support the SCIAMACHY mission)
S-GLI	Second generation GLobal Imager
SPEX	Spectropolarimeter for Planetary Exploration
SRON	Netherlands Institute for Space Research
SSA	single scattering albedo
SWIR	shortwave infrared
SZA	solar zenith angle
TOA	top-of-atmosphere
V&V	Verification and Validation
vRT	vector (i.e., polarized) RT
vRTE	vector RT equation
VNIR	visible/near infrared (spectral range)
VZA	Viewing Zenith Angle

### Acknowledgments

This work was supported financially by the International Space Science Institute (ISSI) in Bern (Switzerland), by EUMETSAT, by JAXA's Global Change Observation Mission – Climate 1 (GCOM-C1) project (JX-PSPC-40059), by JSPS KAKENHI (25340019), and by NASA, ESA, DFG, SRON, CNRS, as well as Bremen University and Lille University. The authors extend special thanks to Vladimir Budak, Dave Diner, Mike Garay, Ya. Ilyushin, Ralph Kahn, Olga Kalashnikova, Rob Levy, Anton Lopatin, John Martonchik, Michael Mishchenko, Lorraine Remer, Felix Seidel, Robert Spurr, Knut Stamnes, Didier Tanré, and Elenora Zege for the many useful discussions related to the topic of this paper, at ISSI and elsewhere. We thank K. Tanaka and H. Murakami of the JAXA (Japan) for providing us with detailed information about S-GLI. Part of this research was performed at the Jet Propulsion Laboratory, California Institute of Technology, under contract with the National Aeronautics and Space Administration.

### Appendix A. Reflectivity of underlying surfaces

#### A.1. Definitions

The intrinsic reflectance properties of underlying surfaces are described by a bidirectional reflection distribution matrix (BRDM)  $\rho = \mathfrak{R} / \pi$  that was introduced in Eq. (3.21b) to describe the lower boundary condition on the 1D vRT problem germane to aerosol remote sensing from space. It provides a relation between the Stokes parameters of reflected (i.e., surface-scattered) and incident radiation fields (see, e.g., Mishchenko and Travis, 1997):

$$I = \mathfrak{R} F_0 \mu_0 / \pi. \quad (\text{A.1})$$

Here,  $\mathbf{I} = [I, Q, U, V]^T$  is the formal Stokes column vector describing the radiance and polarization state of surface-scattered radiation (superscript T stands for “transposed”), and  $\mathbf{F}_0 = [F_0, F_q, F_u, F_v]^T$  is the incoming Stokes vector, describing total and polarized incident irradiances perpendicular to the incoming direction  $(\vartheta_0, \varphi_0)$ . To describe the quantities that determine  $\mathfrak{R}$ , we will need: the wavelength  $\lambda$  of the incident and scattered radiation;  $\phi$  to denote the azimuth angle difference  $\varphi_v - \varphi_0$ , with  $\varphi_0$  and  $\varphi_v$  being the solar and viewing azimuth angles, respectively;  $\vartheta_0$  and  $\vartheta_v$  for the solar and viewing zenith angles, respectively ( $\vartheta_0 = \pi - \vartheta_{inc}$ ,  $\vartheta_{inc}$  being the incident zenith angle in the interval  $(\pi/2, \pi)$ ); and  $\mu_0 = \cos \vartheta_0$ .

When the incident radiation is unpolarized, the element  $\mathfrak{R}_{11}$  of the matrix  $\mathfrak{R}$  is the surface total reflectance (denoted hereafter as  $R_T$ ), and

the elements  $\mathfrak{R}_{21}$  and  $\mathfrak{R}_{31}$  define surface linearly polarized reflectances (denoted hereafter as  $R_p$ ):

$$I = R_I F_0 \mu_0 / \pi, \quad (\text{A.2})$$

$$Q = \mathfrak{R}_{21} F_0 \mu_0 / \pi, \quad (\text{A.3})$$

$$U = \mathfrak{R}_{31} F_0 \mu_0 / \pi, \quad (\text{A.4})$$

$$R_p = \sqrt{\mathfrak{R}_{21}^2 + \mathfrak{R}_{31}^2}. \quad (\text{A.5})$$

Here,  $F_0$  is the incident radiant energy flux per unit area perpendicular to the incident beam (implicitly, in a narrow spectral band around  $\lambda$ ). This definition of total and polarized reflectances has been used by different authors (Roujean et al., 1992; Nadal and Bréon, 1999; Maignan et al., 2009). The definition of the surface total reflectance used here is equivalent to the definition of the bidirectional reflectance factor (BRF), see, e.g., Schaepman-Strub et al. (2006). Implicitly, we suppose here that directional surface reflection properties vary weakly within the instrument's IFOV, thus the conical reflectance quantities are equivalent to the directional ones.

It must be noted that vector radiative transfer calculations for a coupled atmosphere–surface system require all elements of the BRDM for surfaces rather than only the surface total and polarized reflectances ( $R_I$  and  $R_p$ ). However, it is usually assumed that surface reflections are strongly depolarizing over a wide range of scattering angles. This is the case, for example, for complex media causing considerable diffuse

scattering (Woolley, 1971; Savenkov et al., 2003; Tishkovets et al., 2004; Muñoz et al., 2007). Under these conditions the elements (1,1), (2,1), and (3,1) of the BRDM for surfaces give the main contribution to the top-of-atmosphere (TOA) total and polarized reflectances. Let us note that the effect of the elements (2,2) and (3,3) of BRDM on top-of-atmosphere polarized reflectance may be noticeable in high-accuracy polarization measurements. The corresponding effects are subjects for future investigations.

## A.2. Illustration

We show the elements of the BRDM for soil and sand in Fig. A.1. The soil sample is from the Goloseevo Forest near Kiev (Ukraine, April 2014) and sand is the river sand with average dimension of grain of 50  $\mu\text{m}$ . For these measurements the complete Mueller–polarimeter described by Savenkov (2002) was used. We have used backward scattering geometry in the principle plane with fixed incident angle  $10^\circ$  relative to normal to the surface of samples and observation angles in the range  $5^\circ$ – $80^\circ$  resulting in scattering angles of  $90^\circ$  to  $165^\circ$ . The wavelength of the incident light was 630 nm. The incident laser beam was widened to 10-mm diameter to exclude the influence of surface local inhomogeneity on light scatter.

Fig. A.1 shows the measured BRDM elements as functions of observation angle for all samples. Each point presented in the figure is a result of averaging over 500 realizations of the single measurements. Except for the element (1,1) all matrix elements are normalized to the first one. There are no error bars shown in Fig. A.1 because values of the

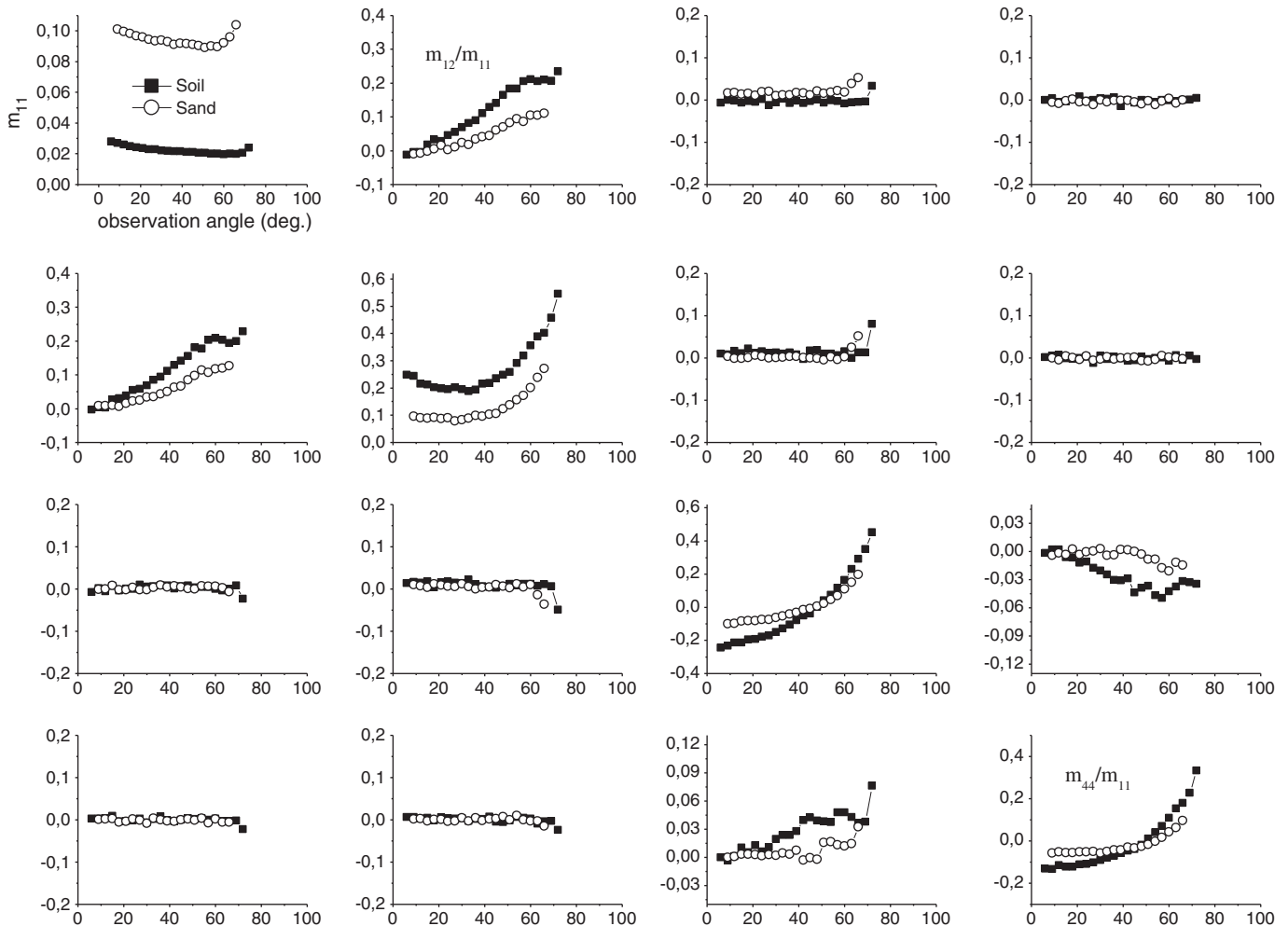
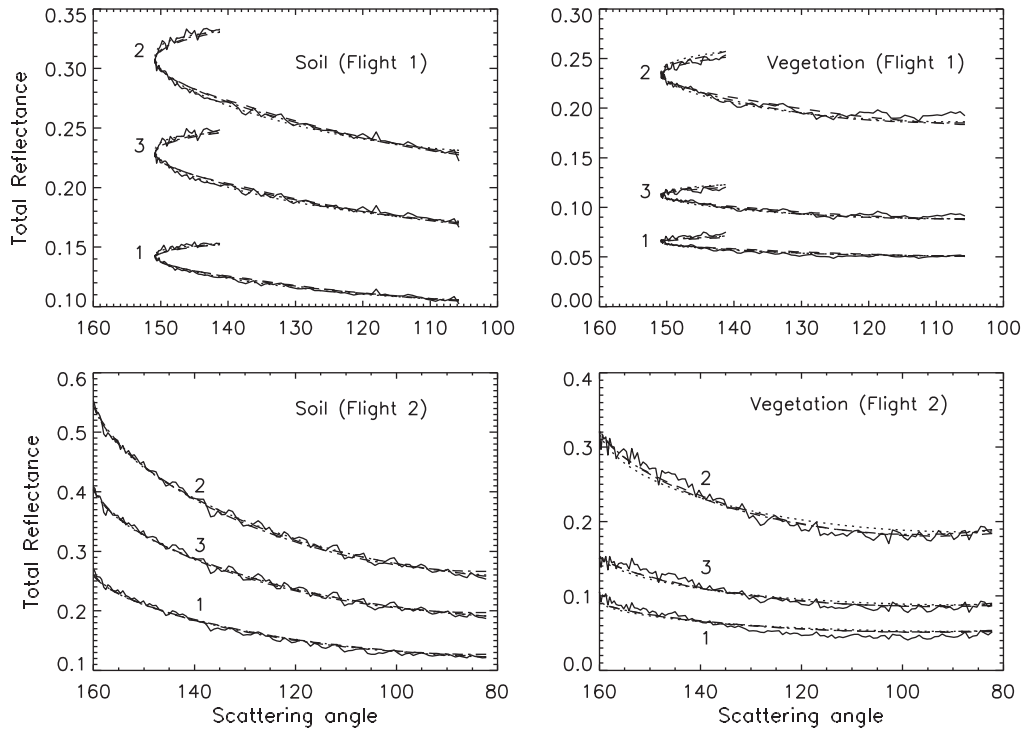


Fig. A.1. BRDM elements for soil and sand samples in the principal plane. The incident angle is  $10^\circ$  and the wavelength is 630 nm. Scattering angles range from  $90^\circ$  to  $165^\circ$ .



**Fig. A.2.** Angular dependences of the average total reflectance for soil and vegetated surfaces and for different RSP flights. The solid curves 1, 2, and 3 correspond to RSP data obtained in channels 4 (670 nm), 7 (1589 nm), and 9 (2264 nm), respectively. The dotted, dashed, and dash-dotted curves show the angular dependences of the BRDF according to the RPV, Ross-Roujean and Ross-Li models, respectively.

standard deviations are comparable with the symbols plotted and below 3%. To avoid potential calculation problems we investigated the reliability of the measured scattering matrices by checking that all of them satisfy the Cloude test (Cloude and Pottier, 1995) within the experimental errors at each observation angle. As it can be seen the eight matrix elements  $m_{13}$ ,  $m_{14}$ ,  $m_{23}$ ,  $m_{24}$ ,  $m_{31}$ ,  $m_{32}$ ,  $m_{41}$  and  $m_{42}$  are zero within the experimental errors over the entire observation angle range and, thus, the BRDM has a block-diagonal structure. The elements (3,4) and (4,3) are also close to zero. However, elements (2,2) and (3,3) are not negligible when observed in some specific directions. The element (1,3) is close to zero because the observations have been performed in the principal plane, when the normal to the layer and both light beams are in the same plane.

The semi-empirical models for the surface total and polarized reflectances  $R_t$  and  $R_p$  are used in practice. If single scattering by randomly oriented elementary surface (or volume) scattering elements gives the main contribution to the polarization of the scattered signal, then  $\mathfrak{R}_{21}$  and  $\mathfrak{R}_{31}$  are related to  $R_p$  via the following simple relations (Hovenier et al., 2004):

$$\mathfrak{R}_{21} = -R_p \cos 2\eta_v, \quad (\text{A.6})$$

$$\mathfrak{R}_{31} = -R_p \sin 2\eta_v, \quad (\text{A.7})$$

where the dihedral angle  $\eta_v$  is the angle between the scattering plane (the plane containing the solar and viewing directions) and the meridional plane containing the zenith and viewing directions. As shown by Litvinov et al. (2010), the relations (A.6) and (A.7) hold for isotropic soil and vegetated surfaces measured with the Research Scanning Polarimeter (RSP) (Cairns et al., 1999; Mishchenko et al., 2007b).

For surface reflectance description on the basis of satellite data, the bidirectional reflection distribution function (BRDF) and bidirectional polarization distribution function (BPDF) are used. When the definitions of surface total and polarized reflectances ( $R_t$  and  $R_p$ ) are given

by Eqs. (A.1)–(A.5), the BRDF and BPDF differ from  $R_t$  and  $R_p$  by the following normalization (Schaeppman-Strub et al., 2006):

$$\text{BRDF} = \frac{R_t}{\pi}, \quad \text{BPDF} = \frac{R_p}{\pi}. \quad (\text{A.8})$$

### A.3. A convenient parametric surface BRDM model

In passive aerosol remote sensing from space or aircraft, it is critical to properly capture the surface properties, including its spatial variability, in the retrieval algorithm since aerosol-laden atmospheres are generally semi-transparent. One novel solution is to enhance the atmospheric RT model by coupling it properly to an oceanic RT model, possibly with snow and ice layers between the air and the water, using Fresnel's laws of reflection and transmission at the interfaces (Zhai et al., 2009; Stamnes et al., 2011). That interfacing should account statistically for micro-scale surface roughening effects, e.g., wind over water. Another novel approach is to reduce the degeneracy of the surface contribution to the aerosol retrieval problem by using a “multi-pixel” analysis of multi-spectral and multiple-angular observations, taking into account that spatial variability of surface reflectance generally occurs over much shorter scales than for the overlying aerosol (Martonchik et al., 2002; Dubovik et al., 2011).

Retrieval methods based on optimal estimation are rapidly gaining popularity, and they call for fully parameterized forward models (as opposed, e.g., to LUTs). Therefore, to complement the parametric representation of aerosol presented in Section 3 of the main text, we need a parametric BRDM with sufficient generality. Following Xu et al. (2011a,b) and Diner et al. (2012), we consider a linear mixture of a depolarizing modified (Martonchik et al., 1998b; Rahman et al., 1993b) or “mRPV” model BRDF complemented with a generic microfacet model (Priest and Meier, 2002) for the polarizing element.

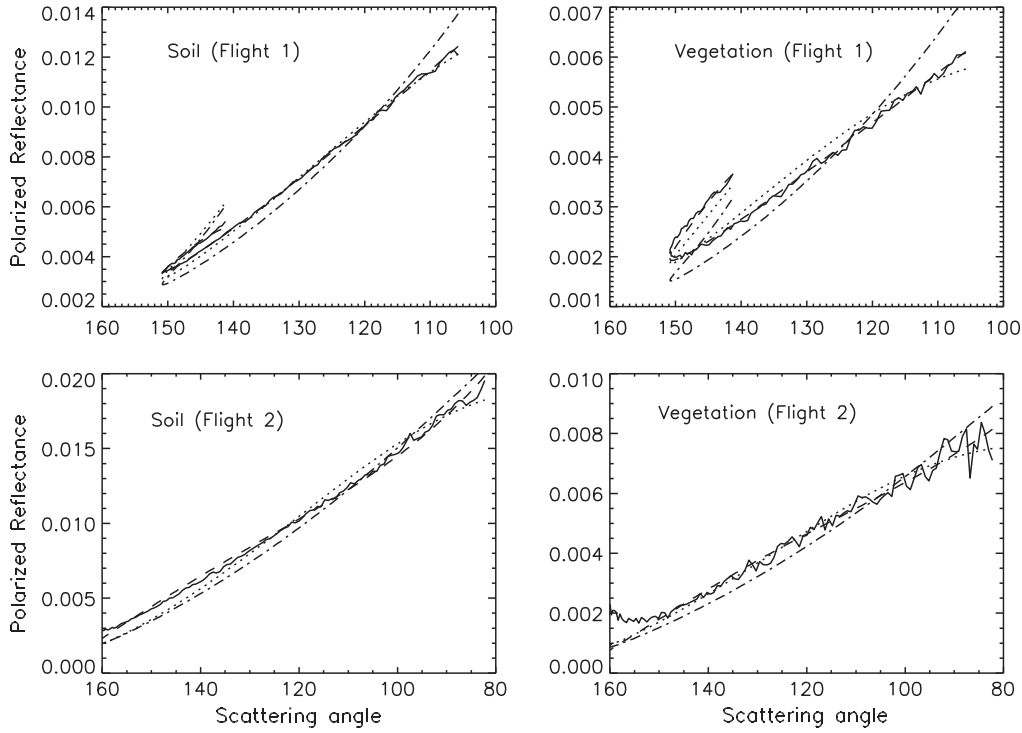


**Fig. A.3.** Angular dependences of the average surface polarized reflectance for soil and vegetated surfaces and for different RSP flights. The solid curve corresponds to RSP data obtained in channel 7 ( $\lambda = 1589$  nm). The dotted, dashed, and dash-dotted curves show the angular dependences of the polarized reflectance according to Nadal and Bréon (1999), modified Fresnel (Litvinov et al., 2011a,b), and linear one-parameter model (Maignan et al., 2009), respectively.

Using the notations adopted in Section 3, we have:

$$\begin{aligned} \rho_{\lambda}(\mu', \varphi' \rightarrow \mu, \varphi) &= (a_{\lambda}/\pi) [|\mu'| \mu (|\mu'| + \mu)]^{k-1} \exp(b\mu_s) \mathbf{diag}[1, 0, 0, 0] \\ &+ \zeta \times [p_w(\beta) / \cos\beta / (4|\mu'| \mu)] S_p(|\mu'|, \mu) \mathbf{L}(\pi - \gamma) \mathbf{F}(\theta_n, n_{s\lambda}) \mathbf{L}(-\gamma'), \end{aligned} \quad (\text{A.9})$$

where  $\mu_s = \cos\theta_s = \mathbf{\Omega}' \cdot \mathbf{\Omega}$  is the cosine of the surface-scattering angle, i.e.,  $-|\mu'| \mu + \eta' \eta \cos(\varphi' - \varphi)$ , where  $\eta = (1 - \mu^2)^{1/2}$  and similarly for  $\eta'$  in the present notations.

Parameters  $k$  and  $b$  in the first term of Eq. (A.9) govern the anisotropy of the surface reflectance in the absence of Fresnel reflectance by micro-facets ( $\zeta = 0$ ), and they are assumed  $\lambda$ -invariant;  $\mathbf{diag}[1, 0, 0, 0]$  is a diagonal matrix with the assigned values. Parameter  $a_{\lambda}$  is the surface albedo in the limit of a depolarizing Lambertian case ( $k = 1$ ,  $b = \zeta = 0$ ) and, in contrast to  $k$  and  $b$ , it can depend quite strongly on  $\lambda$ . Parameter  $k$  controls the overall shape of the BRDF part of the BRDM, as a function of incidence and reflection angles: if  $k < 1$ , we have a “bowl” shaped curve; if  $k > 1$ , it is “bell” shaped. Climatological values of  $k$  for diverse land-surfaces range from strongly anisotropic  $\approx 0.5$  to quasi-Lambertian  $\approx 0.9$  (R.A. Kahn, pers. comm.), all bowl-shaped. The original (and more popular) RPV model uses a Henyey–Greenstein term instead of  $\exp(b\mu_s)$  in Eq. (A.9); specifically, it becomes  $(1 + g^2 - 2g\mu_s)^{-3/2}$  where  $g$  replaces  $b$  as a parameter that, when positive (negative) reinforces surface scattering in the forward (backward) direction. But the exponential term facilitates linearization (Xu et al., 2012), which are required respectively for numerical solution of the 1D vRT equation and efficient retrievals. Climatological values of  $b$  for diverse land-surfaces range from quite strongly backscattering  $\approx -0.6$  to a weak forward-scattering trend  $\approx +0.06$  (R.A. Kahn, pers. comm.).

Parameter  $\zeta$  measures the relative strength of the polarizing microfacet component, the second term in Eq. (A.9), and it can be set to unity when the depolarizing component is presumed absent ( $a_{\lambda} = 0$ ), which is a reasonable assumption for the ocean surface (in the absence of

whitecaps and water-leaving radiance). When  $\zeta$  was used to fit AirMSPI data over land, it is found to be very small:  $< 0.05$  (Diner et al., 2013).

$\mathbf{F}(\theta_n, n_{s\lambda})$  is the  $4 \times 4$  block-diagonal Fresnel matrix for a reflecting surface with a complex refractive index  $n_{s\lambda}$  (with a generally weak dependence on  $\lambda$ ) under incident and reflection angles  $\theta_n$  (away from the randomly-oriented micro-facet normal). Per Snell’s law of reflection, we have  $\theta_n = (\pi - \cos^{-1}\mu_s) / 2$ , and the law of refraction yields  $\theta_r = \sin^{-1}(\sin\theta_n / \text{Re}[n_{s\lambda}])$ . Factoring in that  $F_{\lambda,21} = F_{\lambda,12}$  and  $F_{\lambda,43} = -F_{\lambda,34}$ ,  $\mathbf{F}$  has 4 independent elements:

$$\begin{aligned} F_{\lambda,11} &= \frac{r_p r_p^* + r_s r_s^*}{2}, & F_{\lambda,12} &= \frac{r_p r_p^* - r_s r_s^*}{2}, \\ F_{\lambda,33} &= \frac{r_p r_p^* + r_s r_p^*}{2}, & F_{\lambda,34} &= \frac{i(r_p r_p^* - r_s r_p^*)}{2}, \end{aligned} \quad (\text{A.10})$$

where

$$r_p = \frac{n_s \cos\theta_n - \cos\theta_r}{n_s \cos\theta_n + \cos\theta_r}, \quad r_s = \frac{\cos\theta_n - n_s \cos\theta_r}{\cos\theta_n + n_s \cos\theta_r}. \quad (\text{A.11})$$

The probability density function of the facet tilt angle  $\beta$  with respect to the macroscopic surface normal  $(1, 0, 0)^T$  is denoted  $p_w(\beta)$ .  $\beta$  is given by  $\cos\beta = (|\mu'| + \mu) / [2(1 - \mu_s)]^{1/2}$ . We use  $w$  to denote an optional parameter in the tilt angle PDF; it is reserved presently for the surface wind speed in the Cox and Munk (1954) model that is extensively used for roughened ocean surfaces. In that model,  $p_w(\beta)$  is taken to be a Gaussian distribution for  $\tan\beta$ . Specifically, we have

$$p_w(\beta) = \frac{\exp(-\tan^2\beta / 2s^2)}{2\pi s_w^2 \cos^3\beta}, \quad (\text{A.12})$$

where  $2s_w^2 = 0.003 + 0.00512w$  with  $w$  being the surface wind speed in m/s. Other possible choices are  $p(\beta) = \cos\beta / \pi$  for the Bréon et al. (1995) model. Alternatively, one can simply take a uniform distribution:  $p(\beta) = 1 / 2\pi$  (D.J. Diner, priv. comm.)

Finally,  $S_p(|\mu'|, \mu)$  is the shadowing function associated with that PDF for  $\beta$ —a requirement to conserve radiant energy. To the best of our knowledge,  $S_p(|\mu'|, \mu)$  is only known in explicit analytical form, so far, for two cases. On the one hand, it was computed by Smith (1967) for the Cox–Munk model in Eq. (A.12) when  $|\mu'| = 1$  (nadir viewing); generalized for random viewing geometry, we have (Tsang and Kong, 2001):

$$S_p(|\mu'|, \mu) = 1 / [1 + \Lambda_s(|\mu'|) + \Lambda_s(\mu)], \quad (\text{A.13})$$

where

$$\Lambda_s(\mu) = \frac{1}{2} \left[ \frac{\exp(-X^2/2)}{X\sqrt{\pi/2}} - \operatorname{erfc}\left(\frac{X}{\sqrt{2}}\right) \right]_{X=\frac{1}{\sqrt{\mu^2-1}}} \quad (\text{A.14})$$

On the other hand, Brown (1980) generalized Smith's (1967) method for non-Gaussian slopes, and evaluated  $S_p(1, \mu)$  explicitly for an exponential distribution. In essence,  $S_p(|\mu'|, \mu)$  is the probability that a point on the randomly rough surface is not in shadow when illuminated along a beam with SZA cosine  $\mu$ , nor is it hidden from view when the VZA cosine is  $|\mu'|$ .

Since all the above land-surface parameters are in principle added to the list of unknown aerosol properties for the retrieval, it is judicious to design algorithms emphasizing polarization that should have reduced sensitivity to surface reflection.

For the purposes of counting the unknown parameters in the atmosphere/surface remote sensing problem, the above hybrid model as, in summary, a maximum of as many values of  $a_x$  as there are wavelengths plus six entries assumed to be spectrally invariant ( $k, b; \zeta, w, n_{sr}, n_{si}$ ).

However,  $n_{si}$  is generally taken to be 0, and others ( $\zeta, w, n_{sr}$ ) are often assumed to be known quantities in the retrieval algorithms.

#### A.4. Discussion

A number of surface BRDF models have been used for surface reflection characterization from the Multi-angle Imaging SpectroRadiometer (MISR), the MODerate resolution Imaging Spectroradiometer (MODIS), and the Polarization and Directionality of Earth's Reflectances (POLDER) instruments: predominantly, the Rahman–Pinty–Verstraete (RPV) and modified RPV (mRPV) models as well as their kernel-based counterparts (Ross–Li and Ross–Roujean models).

For characterization of atmospheric aerosol over land surfaces using POLDER data, the Nadal–Bréon model for polarized reflectance is used (Nadal and Bréon, 1999). More recently, Maignan et al. (2009) introduced for POLDER surface polarized reflectance characterization, a new linear BPDF model with only one free parameter. The RSP airborne instrument provides very accurate surface polarized reflectance measurements (Cairns et al., 1999; Mishchenko et al., 2007b). For accurate description of such measurements, Litvinov et al. (2011a,b) proposed a three-parameter semi-empirical model.

Maignan et al. (2004, 2009) performed an extensive comparison of different BRDF and BPDF models with POLDER satellite data. For the BRDF, Maignan et al. (2004) found that the RPV model (Rahman et al., 1993a,b) and the Ross–Li model (Ross, 1981; Li and Strahler, 1992; Wanner et al., 1995) are both capable of reproducing POLDER measurements, except for the so-called “hot spot” region (the angular region near exact backscattering). To take into account the hot spot effect, also known as the opposition effect, BRDF models must be modified (see, for example, Rahman et al., 1993a,b; Maignan et al., 2004). For

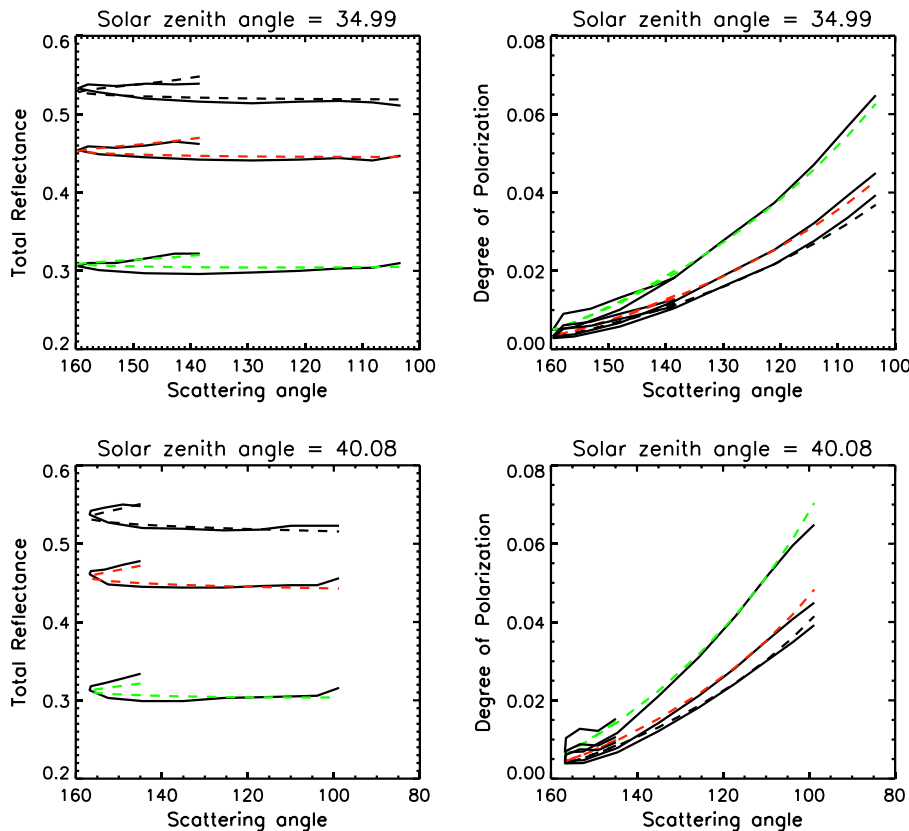


Fig. A.4. Angular dependences of total reflectance and DOLP for a desert surface. The solid curves correspond to POLDER data. The dashed curves show the angular dependences of the model BRDF and the DOLP (Litvinov et al., 2012) for  $\lambda = 565$  nm (green curve),  $\lambda = 670$  nm (red curve) and  $\lambda = 865$  nm (black curve).

the BPDF, it was found that the one-parameter model allows a similar fit to the POLDER data as the previously developed Nadal–Bréon model (Nadal and Bréon, 1999). The cases of highly reflective surfaces such as snow, ice and foam can be treated using the physics-based surface reflection models (Kokhanovsky, 2004; Kokhanovsky and Bréon, 2012).

Examples of fitting the semi-empirical BRDF and BPDF models to RSP measurements are shown on Figs. A.2–A.3. Because of their lack of physical basis, the parameters of the semi-empirical BRDF models are not necessarily consistent with the parameters of the semi-empirical BPDF models. Moreover they are weakly related, or not related at all, to the actual physical parameters of the scattering surfaces. That complicates land surface properties characterization and introduces many uncertainties into the problem of aerosol properties retrieval over land (Litvinov et al., 2011a,b).

Natural land surfaces can be very complex scattering objects, which differ by their physical, optical, geometrical, statistical, etc. properties. The physical description of scattering by such media can be quite complicated. Moreover, there cannot be one universal physically based BRDM model, which could be applied to all possible types of surfaces. Nevertheless, very often the type of a surface can be known or easily established (for example, bare soil, desert, vegetated surfaces, etc.). In this case, use of physics-based models of BRDM for aerosol retrieval over land can gain an advantage over the semi-empirical ones. Moreover the physical models of BRDM are very important on their own for surface characterization. At present time, there are, on the one hand, spaceborne and airborne instruments that provide multi-spectral, multi-angle photopolarimetric measurements over a broad variety of land surfaces that can be used in the evaluation of the physical models of BRDM for land surfaces (Deschamps et al., 1994; Cairns et al., 1999). On the other hand, major progress has now been achieved in the theory of light scattering by random media. It is not yet utilized in the existing BRDF and BPDF models for the visible and near-infrared spectral regions (see, for example, Tsang and Kong, 2001; Muinonen, 2004; Tishkovets and Jockers, 2006; Tishkovets and Mishchenko, 2009; Tishkovets et al., 2011; Mishchenko et al., 2006). In general, most of these approaches are very complicated or time consuming to be used in the retrieval schemes (for example, for aerosol retrieval over land). They can be used as a starting point for obtaining simplified physical BRDM models (Litvinov et al., 2012). An example of fitting such physical BRDM model to PARASOL measurements is shown in the panels of Fig. A.4 (see Litvinov et al., 2012 for details).

Sensitivity studies show that the retrieval of aerosol microphysical properties from remote sensing satellite data requires highly accurate TOA photometric and polarimetric signal prediction; see, for example, Hasekamp and Landgraf (2007) and Mishchenko et al. (2007a). The high quality aerosol products require advanced models of the surface reflectance (Dubovik et al., 2011). To reduce these uncertainties, both robust algorithms for the separation of the atmospheric/surface signals; see, e.g., Dubovik et al. (2000) and Hasekamp et al. (2011), and more physically based models of the BRDF/BPDF (BRDM in general) are required (Litvinov et al., 2012). In such physics-based models, the BRDF and BRDM model parameters would be related to each other, and physical constraints would be imposed by the surface structure and composition; see, e.g., the discussion by Mishchenko et al. (2011).

## References

- Aires, F., Chédin, A., Scott, N.A., Rossow, W.B., 2002. A regularized neural net approach for retrieval of atmospheric and surface temperatures with the IASI instrument. *J. Appl. Meteorol.* 41, 144–159. [http://dx.doi.org/10.1175/1520-0450\(2002\)041<0144:ARNNAF>2.0.CO;2](http://dx.doi.org/10.1175/1520-0450(2002)041<0144:ARNNAF>2.0.CO;2).
- Babenko, V.A., Astafyeva, L.G., Kuzmin, V.N., 2003. *Electromagnetic Scattering in Disperse Media: Inhomogeneous and Anisotropic Particles*. Springer-Praxis, Chichester, United Kingdom.
- Barton, I.J., Scott, J.C., 1986. Remote measurements of surface pressure using absorption in the oxygen A-band. *Appl. Opt.* 25, 3502–3507. <http://dx.doi.org/10.1364/AO.25.003502>.
- Biron, D., Lupi, G., Montini, G., Labate, D., Bruno, U., Melfi, D., Sist, M., Zauli, F., de Leonibus, L., 2013. METOP-SG 3MI (Multi-viewing Multi-channel Multi-polarization Imaging), a powerful observing mission for future operational applications. *Proc. EUMETSAT Meteorological Satellite Conference*, Vienna, Austria, 16–20 September 2013.
- Blackwell, W.J., 2005. A neural-network technique for the retrieval of atmospheric temperature and moisture profiles from high spectral resolution sounding data. *IEEE Trans. Geosci. Remote Sens.* 43, 2535–2546. <http://dx.doi.org/10.1109/TGRS.2005.855071>.
- Boesche, E., Stammes, P., Preusker, R., Bennartz, R., Knap, W., Fischer, J., 2008. Polarization of skylight in the O<sub>2</sub> A-band: effects of aerosol properties. *Appl. Opt.* 47, 3467–3480. <http://dx.doi.org/10.1364/AO.47.003467>.
- Boucher, O., Randall, D., Artaxo, P., Bretherton, C., Feingold, G., Forster, P., Kerminen, V.M., Kondo, Y., Liao, H., Lohmann, U., Rasch, P., Satheesh, S.K., Sherwood, S., Stevens, B., Zhang, X.Y., 2013. Clouds and aerosols. In: Stocker, T.F., Qin, D., Plattner, K.F., Tignor, M., Allen, S.K., Boschung, J., Nauels, A., Xia, Y., Bex, V., Midgley, P.M. (Eds.), *Climate Change 2013: The Physical Science Basis. Contribution of Working Group I to the Fifth Assessment Report of the Intergovernmental Panel on Climate Change*. Cambridge University Press, Cambridge, United Kingdom and New York, NY, United States, pp. 571–657 (Chapter 5).
- Bréon, F.-M., Tanré, D., Lecomte, P., Herman, M., 1995. Polarized reflectance of bare soils and vegetation: measurements and models. *IEEE Trans. Geosci. Remote Sens.* 33, 487–499. <http://dx.doi.org/10.1109/36.377949>.
- Brown, G.S., 1980. Shadowing by non-Gaussian random surfaces. *IEEE Trans. Antennas Propag.* 28, 788–790. <http://dx.doi.org/10.1109/TAP.1980.1142437>.
- Burazerovic, D., Heylen, R., Geens, B., Sterckx, S., Scheunders, P., 2013. Detecting the adjacency effect in hyperspectral imagery with spectral unmixing techniques. *IEEE J. Sel. Top. Appl. Earth Observ. Remote Sens.* 6, 1070–1078. <http://dx.doi.org/10.1109/JSTARS.2013.2240656>.
- Cairns, B., Russell, E.E., Travis, L.D., 1999. Research Scanning Polarimeter: calibration and ground-based measurements. *Proc. SPIE 3754, Polarization: Measurement, Analysis, and Remote Sensing II*, p. 186–<http://dx.doi.org/10.1117/12.366329>.
- Chand, D., Wood, R., Ghan, S.J., Wang, M., Ovchinnikov, M., Rasch, P.J., Miller, S., Schichtel, B., Moore, T., 2012. Aerosol optical depth increase in partly cloudy conditions. *J. Geophys. Res.* 117, D17207. <http://dx.doi.org/10.1029/2012JD017894>.
- Cheng, T., Gu, X., Xie, D., Li, Z., Yu, T., Chen, X., 2011. Simultaneous retrieval of aerosol optical properties over the Pearl River Delta, China using multi-angular, multi-spectral, and polarized measurements. *Remote Sens. Environ.* 115, 1643–1652. <http://dx.doi.org/10.1016/j.rse.2011.02.020>.
- Cheng, T., Gu, X., Xie, D., Li, Z., Yu, T., Chen, H., 2012. Aerosol optical depth and fine-mode fraction retrieval over East Asia using multi-angular total and polarized remote sensing. *Atmos. Meas. Tech.* 5, 501–516. <http://dx.doi.org/10.5194/amt-5-501-2012>.
- Cheng, T., Gu, X., Wu, Y., Chen, H., Yu, T., 2013. The optical properties of absorbing aerosols with fractal soot aggregates: implications for aerosol remote sensing. *J. Quant. Spectrosc. Radiat. Transf.* 125, 93–104. <http://dx.doi.org/10.1016/j.jqsrt.2013.03.012>.
- Chipman, R.A., 1994. *Polarimetry*. In: Bass, M. (Ed.), 2nd ed. *Handbook of Optics: Devices, Measurements and Properties vol. II*. McGraw-Hill, New York, NY, United States, pp. 1–37 (Chapter 22).
- Chowdhary, J., Cairns, B., Travis, L.D., 2006. Contribution of water-leaving radiances to multiangle, multispectral polarimetric observations over the open ocean: bio-optical model results for case 1 waters. *Appl. Opt.* 45, 5542–5567. <http://dx.doi.org/10.1364/AO.45.005542>.
- Cloude, S.R., Pottier, E., 1995. *Concept of polarization entropy in optical scattering*. *Opt. Eng.* 34, 1599–1610.
- Cox, C., Munk, W., 1954. Measurement of the roughness of the sea surface from photographs of the Sun's glitter. *J. Opt. Soc. Am.* 44, 838–850. <http://dx.doi.org/10.1364/JOSA.44.000838>.
- Crisp, D., Atlas, R.M., Bréon, F.-M., Brown, L.R., Burrows, J.P., Ciaï, P., Connor, B.J., Doney, S.C., Fung, I.Y., Jacob, D.J., Miller, C.E., O'Brien, D., Pawson, S., Randerson, J., Rayner, P., Salawitch, R.J., Sander, S.P., Sen, B., Stephens, G.L., Tans, P.P., Toon, G.C., Wennberg, P.O., Wofsy, S.C., Yung, Y.L., Kuang, Z., Chudasama, B., Sprague, G., Weiss, B., Pollock, R., Kenyon, D., Schroll, S., 2004. *The Orbiting Carbon Observatory (OCO) mission*. *Adv. Space Res.* 34, 700–709.
- Davis, A., Marshak, A., Cahalan, R., Wiscombe, W., 1997. The Landsat scale break in stratocumulus as a three-dimensional radiative transfer effect: implications for cloud remote sensing. *J. Atmos. Sci.* 54, 241–260. [http://dx.doi.org/10.1175/1520-0469\(1997\)054<0241:TLBSIS>2.0.CO;2](http://dx.doi.org/10.1175/1520-0469(1997)054<0241:TLBSIS>2.0.CO;2).
- Davis, A.B., Marshak, A., 2002. Space-time characteristics of light transmitted through dense clouds: a Green's function analysis. *J. Atmos. Sci.* 59, 2713–2727. [http://dx.doi.org/10.1175/1520-0469\(2002\)059<2713:STCOLT>2.0.CO;2](http://dx.doi.org/10.1175/1520-0469(2002)059<2713:STCOLT>2.0.CO;2).
- Davis, A.B., Garay, M.J., Xu, F., Qu, Z., Emde, C., 2013. 3D radiative transfer effects in multi-angle/multispectral radio-polarimetric signals from a mixture of clouds and aerosols viewed by a non-imaging sensor. *Proc. SPIE 8873, Polarization Science and Remote Sensing VI*, p. 887309 <http://dx.doi.org/10.1117/12.2023733>.
- Davis, A.B., Sanghavi, S.V., Diner, D.J., Kalashnikova, O.V., Garay, M.J., Martonchik, J.V., Natraj, V., Xu, F., Zhai, P., Korkin, S.V., Lyapustin, A.I., Rozanov, V.V., Kokhanovsky, A.A., 2015. Benchmarking 1D scalar and vector radiative transfer code accuracy, with multi-angle aerosol remote sensing in mind (in preparation).
- de Haan, J.F., Bosma, P.B., Hovenier, J.W., 1987. The adding method for multiple scattering calculations of polarized light. *Astron. Astrophys.* 183, 371–391.
- Del Frate, F., Ortenzi, A., Casadio, S., Zehner, C., 2002. Application of neural algorithms for a real-time estimation of ozone profiles from GOME measurements. *IEEE Trans. Geosci. Remote Sens.* 40, 2263–2270. <http://dx.doi.org/10.1109/TGRS.2002.803622>.
- Deschamps, P.Y., Bréon, F.M., Leroy, M., Podaire, A., Bricaud, A., Buriez, J.C., Sèze, G., 1994. The POLDER mission: instrument characteristics and scientific objectives. *IEEE Trans. Geosci. Remote Sens.* 32, 598–615. <http://dx.doi.org/10.1109/36.297978>.

- Deuzé, J.L., Herman, M., Goloub, P., Tanré, D., Marchand, A., 1999. Characterization of aerosols over ocean POLDER/ADEOS-1. *Geophys. Res. Lett.* 26, 1421–1424. <http://dx.doi.org/10.1029/1999GL900168>.
- Deuzé, J.L., Bréon, F., Devaux, C., Goloub, P., Herman, M., Lafrance, B., Maignan, F., Marchand, A., Nadal, F., Perry, G., Tanré, D., 2001. Remote sensing of aerosols over land surfaces from POLDER-ADEOS-1 polarized measurements. *J. Geophys. Res.* 106, 4913–4926. <http://dx.doi.org/10.1029/2000JD900364>.
- Di Noia, A., Hasekamp, O.P., van Harten, G., Rietjens, J.H.H., Smit, J.M., Snik, F., Henzing, J.S., de Boer, J., Keller, C.U., Volten, H., 2015. Use of neural networks in ground-based aerosol retrievals from multi-angle spectropolarimetric observations. *Atmos. Meas. Tech.* 8, 281–299. <http://dx.doi.org/10.5194/amt-8-281-2015>.
- Diner, D.J., Martonchik, J.V., 1984a. Atmospheric transfer of radiation above an inhomogeneous non-Lambertian reflective ground—I. Theory. *J. Quant. Spectrosc. Radiat. Transf.* 31, 97–125. [http://dx.doi.org/10.1016/0022-4073\(84\)90109-2](http://dx.doi.org/10.1016/0022-4073(84)90109-2).
- Diner, D.J., Martonchik, J.V., 1984b. Atmospheric transfer of radiation above an inhomogeneous non-Lambertian reflective ground—II. Computational considerations and results. *J. Quant. Spectrosc. Radiat. Transf.* 32, 279–304. [http://dx.doi.org/10.1016/0022-4073\(84\)90100-6](http://dx.doi.org/10.1016/0022-4073(84)90100-6).
- Diner, D.J., Davis, A.B., Hancock, B., Gutt, G., Chipman, R.A., Cairns, B., 2007. Dual-photoelastic-modulator-based polarimetric imaging concept for aerosol remote sensing. *Appl. Opt.* 46, 8428–8445. <http://dx.doi.org/10.1364/AO.46.008428>.
- Diner, D.J., Hodos, R.A., Davis, A.B., Garay, M.J., Martonchik, J.V., Sanghavi, S.V., von Allmen, P., Kokhanovsky, A.A., Zhai, P., 2011. An optimization approach for aerosol retrievals using simulated MISR radiances. *Atmos. Res.* 116, 1–14. <http://dx.doi.org/10.1016/j.atmosres.2011.05.020>.
- Diner, D.J., Xu, F., Martonchik, J.V., Rheingans, B.E., Geier, S., Jovanovic, V.M., Davis, A., Chipman, R.A., McClain, S.C., 2012. Exploration of a polarized surface bidirectional reflectance model using the ground-based Multiangle SpectroPolarimetric Imager. *Atmosphere* 3, 591–619. <http://dx.doi.org/10.3390/atmos3040591>.
- Diner, D.J., Xu, F., Garay, M.J., Martonchik, J.V., Rheingans, B.E., Geier, S., Davis, A.B., Hancock, B.R., Jovanovic, V.M., Bull, M.A., Capraro, K., Chipman, R.A., McClain, S.C., 2013. The Airborne Multiangle SpectroPolarimetric Imager (AirMSPI): a new tool for aerosol and cloud remote sensing. *Atmos. Meas. Tech.* 6, 2007–2025. <http://dx.doi.org/10.5194/amt-6-2007-2013>.
- Dubovik, O., King, M.D., 2000. A flexible inversion algorithm for retrieval of aerosol optical properties from Sun and sky radiance measurements. *J. Geophys. Res.* 105, 20,673–20,796. <http://dx.doi.org/10.1029/2000JD900282>.
- Dubovik, O., Smirnov, A., Holben, B.N., King, M.D., Kaufman, Y.J., Eck, T.F., Slutsker, I., 2000. Accuracy assessments of aerosol optical properties retrieved from Aerosol Robotic Network (AERONET) Sun and sky radiance measurements. *J. Geophys. Res.* 105, 9791–9806. <http://dx.doi.org/10.1029/2000JD900040>.
- Dubovik, O., Holben, B.N., Eck, T.F., Smirnov, A., Kaufman, Y.J., King, M.D., Tanré, D., Slutsker, I., 2002. Variability of absorption and optical properties of key aerosol types observed in worldwide locations. *J. Atmos. Sci.* 59, 590–608. [http://dx.doi.org/10.1175/1520-0469\(2002\)059<0590:VOAOP>2.0.CO;2](http://dx.doi.org/10.1175/1520-0469(2002)059<0590:VOAOP>2.0.CO;2).
- Dubovik, O., 2004. Optimization of numerical inversion in photopolarimetric remote sensing. In: Videen, G., Yatskiv, Y., Mishchenko, M. (Eds.), *Photopolarimetry in Remote Sensing*. Kluwer Academic Publishers, Dordrecht, Netherlands, pp. 65–106.
- Dubovik, O., Sinyuk, A., Lapyonok, T., Holben, B.N., Mishchenko, M., Yang, P., Eck, T.F., Volten, H., Muñoz, O., Veihelmann, B., van der Zande, W.J., Leon, J.F., Sorokin, M., Slutsker, I., 2006. Application of spheroidal models to account for aerosol particle nonsphericity in remote sensing of desert dust. *J. Geophys. Res.* 111, D11208. <http://dx.doi.org/10.1029/2005JD006619>.
- Dubovik, O., Herman, M., Holdak, A., Lapyonok, T., Tanré, D., Deuzé, J.L., Ducos, F., Sinyuk, A., Lopatin, A., 2011. Statistically optimized inversion algorithm for enhanced retrieval of aerosol properties from spectral multi-angle polarimetric satellite observations. *Atmos. Meas. Tech.* 4, 975–1018. <http://dx.doi.org/10.5194/amt-4-975-2011>.
- Dubovik, O., Lapyonok, T., Litvinov, P., Herman, M., Fuertes, D., Ducos, F., Lopatin, A., Chaikovskiy, A., Torres, B., Derimian, Y., Huang, X., Aspetsberger, M., Federspiel, C., 2014. “GRASP: a versatile algorithm for characterizing the atmosphere”. *SPIE: Newsroom* <http://dx.doi.org/10.1117/2.1201408.005558>, Published Online: September 19, 2014. <http://spie.org/x109993.xml>.
- Evans, K.F., Stephens, G.L., 1991. A new polarized atmospheric radiative transfer model. *J. Quant. Spectrosc. Radiat. Transf.* 46, 413–423. [http://dx.doi.org/10.1016/0022-4073\(91\)90043-P](http://dx.doi.org/10.1016/0022-4073(91)90043-P).
- Ferlay, N., Thieuleux, F., Cornet, C., Davis, A.B., Dubuisson, P., Ducos, F., Parol, F., Riédi, J., Vanbauc, C., 2010. Toward New Inferences about Cloud Structures from Multidirectional Measurements in the Oxygen A Band: Middle-of-Cloud Pressure and Cloud Geometrical Thickness from POLDER-3/PARASOL. *J. Appl. Meteor. Climatol.* 49, 2492–2507. <http://dx.doi.org/10.1175/2010JAMC2550.1>.
- Gabella, M., Kisselev, V., Perona, G., 1999. Retrieval of aerosol profile variations from reflected radiation in the oxygen absorption A band. *Appl. Opt.* 38, 3190–3195. <http://dx.doi.org/10.1364/AO.38.003190>.
- Grant, I.P., Hunt, G.E., 1969a. Discrete space theory of radiative transfer. I. Fundamentals. *Proc. R. Soc. Lond. A* 313 (1513), 183–197. <http://dx.doi.org/10.1098/rspa.1969.0187>.
- Grant, I.P., Hunt, G.E., 1969b. Discrete space theory of radiative transfer. II. Stability and non-negativity. *Proc. R. Soc. Lond. A* 313 (1513), 199–216. <http://dx.doi.org/10.1098/rspa.1969.0188>.
- Hansen, J.E., 1971a. Multiple scattering of polarized light in planetary atmospheres. Part I. The doubling method. *J. Atmos. Sci.* 28, 120–125. [http://dx.doi.org/10.1175/1520-0469\(1971\)028<0120:MSOPLI>2.0.CO;2](http://dx.doi.org/10.1175/1520-0469(1971)028<0120:MSOPLI>2.0.CO;2).
- Hansen, J.E., 1971b. Multiple scattering of polarized light in planetary atmospheres. Part II. Sunlight reflected by terrestrial water clouds. *J. Atmos. Sci.* 28, 1400–1426. [http://dx.doi.org/10.1175/1520-0469\(1971\)028<1400:MSOPLI>2.0.CO;2](http://dx.doi.org/10.1175/1520-0469(1971)028<1400:MSOPLI>2.0.CO;2).
- Hansen, J.E., Hovenier, J.W., 1974. Interpretation of the polarization of Venus. *J. Atmos. Sci.* 31, 1137–1160. [http://dx.doi.org/10.1175/1520-0469\(1974\)031<1137:OTPOV>2.0.CO;2](http://dx.doi.org/10.1175/1520-0469(1974)031<1137:OTPOV>2.0.CO;2).
- Hansen, J.E., Travis, L.D., 1974. Light scattering in planetary atmospheres. *Space Sci. Rev.* 16, 527–610. <http://dx.doi.org/10.1007/BF00168069>.
- Hansen, P.C., O’Leary, D.P., 1993. The use of the L-curve in the regularization of discrete ill-posed problems. *SIAM J. Sci. Comput.* 14, 1487–1503. <http://dx.doi.org/10.1137/0914086>.
- Hasekamp, O.P., Landgraf, J., 2002. A linearized vector radiative transfer model for atmospheric trace gas retrieval. *J. Quant. Spectrosc. Radiat. Transf.* 75, 221–238. [http://dx.doi.org/10.1016/S0022-4073\(01\)00247-3](http://dx.doi.org/10.1016/S0022-4073(01)00247-3).
- Hasekamp, O.P., Landgraf, J., 2005. Retrieval of aerosol properties over the ocean from multispectral single-viewing-angle measurements of intensity and polarization: retrieval approach, information content, and sensitivity study. *J. Geophys. Res.* 110, D20207. <http://dx.doi.org/10.1029/2005JD006212>.
- Hasekamp, O.P., Landgraf, J., 2007. Retrieval of aerosol properties over land surfaces: capabilities of multiple-viewing-angle intensity and polarization measurements. *Appl. Opt.* 46, 3332–3344. <http://dx.doi.org/10.1364/AO.46.003332>.
- Hasekamp, O.P., 2010. Capability of multi-viewing-angle photo-polarimetric measurements for the simultaneous retrieval of aerosol and cloud properties. *Atmos. Meas. Tech.* 3, 839–851. <http://dx.doi.org/10.5194/amt-3-839-2010>.
- Hasekamp, O.P., Litvinov, P., Butz, A., 2011. Aerosol properties over the ocean from PARASOL multiangle photopolarimetric measurements. *J. Geophys. Res.* 116, D14204. <http://dx.doi.org/10.1029/2010JD015469>.
- Hélière, A., Gelsthorpe, R., Le Hors, L., Toulemon, Y., 2012. ATLID, the atmospheric lidar on board the EarthCARE satellite. Proceedings of the International Conference on Space Optics (ICSO), Ajaccio, Corse, France, Oct. 9–12, 2012, Paper: ICSO-065.
- Heidinger, A., Stephens, G.L., 2000. Molecular line absorption in a scattering atmosphere, part II: application to remote sensing in the O<sub>2</sub> A-band. *J. Atmos. Sci.* 57, 1615–1634. [http://dx.doi.org/10.1175/1520-0469\(2000\)057<1615:MLAIAS>2.0.CO;2](http://dx.doi.org/10.1175/1520-0469(2000)057<1615:MLAIAS>2.0.CO;2).
- Herman, M., Deuzé, J.L., Devaux, C., Goloub, P., Bréon, F.M., Tanré, D., 1997. Remote sensing of aerosols over land surfaces including polarization measurements and application to POLDER measurements. *J. Geophys. Res.* 102, 17,039–17,049. <http://dx.doi.org/10.1029/96JD02109>.
- Herman, M., Deuzé, J.L., Marchand, A., Roger, B., Lallart, P., 2005. Aerosol remote sensing from POLDER/ADEOS over the ocean: improved retrieval using a nonspherical particle model. *J. Geophys. Res.* 110, D10S02. <http://dx.doi.org/10.1029/2004JD004798>.
- Holben, B.N., Eck, T.F., Slutsker, I., Tanré, D., Buis, J.P., Setzer, A., Vermote, E., Reagan, J.A., Kaufman, Y.J., Nakajima, T., Lavenu, F., Jankowiak, I., Smirnov, A., 1998. AERONET — a federated instrument network and data archive for aerosol characterization. *Remote Sens. Environ.* 66, 1–16. [http://dx.doi.org/10.1016/S0034-4257\(98\)00031-5](http://dx.doi.org/10.1016/S0034-4257(98)00031-5).
- Hovenier, J.W., van der Mee, C., Domke, H., 2004. *Transfer of Polarized Light in Planetary Atmospheres*. Springer, Berlin, Germany.
- Imaoka, K., Kachi, M., Fujii, H., Murakami, H., Hori, M., Ono, A., Igarashi, T., Nakagawa, K., Oki, T., Honda, Y., Shimoda, H., 2010. Global Change Observation Mission (GCOM) for monitoring carbon, water cycles, and climate change. *Proc. IEEE* 98, 717–734. <http://dx.doi.org/10.1109/JPROC.2009.2036869>.
- Jäkel, E., Wendisch, M., Mayer, B., 2013. Influence of spatial heterogeneity of local surface albedo on the area-averaged surface albedo retrieved from airborne irradiance measurements. *Atmos. Meas. Tech.* 6, 527–537. <http://dx.doi.org/10.5194/amt-6-527-2013>.
- Jethva, H., Torres, O., Remer, L.A., Bhartia, P.K., 2013. A color ratio method for simultaneous retrieval of aerosol and cloud optical thickness of above-cloud absorbing aerosols from passive sensors: application to MODIS measurements. *IEEE Trans. Geosci. Remote Sens.* 51, 3862–3870. <http://dx.doi.org/10.1109/TGRS.2012.2230008>.
- Jiang, Y., Jiang, X., Shia, R.-L., Sander, S.P., Yung, Y.L., 2003. Polarization study of the O<sub>2</sub> A-band and its application to the retrieval of O<sub>2</sub> column abundance. *EOS Trans. Am. Geophys. Union* 84 (255), A41E–A0735E.
- Jones, S.H., Iannarilli, F.J., Kebabian, P.L., 2004. Realization of quantitative-grade fieldable snapshot imaging spectropolarimeter. *Opt. Express* 12, 6559–6573. <http://dx.doi.org/10.1364/OPEX.12.006559>.
- Kahn, R.A., Gaitley, B.J., Garay, M.J., Diner, D.J., Eck, T.F., Smirnov, A., Holben, B.N., 2010. Multiangle Imaging SpectroRadiometer global aerosol product assessment by comparison with the Aerosol Robotic Network. *J. Geophys. Res.* 115, D23209. <http://dx.doi.org/10.1029/2010JD014601>.
- Kahnert, M., Nousiainen, T., Thomas, M.A., Tyynelä, J., 2012. Light scattering by particles with small-scale surface roughness: comparison of four classes of model geometries. *J. Quant. Spectrosc. Radiat. Transf.* 113, 2356–2367. <http://dx.doi.org/10.1016/j.jqsrt.2012.03.017>.
- Kalashnikova, O.V., Garay, M.J., Davis, A.B., Diner, D.J., Martonchik, J.V., 2011. Sensitivity of multi-angle photo-polarimetry to vertical layering and mixing of absorbing aerosols: quantifying measurement uncertainties. *J. Quant. Spectrosc. Radiat. Transf.* 112, 2149–2163. <http://dx.doi.org/10.1016/j.jqsrt.2011.05.010>.
- Kaufman, Y.J., 1982. Solution of the equation of radiative transfer for remote sensing over nonuniform surface reflectivity. *J. Geophys. Res.* 87, 4137–4147. <http://dx.doi.org/10.1029/JC087iC06p04137>.
- Kaufman, Y.J., Remer, L.A., Tanre, D., Li, R.-R., Kleidman, R., Mattoo, S., Levy, R.C., Eck, T.F., Holben, B.N., Ichoku, C., Martins, J.V., Koren, I., 2005. A critical examination of the residual cloud contamination and diurnal sampling effects on MODIS estimates of aerosol over ocean. *IEEE Trans. Geosci. Remote Sens.* 43, 2886–2897. <http://dx.doi.org/10.1109/TGRS.2005.858430>.
- Keller, C.U., 2001. Instrumentation for astrophysical spectropolarimetry. In: Trujillo-Bueno, J., Moreno-Insertis, F., Sanchez, F. (Eds.), *Astrophysical Spectropolarimetry*. Cambridge University Press, Cambridge, United Kingdom and New York, NY, United States, pp. 303–354. <http://dx.doi.org/10.1017/CBO9780511564802.012> (Chapter 8).
- Kemp, J.C., Swedlund, J.B., Murphy, R.E., Wolstencroft, R.D., 1971a. Physical sciences: circularly polarized visible light from Jupiter. *Nature* 231, 169–170. <http://dx.doi.org/10.1038/231169a0>.

- Kemp, J.C., Wolstencroft, R.D., Swedlund, J.B., 1971b. Circular polarization: Jupiter and other planets. *Nature* 232, 165–168. <http://dx.doi.org/10.1038/232165a0>.
- King, M.D., Kaufman, Y.J., Menzel, W.P., Tanré, D., 1992. Remote sensing of cloud, aerosol, and water vapor properties from the moderate resolution imaging spectrometer (MODIS). *IEEE Trans. Geosci. Remote Sens.* 30, 2–27. <http://dx.doi.org/10.1109/36.124212>.
- King, M.D., Kaufman, Y.J., Tanré, D., Nakajima, T., 1999. Remote sensing of tropospheric aerosols from space: past, present, and future. *Bull. Am. Meteorol. Soc.* 80, 2229–2259.
- Kinne, S., O'Donnell, D., Stier, P., Kloster, S., Zhang, K., Schmidt, H., Rast, S., Giorgetta, M., Eck, T.F., Stevens, B., 2013. MAC-v1: a new global aerosol climatology for climate studies. *J. Adv. Model. Earth Syst.* 5, 704–740. <http://dx.doi.org/10.1002/jame.20035>.
- Knibbe, W.J.J., de Haan, J.F., Hovenier, J.W., Stam, D.M., Koelmeijer, R.B.A., Stammes, P., 2000. Deriving terrestrial cloud top pressure from photopolarimetry of reflected light. *J. Quant. Spectrosc. Radiat. Transf.* 64, 173–199. [http://dx.doi.org/10.1016/S0022-4073\(98\)00135-6](http://dx.doi.org/10.1016/S0022-4073(98)00135-6).
- Knobelspiesse, K., Cairns, B.M., Redemann, J., Bergstrom, R.W., Stohl, A., 2011. Simultaneous retrieval of aerosol and cloud properties during the MILAGRO field campaign. *Atmos. Chem. Phys.* 11, 6245–6263. <http://dx.doi.org/10.5194/acp-11-6245-2011>.
- Knobelspiesse, K., Cairns, B., Jethva, H., Kacenenlobogen, M., Segal-Rosenheimer, M., Torres, O., 2014. Remote sensing of mixed cloud and aerosol scenes. In: Kokhanovsky, A. (Ed.), *Light Scattering Reviews*. Springer Praxis Books Series vol. 9. Springer-Praxis, Chichester, United Kingdom.
- Knollenberg, R., Travis, L., Tomasko, M., Smith, P., Ragert, B., Esposito, L., McCleese, D., Martonchik, J., Beer, R., 1980. The clouds of Venus: a synthesis report. *J. Geophys. Res.* 85, 8059–8081. <http://dx.doi.org/10.1029/JA085A13p08059>.
- Koepke, P., 1984. Effective reflectance of oceanic whitecaps. *Appl. Optics* 23, 1816–1824. <http://dx.doi.org/10.1364/AO.23.001816>.
- Kokhanovsky, A.A., 2004. Spectral reflectance of whitecaps. *J. Geophys. Res.* 109, C05021. <http://dx.doi.org/10.1029/2003JC002177>.
- Kokhanovsky, A.A., 2008. *Aerosol optics. Light absorption and scattering by particles in the atmosphere*. Springer Praxis Books Series. Springer-Praxis, Berlin, Germany.
- Kokhanovsky, A.A., de Leeuw, G. (Eds.), 2009. *Satellite Aerosol Remote Sensing Over Land*. Springer Praxis Books Series. Springer-Praxis, Berlin, Germany.
- Kokhanovsky, A., Deuzé, J.L., Diner, D.J., Dubovik, O., Ducos, F., Emde, C., Garay, M.J., Grainger, R.G., Heckel, A., Herman, M., Katsev, I.L., Keller, J., Levy, R., North, P.R.J., Prikhach, A.S., Rozanov, V.V., Sayer, A.M., Ota, Y., Tanré, D., Thomas, G.E., Zege, E.P., 2010a. The inter-comparison of major satellite aerosol retrieval algorithms using simulated intensity and polarization characteristics of reflected light. *Atmos. Meas. Tech.* 3, 909–932. <http://dx.doi.org/10.5194/amt-3-909-2010>.
- Kokhanovsky, A.A., Budak, V.P., Cornet, C., Duan, M., Emde, C., Katsev, I.L., Klyukov, D.A., Korkin, S.V., Labonnote, L.C., Mayer, B., Min, Q., Nakajima, T., Ota, Y., Prikhach, A.S., Rozanov, V.V., Yokota, T., Zege, E.P., 2010b. Benchmark results in vector atmospheric radiative transfer. *J. Quant. Spectrosc. Radiat. Transf.* 111, 1931–1946. <http://dx.doi.org/10.1016/j.jqsrt.2010.03.005>.
- Kokhanovsky, A.A., Bréon, F.M., 2012. Validation of an analytical snow BRDF model using PARASOL multi-angular and multispectral observations. *IEEE Geosci. Remote Sens. Lett.* 9, 928–932. <http://dx.doi.org/10.1109/LGRS.2012.2185775>.
- Korkin, S.V., Lyapustin, A.I., Rozanov, V.V., 2013. APC: a new code for atmospheric polarization computations. *J. Quant. Spectrosc. Radiat. Transf.* 127, 1–11. <http://dx.doi.org/10.1016/j.jqsrt.2013.06.019>.
- Kotchenova, S.Y., Vermote, E.F., Matarrese, R., Klemm, F.J., 2006. Validation of a vector version of the 6S radiative transfer code for atmospheric correction of satellite data. Part I. Path radiance. *Appl. Opt.* 45, 6762–6774. <http://dx.doi.org/10.1364/AO.45.006762>.
- Kotchenova, S.Y., Vermote, E.F., 2007. Validation of a vector version of the 6S radiative transfer code for atmospheric correction of satellite data. Part II. Homogeneous Lambertian and anisotropic surfaces. *Appl. Opt.* 46, 4455–4464. <http://dx.doi.org/10.1364/AO.46.004455>.
- Kuze, A., Suto, H., Nakajima, M., Hamazaki, T., 2009. Thermal and near infrared sensor for carbon observation Fourier-transform spectrometer on the Greenhouse Gases Observing Satellite for greenhouse gases monitoring. *Appl. Opt.* 48, 6716–6733. <http://dx.doi.org/10.1364/AO.48.006716>.
- Langmore, I., Davis, A.B., Bal, G., 2013. Multipixel retrieval of structural and optical parameters in a 2-D scene with a path-replicating Monte Carlo forward model and a new Bayesian inference engine. *IEEE Trans. Geosci. Remote Sens.* 51, 2903–2919. <http://dx.doi.org/10.1109/TGRS.2012.2217380>.
- Lebsock, M.D., L'Ecuyer, T.S., Stephens, G.L., 2007. Information content of near-infrared spaceborne multiangular polarization measurements for aerosol retrievals. *J. Geophys. Res.* 112, D14206. <http://dx.doi.org/10.1029/2007JD008535>.
- L'Ecuyer, T.S., Jiang, J.H., 2010. Touring the atmosphere aboard the A-Train. *Phys. Today* 63, 36–41. <http://dx.doi.org/10.1063/1.3463626>.
- Lesins, G., Chylek, P., Lohmann, U., 2002. A study of internal and external mixing scenarios and its effect on aerosol optical properties and direct radiative forcing. *J. Geophys. Res.* 107. <http://dx.doi.org/10.1029/2001JD000973> (AAC 5-1–AAC 5-12).
- Li, X., Strahler, A.H., 1992. Geometric-optical bidirectional reflectance modeling of the discrete crown vegetation canopy: effect of crown shape and mutual shadowing. *IEEE Trans. Geosci. Remote Sens.* 30, 276–292. <http://dx.doi.org/10.1109/36.134078>.
- Litvinov, P., Hasekamp, O., Cairns, B., Mishchenko, M., 2010. Reflection models for soil and vegetation surfaces from multiple-viewing angle photopolarimetric measurements. *J. Quant. Spectrosc. Radiat. Transf.* 111, 529–539. <http://dx.doi.org/10.1016/j.jqsrt.2009.11.001>.
- Litvinov, P., Hasekamp, O., Cairns, B., 2011a. Models for surface reflection of radiance and polarized radiance: comparison with airborne multi-angle photopolarimetric measurements and implications for modeling top-of-atmosphere measurements. *Remote Sens. Environ.* 115, 781–892. <http://dx.doi.org/10.1016/j.rse.2010.11.005>.
- Litvinov, P., Hasekamp, O., Cairns, B., Mishchenko, M., 2011b. Semi-empirical BRDF and BPDF models applied to the problem of aerosol retrievals over land: testing on airborne data and implications for modeling of top-of-atmosphere measurements. In: Mishchenko, M.I., Yatskiv, Y.S., Rosenbush, V.K., Videen, G. (Eds.), *Polarimetric Detection, Characterization and Remote Sensing*. NATO Science for Peace and Security Series C: Environmental Security. Springer, Netherlands, Dordrecht, the Netherlands, pp. 313–340. [http://dx.doi.org/10.1007/978-94-007-1636-0\\_sdo5\(1\)3](http://dx.doi.org/10.1007/978-94-007-1636-0_sdo5(1)3).
- Litvinov, P., Hasekamp, O., Dubovik, O., Cairns, B., 2012. Model for land surface reflectance treatment: physical derivation, application for bare soil and evaluation on airborne and satellite measurements. *J. Quant. Spectrosc. Radiat. Transf.* 113, 2023–2039. <http://dx.doi.org/10.1016/j.jqsrt.2012.06.027>.
- Liu, Q., Ruprecht, E., 1996. Radiative transfer model: matrix operator method. *Appl. Opt.* 35, 4229–4237. <http://dx.doi.org/10.1364/AO.35.004229>.
- Liu, Q., Weng, F., 2006. Advanced doubling-adding method for radiative transfer in planetary atmospheres. *J. Atmos. Sci.* 63, 3459–3465. <http://dx.doi.org/10.1175/JAS3808.1>.
- Loyola, D.G., 2006. Applications of neural network methods to the processing of Earth observation satellite data. *Neural Netw.* 19, 168–177. <http://dx.doi.org/10.1016/j.neunet.2006.01.010>.
- Lyapustin, A.I., 2001. Three-dimensional effects in the remote sensing of surface albedo. *IEEE Trans. Geosci. Remote Sens.* 39, 254–263. <http://dx.doi.org/10.1109/36.905233>.
- Lyapustin, A.I., Kaufman, Y.J., 2001. Role of adjacency effect in the remote sensing of aerosol. *J. Geophys. Res.* 106, 11,909–11,916. <http://dx.doi.org/10.1029/2000JD900647>.
- Lyapustin, A.I., Knyazikhin, Y., 2002. Green's function method for the radiative transfer problem. II. Spatially heterogeneous anisotropic surface. *Appl. Opt.* 41, 5600–5606. <http://dx.doi.org/10.1364/AO.41.005600>.
- Lyapustin, A., Muldashev, T., Wang, Y., 2010. Code SHARM: fast and accurate radiative transfer over spatially variable anisotropic surfaces. In: Kokhanovsky, A.A. (Ed.), *Light Scattering Reviews*. Springer Praxis Books Series vol. 5. Springer, Berlin Heidelberg, Berlin, Germany, pp. 205–247. [http://dx.doi.org/10.1007/978-3-642-10336-0\\_sdo5\(6\)\(Chapter 6\)](http://dx.doi.org/10.1007/978-3-642-10336-0_sdo5(6)(Chapter 6)).
- Lyot, B., 1929. *Recherches sur la polarisation de la lumière des planètes et de quelques substances terrestres*. (Thesis), Faculté de Sciences de Paris, France (Also published in *Annales de l'Observatoire d'astronomie Physique de Paris*, sis à Meudon 8(1), 1929).
- Maignan, F., Bréon, F.M., Lacaze, R., 2004. Bidirectional reflectance of Earth targets: evaluation of analytical models using a large set of spaceborne measurements with emphasis on the Hot Spot. *Remote Sens. Environ.* 90, 210–220. <http://dx.doi.org/10.1016/j.rse.2003.12.006>.
- Maignan, F., Bréon, F.M., Fédèle, E., Bouvier, M., 2009. Polarized reflectances of natural surfaces: spaceborne measurements and analytical modeling. *Remote Sens. Environ.* 113, 2642–2650. <http://dx.doi.org/10.1016/j.rse.2009.07.022>.
- Marbach, T., Phillips, P., Lacan, A., Schlüssel, P., 2013. 3M: The Multi-Viewing, -Channel, -Polarisation Imager of the EUMETSAT Polar System – Second Generation (EPS-SG) dedicated to aerosol characterization. *Proc. SPIE 8889, Sensors, Systems and Next-Generation Satellites XVIII* <http://dx.doi.org/10.1117/12.2028221>.
- Marchuk, G.I., Mikhailov, G.A., Nazaraliev, M.A., Darbinjan, R.A., Kargin, B.A., Elepov, B.S., 1980. *The Monte Carlo methods in atmospheric optics*. Springer Series in Optical Sciences. Springer, Berlin Heidelberg, Berlin, Germany <http://dx.doi.org/10.1007/978-3-540-35237-2>.
- Marshak, A., Wen, G., Coakley Jr., J.A., Remer, L.A., Loeb, N.G., Cahalan, R.F., 2008. A simple model for the cloud adjacency effect and the apparent bluing of aerosols near clouds. *J. Geophys. Res.* 113, D14517. <http://dx.doi.org/10.1029/2007JD009196>.
- Martonchik, J.V., Diner, D.J., Kahn, R.A., Ackerman, T.P., Verstraete, M.M., Pinty, B., Gordon, H.R., 1998a. Techniques for the retrieval of aerosol properties over land and ocean using multiangle imaging. *IEEE Trans. Geosci. Remote Sens.* 36, 1212–1227. <http://dx.doi.org/10.1109/36.701027>.
- Martonchik, J.V., Diner, D.J., Kahn, R.A., Verstraete, M.M., Myneni, R.B., Knyazikhin, Y., Gordon, H.R., 1998b. Determination of land and ocean reflective, radiative, and biophysical properties using multiangle imaging. *IEEE Trans. Geosci. Remote Sens.* 36, 1266–1281. <http://dx.doi.org/10.1109/36.701077>.
- Martonchik, J.V., Diner, D.J., Crean, K.A., Bull, M.A., 2002. Regional aerosol retrieval results from MISR. *IEEE Trans. Geosci. Remote Sens.* 40, 1520–1531. <http://dx.doi.org/10.1109/TGRS.2002.801142>.
- Martonchik, J.V., Kahn, R.A., Diner, D.J., 2009. Retrieval of aerosol properties over land using MISR observations. In: Kokhanovsky, A.A., de Leeuw, G. (Eds.), *Satellite aerosol remote sensing over land*. Springer Praxis Books Series, pp. 267–293. [http://dx.doi.org/10.1007/978-3-540-69397-0\\_9](http://dx.doi.org/10.1007/978-3-540-69397-0_9) Chapter 9.
- Mekler, Y., Kaufman, Y.J., 1980. The effect of earth's atmosphere on contrast reduction for a nonuniform surface albedo and 'two-halves' field. *J. Geophys. Res.* 85, 4067–4083. <http://dx.doi.org/10.1029/JC085C07p04067>.
- Mishchenko, M.I., Travis, L.D., 1997. Satellite retrievals of aerosol properties over the ocean using polarization as well as intensity of reflected sunlight. *J. Geophys. Res.* 102, 16989–17013. <http://dx.doi.org/10.1029/96JD02425>.
- Mishchenko, M.I., Hovenier, J.W., Travis, L.D. (Eds.), 1999. *Light Scattering by Nonspherical Particles: Theory, Measurements, and Applications*. Academic Press, San Diego, CA, United States.
- Mishchenko, M.I., 2002. Vector radiative transfer equation for arbitrarily shaped and arbitrarily oriented particles: a microphysical derivation from statistical electromagnetics. *Appl. Opt.* 41, 7114–7134. <http://dx.doi.org/10.1364/AO.41.007114>.
- Mishchenko, M.I., Travis, L.D., Lacis, A., 2006. *Multiple Scattering of Light by Particles*. Cambridge University Press, Cambridge, United Kingdom.
- Mishchenko, M.I., Geogdzhayev, I.V., Cairns, B., Carlson, B.E., Chowdhary, J., Lacis, A.A., Liu, L., Rossow, W.B., Travis, L.D., 2007a. Past, present, and future of global aerosol climatologies derived from satellite observations: a perspective. *J. Quant. Spectrosc. Radiat. Transf.* 106, 325–347. <http://dx.doi.org/10.1016/j.jqsrt.2007.01.007>.

- Mishchenko, M.I., Cairns, B., Hansen, J.E., Travis, L.D., Kopp, G., Schuelern, C.F., Fafaul, B.A., Hooker, R.J., Maring, H.B., Itchikawich, T., 2007b. Accurate monitoring of terrestrial aerosols and total solar irradiance: introducing the Glory mission. *Bull. Am. Meteorol. Soc.* 88, 677–691. <http://dx.doi.org/10.1175/BAMS-88-5-677>.
- Mishchenko, M.I., Travis, L.D., 2008. Gustav Mie and the evolving discipline of electromagnetic scattering by particles. *Bull. Am. Meteorol. Soc.* 89, 1853–1861. <http://dx.doi.org/10.1175/2008BAMS2632.1>.
- Mishchenko, M.I., Tishkovets, V.P., Travis, L.D., Cairns, B., Dlugach, J.M., Liu, L., Rosenbush, V.K., Kiselev, N.N., 2011. Electromagnetic scattering by a morphologically complex object: fundamental concepts and common misconceptions. *J. Quant. Spectrosc. Radiat. Transf.* 112, 671–692. <http://dx.doi.org/10.1016/j.jqsrt.2010.03.016>.
- Mishchenko, M.I., 2014. *Electromagnetic Scattering by Particles and Particle Groups. An Introduction*. Cambridge University Press, Cambridge, United Kingdom.
- Mitchell, R.M., 1987. The effects of aerosol scattering on remote pressure measurement via oxygen A-band absorption. *Int. J. Remote Sens.* 8, 1175–1188. <http://dx.doi.org/10.1080/01431168708954763>.
- Mitchell, R.M., O'Brien, D.M., 1987. Error estimates for passive satellite measurement of surface pressure using absorption in the A band of oxygen. *J. Atmos. Sci.* 44, 1981–1990. [http://dx.doi.org/10.1175/1520-0469\(1987\)044<1981%3AEEFPM>2.0.CO;3B2](http://dx.doi.org/10.1175/1520-0469(1987)044<1981%3AEEFPM>2.0.CO;3B2).
- Muinsonen, K., 2004. Coherent backscattering of light by complex media of spherical scatterers: numerical solution. *Waves Random Media* 14, 365–388. <http://dx.doi.org/10.1088/0959-7174/14/3/010>.
- Müller, M.D., Kaifel, A., Weber, M., Tellmann, S., Burrows, J.P., Loyola, D., 2003. Ozone profile retrieval from Global Ozone Monitoring Experiment (GOME) data using a neural network approach (Neural Network Ozone Retrieval System (NNORSY)). *J. Geophys. Res.* 108, 4497. <http://dx.doi.org/10.1029/2002JD002784>.
- Muñoz, O., Volten, H., Hovenier, J.W., Nousiainen, T., Muinsonen, K., Guirado, D., Moreno, F., Waters, L.B.F.M., 2007. Scattering matrix of large Saharan dust particles: experiments and computations. *J. Geophys. Res.* 112, D13215. <http://dx.doi.org/10.1029/2006JD008074>.
- Nadal, F., Bréon, F.M., 1999. Parameterization of surface polarized reflectance derived from POLDER spaceborne measurements. *IEEE Trans. Geosci. Remote Sens.* 37, 1709–1718. <http://dx.doi.org/10.1109/36.763292>.
- Nakajima, T., Tanaka, M., 1986. Matrix formulations for the transfer of solar radiation in a plane-parallel scattering atmosphere. *J. Quant. Spectrosc. Radiat. Transf.* 35, 13–21. [http://dx.doi.org/10.1016/0022-4073\(86\)90088-9](http://dx.doi.org/10.1016/0022-4073(86)90088-9).
- Nakajima, T., Tanaka, M., 1988. Algorithms for radiative intensity calculations in moderately thick atmospheres using a truncation approximation. *J. Quant. Spectrosc. Radiat. Transf.* 40, 51–69. [http://dx.doi.org/10.1016/0022-4073\(88\)90031-3](http://dx.doi.org/10.1016/0022-4073(88)90031-3).
- Nikolaeva, O.V., Bass, L.P., Germogenova, T.A., Kokhanovsky, A.A., Kuznetsov, V.S., Mayer, B., 2005. The influence of neighbouring clouds on the clear sky reflectance studied with the 3-D transport code RADUGA. *J. Quant. Spectrosc. Radiat. Transf.* 94, 405–424. <http://dx.doi.org/10.1016/j.jqsrt.2004.09.037>.
- O'Brien, D.M., Mitchell, R.M., 1992. Error estimates for retrieval of cloud-top pressure using absorption in the A-Band of oxygen. *J. Appl. Meteorol.* 31, 1179–1192. [http://dx.doi.org/10.1175/1520-0450\(1992\)031<1179:EEFROC>2.0.CO;2](http://dx.doi.org/10.1175/1520-0450(1992)031<1179:EEFROC>2.0.CO;2).
- Oka, K., Kato, T., 1999. Spectroscopic polarimetry with a channeled spectrum. *Opt. Lett.* 24, 1475–1477. <http://dx.doi.org/10.1364/OL.24.001475>.
- Otterman, J., Fraser, R.S., 1979. Adjacency effects on imaging by surface reflection and atmospheric scattering: cross radiance to zenith. *Appl. Opt.* 18, 2852–2860. <http://dx.doi.org/10.1364/AO.18.002852>.
- Otterman, J., Ungar, S., Kaufman, Y., Podolak, M., 1980. Atmospheric effects on radiometric imaging from satellites under low optical thickness conditions. *Remote Sens. Environ.* 9, 115–129. [http://dx.doi.org/10.1016/0034-4257\(80\)90003-6](http://dx.doi.org/10.1016/0034-4257(80)90003-6).
- Pellicori, S.F., Russell, E.E., Watts, L.A., 1973. Pioneer imaging photopolarimeter optical system. *Appl. Opt.* 12, 1246–1258. <http://dx.doi.org/10.1364/AO.12.001246>.
- Phillips, D.L., 1962. A technique for the numerical solution of certain integral equations of the first kind. *J. Assoc. Comput. Mach.* 9, 84–97. <http://dx.doi.org/10.1145/3211105.321114>.
- Pierce, J.R., Kahn, R.A., Davis, M.R., Comstock, J.M., 2010. Detecting thin cirrus in Multiangle Imaging Spectroradiometer aerosol retrievals. *J. Geophys. Res.* 115, D08201. <http://dx.doi.org/10.1029/2009JD013019>.
- Potter, J.F., 1970. The delta function approximation in radiative transfer theory. *J. Atmos. Sci.* 27, 943–949. [http://dx.doi.org/10.1175/1520-0469\(1970\)027<0943:TDFAIR>2.0.CO;2](http://dx.doi.org/10.1175/1520-0469(1970)027<0943:TDFAIR>2.0.CO;2).
- Povel, H., Aebersold, H., Stenflo, J.O., 1990. Charge-coupled device image sensor as a demodulator in a 2-D polarimeter with a piezoelectric modulator. *Appl. Opt.* 29, 1186–1190. <http://dx.doi.org/10.1364/AO.29.001186>.
- Preisendorfer, R.W., 1965. *Radiative Transfer on Discrete Spaces vol. 1*. Pergamon Press, Oxford, United Kingdom.
- Priest, R.G., Meier, S.R., 2002. Polarimetric microfacet scattering theory with applications to absorptive and reflective surfaces. *Opt. Eng.* 41, 988–993. <http://dx.doi.org/10.1117/1.1467360>.
- Rahman, H., Verstraete, M.M., Pinty, B., 1993a. Coupled surface-atmosphere reflectance (CSAR) model: 1. Model description and inversion on synthetic data. *J. Geophys. Res.* 98, 20,779–20,789. <http://dx.doi.org/10.1029/93JD02071>.
- Rahman, H., Pinty, B., Verstraete, M.M., 1993b. Coupled surface-atmosphere reflectance (CSAR) model: 2. Semiempirical surface model usable with NOAA advanced very high resolution radiometer data. *J. Geophys. Res.* 98, 20,791–20,801. <http://dx.doi.org/10.1029/93JD02072>.
- Reinersman, P.N., Carder, K.L., 1995. Monte Carlo simulation of the atmospheric point-spread function with an application to correction for the adjacency effect. *Appl. Opt.* 34, 4453–4471. <http://dx.doi.org/10.1364/AO.34.004453>.
- Richter, R., Schläpfer, D., 2002. Geo-atmospheric processing of airborne imaging spectrometry data. Part 2: atmospheric/topographic correction. *Int. J. Remote Sens.* 23, 2631–2649. <http://dx.doi.org/10.1080/01431160110115834>.
- Rietjens, J.H.H., van Harten, G., Bekkers, D., Vreeker, A., Snik, F., Smit, J.M., Keller, C.U., 2015. Performance of spectrally modulated polarimetry II: Data reduction and absolute polarization calibration of a prototype SPEX satellite instrument (in preparation).
- Ristovski, K., Vucetic, S., Obradovic, Z., 2012. Uncertainty analysis of neural-network-based aerosol retrieval. *IEEE Trans. Geosci. Remote Sens.* 50, 409–414. <http://dx.doi.org/10.1109/TGRS.2011.2166120>.
- Roache, P.J., 1998. *Verification and Validation in Computational Science and Engineering*. Hermosa Publishers, Albuquerque, NM, United States.
- Rodgers, C.D., 2000. *Inverse Methods for Atmospheric Sounding: Theory and Practice*. World Scientific, London, United Kingdom.
- Ross, J.K., 1981. *The Radiation Regime and Architecture of Plant Stands*. Dr. W. Junk Publishers, The Hague, the Netherlands.
- Roujean, J.L., Leroy, M., Deschamps, P.Y., 1992. A bidirectional reflectance model of the Earth's surface for the correction of remote sensing data. *J. Geophys. Res.* 97, 20455–20468. <http://dx.doi.org/10.1029/92JD01411>.
- Royer, A., Davis, A., O'Neill, N., 1988. Analyse des effets atmosphériques dans les images HRV de SPOT. *Can. J. Remote. Sens.* 14, 80–91. <http://dx.doi.org/10.1080/07038992.1988.10855123>.
- Ročanov, V.V., Ročanov, A.V., Kokhanovsky, A.A., Burrows, J.P., 2014. Radiative transfer through terrestrial atmosphere and ocean: software package SCIATRAN. *J. Quant. Spectrosc. Radiat. Transf.* 133, 13–71. <http://dx.doi.org/10.1016/j.jqsrt.2013.07.004>.
- Russell, E.E., Watts, L.A., Pellicori, F.S., Coffeen, D.L., 1977. Orbiter cloud photopolarimeter for the pioneer venus mission. *Proc. SPIE* 0112, Optical Polarimetry: Instrumentation and Applications <http://dx.doi.org/10.1117/12.955539>.
- Russell, E.E., Brown, F.G., Chandos, R.A., Fincher, W.C., Kubel, L.F., Lacin, A.A., Travis, L.D., 1992. Galileo Photopolarimeter/Radiometer experiment. *Space Sci. Rev.* 60, 531–563. <http://dx.doi.org/10.1007/BF00216867>.
- Sanghavi, S.V., Martonchik, J.V., Davis, A.B., Diner, D.J., 2013. Linearization of a scalar matrix operator method radiative transfer model with respect to aerosol and surface properties. *J. Quant. Spectrosc. Radiat. Transf.* 116, 1–16. <http://dx.doi.org/10.1016/j.jqsrt.2012.10.021>.
- Sanghavi, S., Davis, A.B., Eldering, A., 2014. vSmartMOM: a vector matrix operator method-based radiative transfer model linearized with respect to aerosol properties. *J. Quant. Spectrosc. Radiat. Transf.* 133, 412–433. <http://dx.doi.org/10.1016/j.jqsrt.2013.09.004>.
- Sano, I., 2004. Optical thickness and Angstrom exponent of aerosols over the land and ocean from space-borne polarimetric data. *Adv. Space Res.* 34, 833–837. <http://dx.doi.org/10.1016/j.asr.2003.06.039>.
- Savenkov, S.N., 2002. Optimization and structuring of the instrument matrix for polarimetric measurements. *Opt. Eng.* 41, 965–972.
- Savenkov, S.N., Muttiah, R.S., Oberemok, Y.A., 2003. Transmitted and reflected scattering matrices from an English oak leaf. *Appl. Opt.* 42, 4955–4962. <http://dx.doi.org/10.1364/AO.42.004955>.
- Schaepman-Strub, G., Schaeppman, M.E., Painter, T.H., Dangel, S., Martonchik, J.V., 2006. Reflectance quantities in optical remote sensing: definitions and case studies. *Remote Sens. Environ.* 103, 27–42. <http://dx.doi.org/10.1016/j.rse.2006.03.002>.
- Seinfeld, J.H., Pandis, S., 2006. *Atmospheric Chemistry and Physics: From Air Pollution to Climate Change*. Wiley, New York, NY, United States.
- Semenov, A.A., Moshkov, A.V., Pozhidayev, V.N., Barducci, A., Marcoianni, P., Pippi, I., 2011. Estimation of normalized atmospheric point spread function and restoration of remotely sensed images. *IEEE Trans. Geosci. Remote Sens.* 49, 2623–2634. <http://dx.doi.org/10.1109/TGRS.2011.2114351>.
- Smith, B.G., 1967. Geometrical shadowing of a random rough surface. *IEEE Trans. Antennas Propag.* 15, 668–671.
- Snik, F., Karalidi, T., Keller, C.U., 2009. Spectral modulation for full linear polarimetry. *Appl. Opt.* 48, 1337–1346. <http://dx.doi.org/10.1364/AO.48.001337>.
- Spurr, R.J.D., 2006. VLDORT: a linearized pseudo-spherical vector discrete ordinate radiative transfer code for forward model and retrieval studies in multilayer multiple scattering media. *J. Quant. Spectrosc. Radiat. Transf.* 102, 316–342. <http://dx.doi.org/10.1016/j.jqsrt.2006.05.005>.
- Stam, D.M., de Haan, J.F., Hovenier, J.W., Stammes, P., 1999. Degree of linear polarization of light emerging from the cloudless atmosphere in the oxygen A band. *J. Geophys. Res.* 104, 16,843–16,858. <http://dx.doi.org/10.1029/1999JD900159>.
- Stam, D.M., de Haan, J.F., Hovenier, J.W., Stammes, P., 2000. A fast method for simulating observations of polarized light emerging from the atmosphere applied to the oxygen-A band. *J. Quant. Spectrosc. Radiat. Transf.* 64, 131–149. [http://dx.doi.org/10.1016/S0022-4073\(99\)00009-6](http://dx.doi.org/10.1016/S0022-4073(99)00009-6).
- Stammes, K., Tsay, S.C., Wiscombe, W., Jayaweera, K., 1988. Numerically stable algorithm for discrete-ordinate-method radiative transfer in multiple scattering and emitting layered media. *Appl. Opt.* 27, 2502–2509. <http://dx.doi.org/10.1364/AO.27.002502>.
- Stammes, K., Hamre, B., Stammes, J.J., Ryzhikov, G., Biryulina, M., Mahoney, R., Hauss, B., Sei, A., 2011. Modeling of radiation transport in coupled atmosphere-snow-ice-ocean systems. *J. Quant. Spectrosc. Radiat. Transf.* 112, 714–726.
- Stephens, G.L., Heidinger, A., 2000. Molecular line absorption in a scattering atmosphere, part I: theory. *J. Atmos. Sci.* 57, 1599–1614. [http://dx.doi.org/10.1175/1520-0469\(2000\)057<1599:3AMLAIAS>2.0.CO;3B2](http://dx.doi.org/10.1175/1520-0469(2000)057<1599:3AMLAIAS>2.0.CO;3B2).
- Sterckx, S., Knaeps, E., Ruddick, K., 2011. Detection and correction of adjacency effects in hyperspectral airborne data of coastal and inland waters: the use of the near infrared similarity spectrum. *Int. J. Remote Sens.* 32, 6479–6505. <http://dx.doi.org/10.1080/01431161.2010.512930>.

- Takashima, T., Masuda, K., 1992. Simulation of atmospheric effects on the emergent radiation over a checkerboard type of terrain. *Astrophys. Space Sci.* 198, 253–263. <http://dx.doi.org/10.1007/BF00644757>.
- Tanré, D., Herman, M., Deschamps, Y., 1981. Influence of the background contribution upon space measurements of ground reflectance. *Appl. Opt.* 20, 3676–3684. <http://dx.doi.org/10.1364/AO.20.003676>.
- Tapiador, F.J., Kidd, C., Hsu, K.L., Marzano, F., 2004. Neural networks in satellite rainfall estimation. *Meteorol. Appl.* 11, 83–91. <http://dx.doi.org/10.1017/S1350482704001173>.
- Tikhonov, A., 1963. On the solution of incorrectly stated problems and a method of regularization. *Dokl. Akad. Nauk SSSR* 151, 501–504.
- Timofeyev, Yu.M., Vasilyev, A.V., Rozanov, V.V., 1995. Information content of the spectral measurements of the 0.76  $\mu\text{m}$   $\text{O}_2$  outgoing radiation with respect to the vertical aerosol optical properties. *Adv. Space Res.* 16, 91–94. [http://dx.doi.org/10.1016/0273-1177\(95\)00385-R](http://dx.doi.org/10.1016/0273-1177(95)00385-R).
- Tishkovets, V.P., Petrova, E.V., Jockers, K., 2004. Optical properties of aggregate particles comparable in size to the wavelength. *J. Quant. Spectrosc. Radiat. Transf.* 86, 241–265. <http://dx.doi.org/10.1016/j.jqsrt.2003.08.003>.
- Tishkovets, V.P., Jockers, K., 2006. Multiple scattering of light by densely packed random media of spherical particles: dense media vector radiative transfer equation. *J. Quant. Spectrosc. Radiat. Transf.* 101, 54–72. <http://dx.doi.org/10.1016/j.jqsrt.2005.10.001>.
- Tishkovets, V.P., Mishchenko, M.I., 2009. Approximate calculation of coherent backscattering for semi-infinite discrete random media. *J. Quant. Spectrosc. Radiat. Transf.* 110, 139–145. <http://dx.doi.org/10.1016/j.jqsrt.2008.09.005>.
- Tishkovets, V.P., Petrova, E.V., Mishchenko, M.I., 2011. Scattering of electromagnetic waves by ensembles of particles and discrete random media. *J. Quant. Spectrosc. Radiat. Transf.* 112, 2095–2127. <http://dx.doi.org/10.1016/j.jqsrt.2011.04.010>.
- Torres, O., Jethva, H., Bhartia, P.K., 2012. Retrieval of aerosol optical depth above clouds from OMI observations: sensitivity analysis and case studies. *J. Atmos. Sci.* 69, 1037–1053. <http://dx.doi.org/10.1175/JAS-D-11-0130.1>.
- Tsang, L., Kong, J.A., 2001. *Scattering of electromagnetic waves: advanced topics*. Wiley Series in Remote Sensing, Wiley, New York, NY, United States.
- van de Hulst, H.C., 1980. *Multiple Light Scattering: Tables, Formulas, and Applications 2 vols*. Academic Press, San Diego, CA, United States.
- van Diedenhoven, B., Hasekamp, O.P., Aben, I., 2005. Surface pressure retrieval from SCIAMACHY measurements in the  $\text{O}_2$  A-band: validation of the measurements and sensitivity on aerosols. *Atmos. Chem. Phys.* 5, 2109–2120. <http://dx.doi.org/10.5194/acp-5-2109-2005>.
- van Harten, G., Snik, F., Rietjens, J.H.H., Smit, J.M., de Boer, J., Diamantopoulou, R., Hasekamp, O.P., Stam, D.M., Keller, C.U., Laan, E.C., Verlaan, A.L., Vliegthart, W.A., ter Horst, R., Navarro, R., Wielinga, K., Hannemann, S., Moon, S.G., Voors, R., 2011. Prototyping the Spectropolarimeter for Planetary Exploration (SPEX): calibration and sky measurements. *Proc. SPIE 8160, Polarization Science and Remote Sensing V* <http://dx.doi.org/10.1117/12.893741>.
- van Harten, G., 2014. *Spectropolarimetry for Planetary Exploration*. PhD thesis, Leiden University, ISBN 978-94-6259-458-6.
- van Harten, G., de Boer, J., Rietjens, J.H.H., Di Noia, A., Snik, F., Volten, H., Smit, J.M., Hasekamp, O.P., Henzing, J.S., Keller, C.U., 2014. Atmospheric aerosol characterization with a ground-based SPEX spectropolarimetric instrument. *Atmos. Meas. Tech.* 7, 4341–4351. <http://dx.doi.org/10.5194/amt-7-4341-2014>.
- Várnai, T., Marshak, A., 2009. MODIS observations of enhanced clear sky reflectance near clouds. *Geophys. Res. Lett.* 36, L06807. <http://dx.doi.org/10.1029/2008GL037089>.
- Várnai, T., Marshak, A., 2011. Global CALIPSO observations of aerosol changes near clouds. *IEEE Geosci. Remote Sens. Lett.* 8, 19–23. <http://dx.doi.org/10.1109/LGRS.2010.2049982>.
- Vucetic, S., Han, B., Mi, W., Li, Z., Obradovic, Z., 2008. A data mining approach for the validation of aerosol retrievals. *IEEE Geosci. Remote Sens. Lett.* 5, 113–117. <http://dx.doi.org/10.1109/LGRS.2007.912725>.
- Wang, M., Gordon, H.R., 1994. Radiance reflected from the ocean–atmosphere system: synthesis from individual components of the aerosol size distribution. *Appl. Opt.* 33, 7088–7095. <http://dx.doi.org/10.1364/AO.33.007088>.
- Wanner, W., Li, X., Strahler, A.H., 1995. On the derivation of kernels for kernel-driven models of bidirectional reflectance. *J. Geophys. Res.* 100, 21,077–21,089. <http://dx.doi.org/10.1029/95JD02371>.
- Waquet, F., Léon, J.F., Cairns, B., Goloub, P., Deuzé, J.L., Auriol, F., 2009a. Analysis of the spectral and angular response of the vegetated surface polarization for the purpose of aerosol remote sensing over land. *Appl. Opt.* 48, 1228–1236. <http://dx.doi.org/10.1364/AO.48.001228>.
- Waquet, F., Riedi, J.C., Labonnote, L., Goloub, P., Cairns, B., Deuzé, J.-L., Tanré, D., 2009b. Aerosol remote sensing over clouds using A-train observations. *J. Atmos. Sci.* 66, 2468–2480. <http://dx.doi.org/10.1175/2009JAS3026.1>.
- Waquet, F., Cornet, C., Deuzé, J.L., Dubovik, O., Ducos, F., Goloub, P., Herman, M., Lapyonok, T., Labonnote, L.C., Riedi, J., Tanré, D., Thieuleux, F., Vanbauce, C., 2013. Retrieval of aerosol microphysical and optical properties above liquid clouds from POLDER/PARASOL polarization measurements. *Atmos. Meas. Tech.* 6, 991–1016. <http://dx.doi.org/10.5194/amt-6-991-2013>.
- Wen, G., Marshak, A., Cahalan, R.F., Remer, L.A., Kleidman, R.G., 2007. 3-D aerosol–cloud radiative interaction observed in collocated MODIS and ASTER images of cumulus cloud fields. *J. Geophys. Res.* 112, D13204. <http://dx.doi.org/10.1029/2006JD008267>.
- Winker, D.M., Pelon, J., Coakley Jr., J.A., Ackerman, S.A., Charlson, R.J., Colarco, P.R., Flamant, P., Fu, Q., Hoff, R., Kittaka, C., Kubar, T.L., LeTret, H., McCormick, M.P., Megie, G., Poole, L., Powell, K., Trepte, C., Vaughan, M.A., Wielicki, B.A., 2010. The CALIPSO mission: a global 3D view of aerosols and clouds. *Bull. Am. Meteorol. Soc.* 91, 1211–1229. <http://dx.doi.org/10.1175/2010BAMS3009.1>.
- Wiscombe, W.J., 1976. On initialization, error and flux conservation in the doubling method. *J. Quant. Spectrosc. Radiat. Transf.* 16, 637–658. [http://dx.doi.org/10.1016/0022-4073\(76\)90056-X](http://dx.doi.org/10.1016/0022-4073(76)90056-X).
- Wiscombe, W.J., 1977. The delta-M method: rapid yet accurate radiative flux calculations for strongly asymmetric phase functions. *J. Atmos. Sci.* 34, 1408–1422. [http://dx.doi.org/10.1175/1520-0469\(1977\)034<1408:TDMRYA>2.0.CO;2](http://dx.doi.org/10.1175/1520-0469(1977)034<1408:TDMRYA>2.0.CO;2).
- Woolley, J.T., 1971. Reflectance and transmittance of light by leaves. *Plant Physiol.* 47, 656–662. <http://dx.doi.org/10.1104/pp.47.5.656>.
- Wu, M.C., 1985. Remote sensing of cloud-top pressure using reflected solar radiation in the oxygen A-band. *J. Clim. Appl. Meteorol.* 24, 539–546. [http://dx.doi.org/10.1175/1520-0450\(1985\)024<0539%3ARS0CTP>2.0.CO;3B2](http://dx.doi.org/10.1175/1520-0450(1985)024<0539%3ARS0CTP>2.0.CO;3B2).
- Xie, D., Gu, X., Cheng, T., Yu, T., Li, Z., Chen, X., Chen, H., Guo, Jing, 2011. The initial research for polarized reflectance of typical urban surface types based on DPC. *China Earth Sci.* 54, 1199–1205. <http://dx.doi.org/10.1007/s11430-011-4216-z>.
- Xie, D., Cheng, T., Zhang, W., Yu, J., Li, X., Gong, H., 2013. Aerosol type over east Asian retrieval using total and polarized remote sensing. *J. Quant. Spectrosc. Radiat. Transf.* 129, 15–30. <http://dx.doi.org/10.1016/j.jqsrt.2013.05.028>.
- Xu, F., Davis, A.B., West, R.A., Esposito, L.W., 2011a. Markov chain formalism for polarized light transfer in plane-parallel atmospheres, with numerical comparison to the Monte Carlo method. *Opt. Express* 19, 946–967. <http://dx.doi.org/10.1364/OE.19.000946>.
- Xu, F., Davis, A.B., West, R.A., Martonchik, J.V., Diner, D.J., 2011b. Markov chain formalism for vector radiative transfer in a plane-parallel atmosphere overlying a polarizing surface. *Opt. Lett.* 36, 2083–2085. <http://dx.doi.org/10.1364/OL.36.002083>.
- Xu, F., Davis, A.B., Sanghavi, S.V., Martonchik, J.V., Diner, D.J., 2012. Linearization of Markov chain formalism for vector radiative transfer in a plane-parallel atmosphere/surface system. *Appl. Opt.* 51, 3491–3507. <http://dx.doi.org/10.1364/AO.51.003491>.
- Yamamoto, G., Wark, D.Q., 1961. Discussion of the letter by R.A. Hanel, "Determination of cloud altitude from a satellite". *J. Geophys. Res.* 66, 3596. <http://dx.doi.org/10.1029/JZ066i010p03596>.
- Zeng, J., Han, Q., Wang, J., 2008. High-spectral resolution simulation of polarization of skylight: sensitivity to aerosol vertical profile. *Geophys. Res. Lett.* 35, L20801. <http://dx.doi.org/10.1029/2008GL035645>.
- Zhai, P.W., Hu, Y., Trepte, C.R., Lucker, P., 2009. A vector radiative transfer model for coupled atmosphere and ocean systems based on successive order of scattering method. *Opt. Express* 17, 2057–2079. <http://dx.doi.org/10.1364/OE.17.002057>.
- Zhang, J., Reid, J.S., Holben, B.N., 2005. An analysis of potential cloud artifacts in MODIS over ocean aerosol optical thickness products. *Geophys. Res. Lett.* 32, L15803. <http://dx.doi.org/10.1029/2005GL023254>.